# Gallium Metal Nanoparticles for Plasmonics and Droplet Epitaxy:

# Formation and Properties

by

Sunyeol Jeon

A dissertation submitted in partial fulfillment
of the requirements for the degree of
Doctor of Philosophy
(Materials Science and Engineering)
in the University of Michigan
2016

Doctoral Committee:

Professor Rachel S. Goldman, Chair
Assistant Professor Emmanouil Kioupakis
Associate Professor Pei-Cheng Ku
Associate Professor Vanessa Sih

© Sunyeol Jeon
2016

## Acknowledgements

I would like to thank my thesis advisor, Prof. Rachel S. Goldman, for her guidance and support throughout my studies at the University of Michigan. I would also like to thank my thesis committee members, Prof. Pei Cheng Ku, Prof. Vanessa Sih, and Prof. Emmanouil Kioupakis, for their valuable discussions and suggestions.

This dissertation would not have been possible without the help of my collaborators. Especially, I would like to acknowledge Dr. Jieun Lee in Prof. Vanessa Sih's group, Tyler Hill and Adam Katcher in Prof. Hui Deng's group at University of Michigan.

Special thanks go to my fellow group members, Dr. Jia-Hung Wu, Dr. Adam Wood, Dr. Michael Warren, Dr. Justin Canniff, Dr. Myungkoo Kang, Dr. Simon Huang, Dr. Yen-Hsiang Lin, Alexander Chang, Jenna Walrath, Tim Jen, Davide Del Gaudio, Jordan Occena, and Caleb Reese, for their useful discussions, suggestions, and encouragement.

This work was supported by the National Science Foundation through the Materials Research Science and Engineering Center (MRSEC) at the University of Michigan, grant No. DMR-1120923. This research was also supported in part by the Center for Solar and Thermal Energy Conversion, an Energy Frontier Research Center, funded by the U.S. Department of Energy, Office of Science, Office of Basic Energy Sciences under Award No. DE-SC0000957.

## Table of Contents

Acknowledgements ..... ii

List of Figures ..... vi

List of Tables ..... xiv

List of Appendices ..... xv

Abstract ..... xvi

Chapter 1 Introduction ..... 1

1.1 Overview ..... 1

1.2 Nanostructured Materials: Light-matter Interactions ..... 3

1.3 Ga Nanoparticles for Plasmonics ..... 6

1.4 GaN Nanostructures for Optoelectronics ..... 7

1.5 Dissertation Objectives ..... 10

1.6 Dissertation Organization ..... 11

1.7 References ..... 20

Chapter 2 Experimental Procedures ..... 28

2.1 Overview ..... 28

2.2 Focused Ion Beam Irradiation ..... 28

2.3 Molecular Beam Epitaxy ..... 29

2.4 Reflected High-Energy Electron Diffraction ..... 32

2.5 Atomic Force Microscopy ..... 33

2.6 Scanning Electron Microscopy ..... 34

2.7 X-Ray Diffraction ........................................................................................ 34

2.8 Photoluminescence ........................................................................................ 35

2.9 References ........................................................................................ 39

Chapter 3 Formation of embedded Ga nanoparticle (NP) arrays and their influence on GaAs photoluminescence ........................................................................................ 40

3.1 Overview ........................................................................................ 40

3.2 Background: Ga Metallic Nanoparticle Surface Plasmon Resonances ...................... 41

3.3 Fabrication of embedded GaAs:Ga Nanocomposites ........................................... 42

3.4 Morphology and Structure of GaAs:Ga Nanocomposites .................................... 43

3.5 Influence of Ga NP size and Depth on GaAs Photoluminescence ......................... 45

3.6 FDTD Simulations ........................................................................................ 47

3.7 PL Enhancement Comparison of Theory and Experiment .................................... 54

3.8 Conclusions ........................................................................................ 54

3.9 References ........................................................................................ 69

Chapter 4 Droplet Epitaxy of GaN QDs ........................................................................................ 72

4.1 Overview ........................................................................................ 72

4.2 Background ........................................................................................ 73

4.3 Experimental Details ........................................................................................ 75

4.4 Droplet Epitaxy on c-GaN substrates ........................................................................................ 77

4.5 Droplet Epitaxy on r-$Al_2O_3$ substrates ........................................................................................ 78

4.6 Droplet Epitaxy on Si substrates ........................................................................................ 78

4.7 Conclusions ........................................................................................ 81

4.8 References ........................................................................................ 95

Chapter 5 Formation and Optical Properties of Zincblende-Wurtzite GaN Films and Nanowires ........................................................................................ 100

5.1 Overview ........ 100

5.2 Background ........ 101

5.3 Experimental Details ........ 102

5.4 Formation of Zincblende-Wurtzite GaN Films and Nanowires ........ 103

5.5 Optical Properties of Zincblende-Wurtzite GaN Films and Nanowires ........ 108

5.6 Conclusions ........ 109

5.7 References ........ 118

Chapter 6 Summary and Suggestions for Future Work ........ 122

6.1 Summary ........ 122

6.2 Suggestions for Future Work ........ 123

6.2.1 In Nanoparticles for Plasmonics........124

6.2.2 Single Crystalline GaAs Overgrowth........125

6.2.3 Ga Nanoparticles: Catalyst for Si Nanowire growths........126

6.2.4 Ga/GaN and In/InN Core-shell Quantum Dot structures........126

6.2.5 Growth of pure ZB GaN Nanowires........127

6.3 References ........ 139

Appendices ........ 141

## List of Figures

Figure 1.1 A schematic diagram illustrating localized surface plasmon resonance (LSPR) of metallic NPs induced by electric field. Reprinted figures with permission from K. A. Willets and R. P. Van Duyne, *Annu. Rev. Phy. Chem.* **58**, 267 (2007)……………………….. ……………………………………….............13

Figure 1.2 A plot of localized surface plasmon resonance (LSPR) energy vs. average diameter of various metallic nanoparticles (NPs) including Ga, Au, Ag, In, Na, and Ni. The plot reveals that LSPR energies of metallic NPs decrease with increasing average diameter of NPs. Especially, LSPR energies of Ga NPs are tunable in the wide range 0.8 to 5.8 eV. Reprinted figure with permission from Myungkoo Kang Ph.D. thesis, University of Michigan, Ch.1, 2014…........... 14

Figure 1.3 Plots of calculated and measured localized surface plasmon resonance (LSPR) energy vs. average diameter of Ga NP. The calculations assume that a Ga NP is either in GaAs or on GaAs and GaN. The plot reveals that Ga LSPR energies range from 0.8 to 2.5eV, showing a decreasing trend with increasing diameter of NPs........................................................................................................ 15

Figure 1.4 a schematic illustration of a semiconductor band diagram where the photoexcitation and recombination processes occur. (a) carrier excitation by incident photon energy, (b) electron-phonon thermallization, (c) band-to-band radiative recombination, (d) trap-assisted recombination (Shockely-Read-Hall recombination), and (e) Auger recombination............................................... 16

Figure 1.5 Schematic diagrams of metallic NP LSPR-utilized (a) light emitting device, Reprinted figures with permission from M. Stockman, *Nat. Mater.* **3**, 423 (2004), (b) solar cell, Reprinted figures with permission from V. E. Ferry *et al.*, *Adv. Mater*. **22**, 4794 (2010), (c) metamaterial, Reprinted figures with permission from A. Alu *et al., Opt. Exp.* **14**, 1557 (2006), and (d) biosensor, Reprinted figures with permission from S. Gao *et al.*, *Adv. Funct. Mater.* **20**, 78 (2010)…………………...…………………………………….………………..17

Figure 1.6 Schematic band diagram of GaN/InGaN heterostructures. (a) WZ structures: built-in polarization field slows carrier dynamics. (b) ZB structures: built-in polarization field is screened…………………………………………………18

Figure 1.7 Schematic MBE growth processes for GaN QDs, NW, and films. Using various surface treatments and Ga deposition parameters, polycrystalline, ZB, and WZ GaN QDs on Si(001), r-$Al_2O_3$, Si(111), and c-GaN substrates were fabricated via DE method. In addition, using a two-step growth method of Ga pre-

deposition followed by GaN growth, ZB and WZ mixed phase of GaN NWs and films were grown……..…………………………………………………19

Figure 2.1 (a) Schematic of NOVA 200 dual beam workstation, and (b) schematic of relative orientations of the electron beam, the ion beam, and the sample surface normal (dashed line). The electron beam angle of incidence, $\theta_e$ is defined as the angle between the incident electron beam and the sample surface normal. The ion beam angle of incidence, $\theta_I$, is defined as the angle between the incident ion beam and the sample surface normal. The angle between the ion and electron beam column is fixed at 52°. Therefore, to achieve normal-incidence FIB irradiation, $\theta_I$=0°, the sample must be tilted to 52° with respect to the electron beam. The angle between the electron beam column and secondary electron detector is 90°. Reprinted figure with permission from Myungkoo Kang Ph.D. thesis, University of Michigan, Ch.2, 2014 .................................................. 36

Figure 2.2 Schematic (top-down view) of the Modified Varian Gen II molecular beam epitaxy system used in this thesis study. Ga, Al, In, Si, Be, Bi and As solid sources, and rf $N_2$ plasma source are located in the effusion cell ports. Reprinted figure with permission from Simon Huang Ph.D. thesis, University of Michigan,Ch.2,2015...........................................................................37

Figure 2.3 Schematic of (a) straight and (b) bended piezoelectric tube during AFM tip scanning on a flat surface. The laser reflection from the tip to the photodiode is indicated by the red line with an arrow. Reprinted figure with permission from Simon Huang Ph.D. thesis, University of Michigan, Ch.2, 2015.. ................ 38

Figure 3.1 Light-matter interactions at the interface of metal and semiconductor: (a) Absorption enhancement in plasmonic metal-semiconductor hetero-structures by localizing the incident field. Reprinted figures with permission from X. Lu *et al. Rev. Phys. Chem.* **60**, 167 (2009). (b) Plasmon-induced resonant energy transfer (RET) from metal to semiconductor, leading to charge separation in semiconductor. Reprinted figures with permission from S.K.Cushing *et al. The Electrochemical Society Interface* **66** (2013). (c) plasmon-induced direct electron transfer (DET) from metal(semiconductor) to semiconductor(metal), Reprinted figures with permission from S.K.Cushing *et al. The Electrochemical Society Interface* **66** (2013). (d) Semiconductor energy transferred to metal SP, leading to enhanced decay rate through semiconductor-SP coupling. Reprinted figures with permission from K. Okamoto *et al. Appl. Phys. Lett.* **87**, 071102 (2005)......................................................................................................... 56

Figure 3.2 A schematic diagram depicting the fabrication of embedded GaAs:Ga nanocomposites: (a) 2D close-packed Ga NP arrays using FIB system (left), SEM images collected from the Ga NP arrays fabricated on GaAs at $\theta_i$ = 30° and 52° (right-top), and cross-sectional TEM image of FIB-fabricated Ga NP showing Ga rich amorphous layer between Ga NP and GaAs (right-bottom). (b) MBE GaAs overgrowth of Ga NP arrays (left), concentric ring RHEED patterns collected during GaAs overgrowth (right-top), and a schematic diagram of

cross-sectional structure of embedded GaAs:Ga nanocomposites (right-bottom)... 57

Figure 3.3 AFM images of unpatterned regions (left), FIB-patterned regions at $\theta_{ion} = 52°$ (middle), and FIB-patterned regions at $\theta_{ion} = 30°$ (right) for NP depth of (a) 0nm (i.e. as-FIB NP), (b) 20nm, (c) 50nm, (d) 100nm, (e) 200nm, and (d) 500nm, with corresponding fast Fourier transforms (FFTs) as insets. For $d_{Ga}$ = 40 nm ($\theta_{ion} = 52°$) NP arrays with depths of 0 - 100 nm, elongated close-packed surface arrays are observed, containing hexagonal FFT patterns including split center spots. For $d_{Ga}$ = 40 nm NP arrays with depths of 500nm and $d_{Ga}$ = 66 nm $\theta_{ion} = 30°$) NP arrays with depths of 0 – 500nm, circular FFT patterns are observed, indicating an isotropic distribution of surface features... 58

Figure 3.4 cross-sectional HRTEM images of embedded GaAs:Ga nanocomposite with $d_{Ga}$=40nm and NP depth=500nm. The GaAs overgrown layer exhibits polycrystalline structure. 59

Figure 3.5 GaAs PL intensities for both patterned regions with $d_{Ga}$=40nm and 66nm (green and blue line), in comparison with that from the unpatterned regions (black dashed line), for NP depth of (a) 50 nm, (b) 100nm, (c) 200nm, and (d) 500nm. The GaAs NBE emission, including BtB emission at 1.515 eV and DAP emission at 1.491 eV, are apparent. For $d_{Ga}$=40nm (66nm), DAP and BtB emissions are enhanced (reduced) in the presence of Ga NPs whose depths are ≤100nm. For NP depth of 200nm, the emission intensity is reduced for the patterned region, in comparison to the unpatterned region. For NP depth=500nm, the PL spectra from the patterned and unpatterned regions are similar.. 60

Figure 3.6 NP depth dependence of RMS roughness (left) and TIS (right) for the unpatterned regions (black dashed line) and patterned regions with $d_{Ga}$=40nm and 66nm (green and blue line). 61

Figure 3.7 PL enhancement mechanisms considered in the GaAs:Ga nanocomposites (a) Absorption enhancement induced by localized EM field due to LSPR of Ga NPs. (b) LSP-excitation via RET from Ga NP to GaAs. (c) SE rate enhancement through LSP coupling. 62

Figure 3.8 schematic diagrams of FDTD absorptance simulation geometries. The simulation volume is a cube of 1 $\mu m^3$ of GaAs with a 25nm-thick vacuum layer on the top. The hemi-spheroidal Ga NP arrays are buried at different depths ranging from 20 to 500 nm below the GaAs surface. (a) Ga NP arrays in vacuum, (b) GaAs with hole arrays at the position of Ga NP arrays, and (c) GaAs with Ga NP arrays. 63

Figure 3.9 The simulated absorptance for (a)–(e) $d_{Ga}$=40nm and (f)-(j) $d_{Ga}$=66nm at the NP depths of 20nm, 50nm, 100nm, 200nm, and 500nm. It is apparent that the absorptance of the Ga NP arrays shows maxima between 1 and 3eV, coinciding

with the reported LSPR of Ga NPs on GaN (1.5 – 2.4eV) and on GaAs (1.4 – 2.0eV)........................................................................................................ 64

Figure 3.10 (a) the absorptance spectrum of the nanocomposite (black line) and the GaAs matrix with hole arrays in the positions of Ga NP arrays (red line). The vertical dashed line indicated the incident photon energy of 1.956eV. (b) the absorptance spectrum of Ga NP arrays with $d_{Ga}$=40nm and NP depth=100nm. ........................................................................................................ 65

Figure 3.11 (a) NP depth dependence of the absorption enhancement ratio for $d_{Ga}$=40 and 66nm for NP depths ranging from 20 to 500 nm. The enhancement in absorption is decreasing with increasing NP diameter and depth, due to reduction in E-field enhancement induced by NP arrays. (b) plots of total probability of exciting EHP by RET process and incident radiation vs. NP depth. (c) total EHP concentration generated via absorption enhancement and LSP-excitation vs. NP depth........................................................................................................ 66

Figure 3.12(a) a plot of calculated spontaneous emission rate ratio vs. NP depth. The resulting SE rate ratios are below 1, suggesting that the SE rate is decreased with NP arrays, presumably due to the NP size- and depth-dependent $E_{LSPR}$. (b) a plot of the extracted $E_{LSPR}$ from Ga NP absorptance spectra vs. NP depth.(c) a plot of calculated effective permittivity vs. NP size and depth.................... 67

Figure 3.13 the comparison between the measured GaAs PL enhancement ratio and the product of predicted fractions of absorption enhancement, LSP-excitation by RET process, and SE rate enhancement for (a) $d_{Ga}$= 40nm and (b) 66nm vs. NP depth. The decreasing trends of the measured and predicted enhancement ratios with increasing NP depth up to 100nm are similar for both $d_{Ga}$=40nm and 66nm cases. ........................................................................................................ 68

Figure 4.1 Schematic of QD growth via the (left) Stranski-Krastanov (SK) growth mode where 3D islands form as the wetting layer reaches the critical thickness; (right) droplet epitaxy (DE) growth mode where metal droplets are crystallized into semiconductor QDs via exposure to an nitrogen flux.................................... 83

Figure 4.2 (left) Schematic GaN DE growth procedure for c-GaN substrate: 1) sample outgassing at 800°C for 10min in the MBE chamber, 2) Ga droplet formation at 185°C with 0.5ML/s for 10sec, 3) nitridation with 350W 1sccm N plasma at 185°C for 30min, (middle) Schematic GaN DE growth procedure for r-$Al_2O_3$ substrate: 1) sample outgassing at 800°C for 10min in the MBE chamber, 2) Ga droplet formation at 30°C with 0.68ML/s for 5min, 3) nitridation with 350W 1sccm N plasma at 800°C for 30min, (right) Schematic GaN DE growth procedure for Si substrate: 1) thermal oxide desorption at 900°C for 10min in the MBE chamber, 2) Ga droplet formation at 550°C with 0.75ML/s for 10sec, 3) nitridation with 350W 1sccm N plasma at 550, 650 and 720°C for 30min. 84

Figure 4.3 (a) Schematic atomic structure of WZ c-plane GaN, RHEED patterns collected during outgassing along (b) <1100> axis, (c) <2110> axis, during Ga droplet formation along (d) <1100> axis, (c) <2110> axis, and during nitridation along (f) <1100> axis, (g) <2110> axis. .................................................................. 85

Figure 4.4 (a) AFM image of c-plane GaN surface, (b) AMF image of GaN QDs on c-GaN after nitridation, (c) Dark field (top) and Bright field (bottom) HRTEM images of coherent WZ GaN QDs grown on c-GaN. ................................................ 86

Figure 4.5 (a) AFM image of 205ML Ga droplets on r-$Al_2O_3$, (b) AMF image of GaN QDs on r-$Al_2O_3$ after nitridation, (c) GIXRD data with ZB GaN (002) peak at 2theta of 40$^o$, (d) 10K PL data with GaN ZB band edge emission peak at 3.16eV... 87

Figure 4.6 RHEED patterns taken during nitridation steps. (a) concentric ring patterns suggesting polycrystalline GaN grown on Si (001) without thermal oxide desorption. (b) cubic spotty patterns suggesting ZB GaN grown on Si (001) with thermal oxide desorption. (c) hexagonal spotty patterns suggesting WZ GaN grown on Si (111) with thermal oxide desorption. ........................................ 88

Figure 4.7 Schematic atomic structure of (a) Si (001) and (b) GaN (001) along <100> axis and <110> axis. The spheres represent the atoms at the first layer of Si (001) and GaN (001) planes with the lattice parameters of 0.543nm for Si and 0.452nm for GaN. ........................................................................... 89

Figure 4.8 RHEED patterns of the sample grown on thermally cleaned Si (001), collected during (a) Si surface along Si<100> axis, (b) Si surface along Si<110>, (c) 7.5ML Ga droplet deposition along Si<100> axis, (d) 7.5ML Ga droplet deposition on along Si<100> axis, (e) nitridation on along GaN <100> axis, and (f) nitridation on along GaN <110> axis. ...................................................... 90

Figure 4.9 AFM images of (a), (e), and (i) for Ga droplets on Si, and (b)-(d), (f)-(h), and (j)-(l) for Ga N QDs on Si, (a) $T_{Ga}$=550$^{\circ}$C, (b) $T_{nit}$=550$^{\circ}$C, (c) 650$^{\circ}$C, (d) 720$^{\circ}$C for Si (001) without oxide desorption, (e) $T_{Ga}$=550$^{\circ}$C, (f) $T_{nit}$=550$^{\circ}$C, (g) 650$^{\circ}$C, (h) 720$^{\circ}$C for Si (001) with oxide desorption, and (i) $T_{Ga}$=550$^{\circ}$C, (j) $T_{nit}$=550$^{\circ}$C, (k) 650$^{\circ}$C, (l) 720$^{\circ}$C for Si (111) with oxide desorption. ............................... 91

Figure 4.10 The corresponding GaN QD size distributions (a) GaN QDs grown on Si (001) without oxide desorption from Fig. 4.6(a)-(c), (b) GaN QDs grown on Si (001) with oxide desorption from Fig. 4.6(d)-(g), and (c) GaN QDs grown on Si (111) with oxide desorption from Fig. 4.6(h)-(j). The Frequency is the percentage of islands with diameters within a specified range. ........................................... 92

Figure 4.11 Plots of the (a) density, (b) mean diameter, and (c) mean height of Ga droplets and GaN QDs grown at 550, 650, and 720$^{\circ}$C. ................................................ 93

Figure 4.12 Plots of the GaN QD volume per unit area estimated from QD density, diameter and height. The estimated GaN QD volume values are in the range from 1.5E14 to 4E14 $nm^3/cm^2$, independent on nitridation temperature. ............................ 94

Figure 5.1 The GaN morphologies plot of (a) $T_{substrate}$ and (b) growth rate vs. Ga BEP, where of red dots (black squares) denote NW (film). The GaN morphology consists in NWs in the regime of Ga BEP $<0.3\times10^{-7}$ Torr and $T_{growth}$ <800°C. At higher Ga BEP and $T_{growth}$, GaN grows in films. The growth rate increases with increasing Ga BEP until ~$0.9\times10^{-7}$ Torr, and saturates at the Ga BEP exceeding $0.9\times10^{-7}$ Torr. .......... 110

Figure 5.2 (a) Schematic illustrations of GaN growth at 800°C with N/Ga flux ratio=33. First, the clean Si surface is exposed to a Ga BEP of $0.3\times10^{-7}$ Torr for 3 min, followed by 3hrs GaN growth with the same Ga BEP and a N flux of $1.0\times10^{-6}$ Torr. (b) During the Ga pre-deposition step, streaky RHEED patterns of (1×1) Si surface in the $[110]_{Si(001)}$ azimuth were observed. (c) During the GaN growth step, broken ring RHEED patterns were observed in the $[1100]_{WZ\text{-}GaN}$ azimuth. (d) the XRD scan, with the tilted SEM image as an inset .......... 111

Figure 5.3 (a) Schematic illustrations of GaN growth at 800°C with N/Ga flux ratio<13. First, the clean Si surface is exposed to a Ga BEP of $0.9\times10^{-7}$ Torr for 3 min, followed by 3hrs GaN growth with the same Ga BEP and a N flux of $1.0\times10^{-6}$ Torr. (b) during the Ga pre-deposition step, diffuse RHEED patterns were observed. (c) RHEED patterns taken during the GaN growth step after 23 min (top) and 2 hr (bottom). (d) cross-sectional SEM image. .......... 112

Figure 5.4 (a) XRD data with peaks at 2θ = 34.7°, 37.1°, and 40.0°, corresponding to WZ-GaN (002), WZ-GaN (101), and ZB-GaN (200) planes, respectively, revealing the presence of mixed phase of WZ and ZB. (b) LIBAD scans at $\theta_i$ = 1° (blue), 5° (red), and 8°(black). For $\theta_i$ = 1°, only WZ diffraction peaks are observed, revealing that the top of GaN consists of WZ phase. With increasing $\theta_i$ exceeding 5°, the ZB diffraction peak at 2θ = 40.0° is observed, suggesting that ZB phase is buried in the film. .......... 113

Figure 5.5 (a) Schematic illustrations of GaN growth at 800°C with high Ga flux during Ga supersaturation, followed by low Ga flux during GaN growth. First, the clean Si surface is exposed to a Ga BEP of $0.9\times10^{-7}$ Torr for 3 min, followed by 3 hrs GaN growth with Ga BEP of $0.3\times10^{-7}$ Torr and N flux of $1.0\times10^{-6}$ Torr. (b) during the Ga pre-deposition step, diffuse RHEED patterns were observed. (c) RHEED patterns taken during the GaN growth step after 10 min (top) and 2 hr (bottom). (d) tilted SEM image, showing formation of 188±9nm-thick GaN NWs. .......... 114

Figure 5.6 (a) XRD data with peaks at 2θ = 33.1°, 34.7°, 37.1°, and 40.0°, corresponding to WZ-GaN (100), WZ-GaN (002), WZ-GaN (101), and ZB-GaN (200) planes, respectively, revealing the presence of mixed phase of WZ and ZB. (b) GIXRD scans at $\theta_i$ = 1° (blue), 5° (red), and 8°(black). For $\theta_i$ = 1°, only WZ diffraction peaks are observed, revealing that the top of GaN consists of WZ phase. With increasing $\theta_i$ exceeding 5°, the ZB diffraction peak at 2θ = 40.0° is observed, suggesting that ZB-WZ phase transformation occurs at 150nm thickness... 115

Figure 5.7 PL spectra at 10K for a WZ NW (blue line), ZB-WZ mixed film (black line), and ZB-WZ mixed NW (green line). For the WZ NW, the spectrum is dominated by an emission at 3.47eV corresponding to excitonic transitions of WZ GaN. For the ZB-WZ film, the emission 3.16eV is apparent, which is attributed to donor-acceptor-pair (DAP) transitions of ZB GaN, without the emissions related to WZ GaN. For the ZB-WZ mixed NW, four resolved emission peaks at 3.47eV, 3.41eV, 3.32eV, and 3.16eV are observed. The emissions at 3.47 eV and 3.41 eV are attributed to the excitonic transitions and DAP transitions of WZ GaN, respectively. In addition to the WZ GaN emissions, the emissions related to ZB GaN DAP transitions around 3.3eV and excitonic transitions at 3.16eV are apparent. ............................................ 116

Figure 5.8 Proposed band alignment of ZB and WZ GaN, inducing the capture of electrons in relatively low ZB conduction band and their recombination with holes in ZB valence band ……………..……………………………………………..……...….117

Figure 6.1 SEM images of In droplets deposited on Si (001) (a) 3ML, (b) 4ML, (c) 5ML, (d) 6.5ML, and (e) 8ML, with the corresponding In droplet size distributions on right sides.......................................................................................................... 129

Figure 6.2 Plots of (a) simulated and (b) measured absorption efficiency (effective absorption cross-section of In droplet / geometrical cross section of In droplet) vs. Energy with various In diameter ranging from 10 to 63nm. ............................................ 130

Figure 6.3 Comparison of the $E_{LSPR}$ collected from ellipsometry experiments and FDTD absorption simulations vs. In droplet diameter. LSPR energy of In droplets on Si (001) ranges from 5 to 6eV, showing redshift with increasing In droplet size.. 131

Figure 6.4 SEM images of (a) FIB-Ga NPs on GaAs and (b) GaAs overgrowth with V/III of 10, with the kinetic Monte-Carlo (KMC) simulation result showing surface protrusions. ........................................................................................ 132

Figure 6.5 KMC simulation results with various V/III incorporation rate ratios ranging from 1.5 to 10. The color codes are depicted in the right side: (green) As from substrate, (red) Ga from NP and substrate, (violet) Ga deposited, and (bright blue) As deposited......................................................................... 133

Figure 6.6 Schematic illustration of Single crystalline GaAs overgrowth using MBE-fabrication of Ga droplets, followed by *in situ* MBE GaAs overgrowth........... 134

Figure 6.7 (a) A cross-sectional scanning electron micrograph of a Ge (111) substrate decorated with discrete liquid Ga droplets. (b) Same as (a) but after 60 s ec-LLS process. Reprinted figures with permission from E. Fahrenkrug *et. al. Nano Lett.* **14**(2) 847 (2014). Copyright 2014 by ACS Publications. ................... 135

Figure 6.8 Schematic chamber modification design for *in situ* FIB source, including a custom clamp and a UHV spacer. The custom clamp is for reducing the vibrational interferences, providing a mechanical stability between the FIB

column and sample surfaces. This *in situ* system enables oxide-free sample preparations. ........................................................................................ 136

Figure 6.9 Schematic illustration of FIB-directed Epitaxial Core-Shell Nanostructures: 2D array of metal-semiconductor epitaxial core-shell nanostructures with Ga droplet cores and a surrounding GaN......................................................................... 137

Figure 6.10 Schematic illustration of GaN NW growth via two-step MBE process: 1) small sized GaN QD formation for seeds, 2) epitaxial growth of GaN NWs............ 138

Figure A.1 (a) GIXRD scans of a GaAs (001) substrate and overgrown GaAs layers in the thickness range 20 nm to 500 nm, using a monochromatic Cu-Kα ($\lambda$ = 1.5405 Å) rotating anode operated at 40 kV and 100 mA. For all overgrown layers, peaks at 2θ of 27.3°, 45.3° and 53.7°, corresponding to GaAs (111), (220) and (311) planes, are apparent. (b) The calculated grain sizes and fractions of GaAs (111) planes, $f_{(111)}$, for the thickness ranging from 20 nm to 500 nm. For overgrown layer thicknesses up to 100 nm, the grain size ($f_{(111)}$ value) is 6.7 ± 0.7 nm (0.45 ± 0.03). For overgrown layer thicknesses beyond 100nm, the grain size ($f_{(111)}$ value) increases up to (decreases down to) 15.2 ± 0.1 nm (0.24)............................... 142

Figure B.1 Plots of effective permittivity of GaAs:Ga nanocomposites vs. NP buried depth, using Maxwell-Garnett effective medium approximations. The observed diameter, height, and density of Ga NP arrays are used to estimate NP volume fractions.146

Figure B.2 Plots of calculated $E_{LSPR}$ with the effective permittivity values of GaAs:Ga nanocomposites vs. NP depth. In the cases of larger NP sizes and thicker NP buried depths, it is evident that $E_{LSPR}$ is redshifted.................................................... 147

Figure D.1 (a) the simulated energy-dependent absorptance of bulk GaAs (at 300K), exhibiting the absorption at 1.42eV presumably corresponding to the GaAs bandedge. (b) the simulated energy-dependent reflectance spectrum of bulk GaAs at 300K (red line), in comparison to the measured reflectance reported by H. R. Phillip et al. (black dashed line). Reprinted figures with permission from H. R. Phillip *et. al. Phys. Rev.* **129** (4) 1550 (1963). Copyright 1963 by American Physical Society. ............. 152

Figure F.1 Plots of energy-dependent $\varepsilon_{Ga}$, (top) real parts of dielectric constant, (bottom) imaginary parts of dielectric constant......................................................... 156

Figure F.2 Plots of energy-dependent $\varepsilon_{GaAs}$.................................................................. 157

Figure G.1 A Plot of incident angle-dependent information depth of GaN with 0.154nm X-ray radiation.......................................................................................... 160

**List of Tables**

Table F.1 GaAs Materials Parameters…………………………………………..............155

Table H.1Samples of GaAs overgrowth on Ga droplets................................................ 162

Table H.2 Samples of GaN QDs grown in c-plane GaN from Kyma Technologies...... 163

Table H.3Samples of GaN QDs grown on Si substrates. .............................................. 164

Table H.4 Samples of GaN films and NWs grown on Si substrates….………………..165

## List of Appendices

**Appendix A NP depth-dependent crystallinity of GaAs overgrown layer** ................... 141

**Appendix B Maxwell-Garnett Effective Medium Theory** ............................................ 144

**Appendix C Lumerical FDTD simulation codes** ....................................................... 149

**Appendix D Validation of Lumerical Absorptance Simulations** .............................. 151

**Appendix E Size Analysis of Droplets and Quantum Dots** ....................................... 154

**Appendix F Materials Parameters** ................................................................................. 155

**Appendix G Refraction-corrected Information depth** .............................................. 159

**Appendix H List of Samples** ........................................................................................... 162

**Abstract**

**Gallium Metallic Nanoparticles for Plasmonics and Droplet Epitaxy: Formation and Properties**

**by**

**Sunyeol Jeon**

**Chair: Rachel S. Goldman**

The development of new materials in nanophotonics, defined as the use of multiscale materials to control light-matter interactions, has proven to be the foundation for revolutionary advances in both science and technology. In this thesis, we utilize Ga droplets as a plasmonic metal nanoparticle (NP) as well as a seed for droplet epitaxy of ZB GaN nanostructures, and examine the formation of embedded GaAs:Ga nanocomposites and ZB GaN nanostructures, and their structural and optical properties.

Metallic nanostructures generate surface plasmons an incident electromagnetic wave, leading to enhancements in absorption and emission. However, materials research and device fabrication have focused nearly exclusively on 2-dimensional dispersions of Ag and Au formed on surfaces, with plasmon resonances limited to visible wavelengths. Thus, it is necessary to explore a new plasmonic materials, which cover wide wavelength ranges. Here, we examined the formation of embedded Ga NP arrays and their influence on GaAs

near-band edge (NBE) photoluminescence (PL) efficiency using ion beams and molecular beam epitaxy. Using a combined computational-experimental approach, we revealed new insight into the influence of the embedded NPs on the PL of GaAs. This approach provides an opportunity to enhance the PL efficiency from a variety of semiconductor heterostructures, using a seamless approach to embed non-noble metals during epitaxy.

GaN is of interest for optoelectronic applications. However, GaN typically crystallizes in a wurtzite (WZ) structure, exhibiting piezoelectric properties leading to a reduced probability for recombination of electrons and holes and consequently limit the performance of devices. Thus, interest in polarization-free zinc-blende (ZB) GaN nanostructures is rapidly increasing. In this thesis, we first demonstrate the growths of ZB GaN nanostructures via droplet epitaxy (DE). By varying the surface conditions of substrates and nitridation processes, GaN QDs were grown polycrystalline, WZ, and ZB. We observe a one-to-one conversion from Ga droplets to GaN QDs when the Ga deposition and nitridation temperatures are equal at 550°C and a Ga droplet coalescence during nitridation at elevated nitridation temperatures. Furthermore, we examined the growth of ZB-WZ mixed NW growth via controlling $SiN_x$ interlayer formation, using a two-step MBE growth method of Ga pre-deposition followed by GaN growth on Si (001). We demonstrate, for the first time, a growth process consisting of pre-deposition at high Ga flux, followed by GaN growth at low Ga flux, thereby resulting in GaN NW ensembles with a significant ZB content.

# Chapter 1

# Introduction

## 1.1 Overview

The development of new materials in nanophotonics, defined as the use of multiscale materials to control light-matter interactions, has often proven to be the foundation for revolutionary advances in both science and technology. The need for novel nanostructures of metals, semiconductors and their composites has increased due to their variety of functionalities and unique applications in nanophotonics. Here, utilizing Ga droplets as a metal nanoparticle (NP) and a seed for GaN epitaxial growth, we report formation and properties of a new plasmonic nanocomposite and a zinc-blende (ZB) GaN nanostructures.

For metallic nanostructures, surface plasmons are generated under an incident electromagnetic wave, and this phenomenon has been applied in areas of solar energy harvesting, optical sensing, negative refractive index metamaterials, and light generation. Localized surface plasmon resonance (LSPR) is an optical phenomenon generated by a light wave trapped within conductive metallic nanoparticles (NPs) with a radius smaller than the wavelength of light, as shown in Fig. 1.1.[1] The interaction between the incident light and surface electrons produces coherent localized plasmon oscillations with a resonant frequency that strongly depends on the composition, size, geometry, dielectric

environment, and particle–particle separation distance of NP arrays. The intense and localized electromagnetic (EM) fields induced by LSPR lead to enhanced optical properties of surrounding media. To date, materials research and device fabrication have focused nearly exclusively on Ag and Au NP dispersions in two dimensions,[2,3,4,5] with plasmon resonances limited to visible wavelengths.[6] On the other hand, Ga NPs, with LSPR quality factors comparable to those of Ag and Au,[7,8] and plasmon energies tunable from the infrared to the ultraviolet wavelength ranges, have been reported, as shown in Fig. 1.2 and Fig. 1.3.[8,9,10] Furthermore, close-packed surface arrays of Ga NP were recently demonstrated using ion-irradiation of semiconductor surfaces.[8,11] In this thesis, we explore a new plasmonic material Ga fabricated via focused ion beam irradiation followed by molecular beam epitaxy overgrowth for enhancing energy conversion efficiencies of semiconductors. Here, we report formation and properties of GaAs:Ga nanocomposites.

For semiconductor nanostructures, quantum dots (QDs) and nanowires (NWs) are expected to exhibit novel electrical and optical properties that differ from those of conventional bulk and thin-film semiconductor materials. Among semiconductor materials, GaN is of large interest for future optoelectronic devices due to its direct wide band gap, operating in the blue to the near ultraviolet wavelengths.[12,13,14,15] The fabrication of GaN QDs has been extensively investigated, and the most frequently used approach is the self-assembly process in Stranski-Krastanov (SK) growth mode, which requires sufficient lattice mismatch, and usually results in a 2D wetting layer.[16,17] An alternative growth approach is GaN droplet epitaxy (DE) which allows dot size and density manipulation by tuning the amount of deposited Ga and the substrate temperature,[18,19] suggesting the possibility of QD formation on any substrate. For GaN NWs fabrication, two approaches

have been used, a top-down approach in which a sequence of GaN layers is etched by e-beam lithography and reactive ion etching into wires,[20, 21, 22] and a bottom-up approach in which GaN is grown directly in the form of NWs.[23, 24, 25, 26] While the top-down approach is limited by the low productivity and resolution of e-beam patterning, the self-assembling bottom-up approach can efficiently produce a large number of wires with high aspect ratio. This bottom-up approach usually utilizes metal-droplet catalyst for seeds in which the atoms and molecules of the impinging flux are solved and condensed at the solid interface by the well-known vapor-liquid-solid (VLS) mechanism.[27] However, the use of an external metal catalyst has the disadvantage of a possible undesirable doping of GaN NWs. Therefore, a catalyst-free or self-catalyst growth of NWs is preferable, and this can be achieved by adjusting the growth parameters. In this thesis, we demonstrate the selective growth of WZ and ZB GaN QDs, films and NWs via control of substrates and MBE growth parameters. We discuss the influence of surface treatments, nitridation temperatures, and Ga fluxes on the structural and optical properties of GaN nanostructures.

This chapter opens with a description of light-matter interactions in metals and semiconductors. We then discuss Ga nanoparticles as a new plasmonic material and a seed material for GaN nanostructures. Finally, this chapter concludes with an outline and objectives of the dissertation

## 1.2 Nanostructured Materials: Light-matter Interactions

### 1.2.1 Localized Surface Plasmon Resonances in Metal Nanoparticles

When electromagnetic (EM) radiation is incident upon metallic NPs, collective oscillations, termed LSPR, are generated.[28] Recently, noble metal NP-semiconductor interfaces have shown significant promise for light absorption and emission applications.[29,30,31,32,33,34,35,36,37] Metallic NPs in semiconductors generate LSPR depending on particle size, shape, the refractive index of the NPs and semiconductors, and the material geometry of NPs and semiconductors,[49,52,55,38] leading to enhanced light absorption[39] and emission.[51,56] The NP-induced localized field enhances light absorption in the semiconductor at energies close to the LSPR energy ($E_{LSPR}$), resulting in enhanced electron-hole pair (EHP) generation.[40] In the light emission process, when $E_{LSPR}$ is comparable to the emission energy of the semiconductor, the spontaneous emission (SE) rate in the semiconductor is enhanced depending on the geometry of semiconductor and metal, such as the separation distance between the semiconductor and metal, leading to radiative recombination enhancement.[56,59] In addition, if $E_{LSPR}$ is greater than the band gap energy of the semiconductor, the NPs act as a source to excite EHP in the semiconductor by a resonant energy transfer (RET) process, consequently resulting in enhanced emission.[41,42] On the other hand, NP-induced emission reduction has been observed depending on the band structures of NPs and semiconductor due to a direct electron transfer (DET) from the semiconductor to the NPs when they are directly in contact.[43,44]

### 1.2.2 Light Absorption and Emission in Semiconductors

For semiconductors, a photon with energy larger than the band gap energy of a semiconductor, $E_g$, can be absorbed in a semiconductor, resulting in electron-hole pair

(EHP) generation in the conduction band and valence band, respectively. N the other hand, when EHP pairs are generated in a semiconductor or carriers are excited into higher impurity levels from which they fall to their equilibrium states, light emission or luminescence occurs. If carriers are excited by photon absorption, the radiation resulting from the recombination of the excited carriers is called photoluminescence (PL). For a steady state, the rate of carrier generation by photon absorption equals the rate of recombination of photoexcited carriers.[45] Recombination of the photoexcited carriers is a process by which both electrons and holes annihilate each other, consisting of radiative recombination and non-radiative recombination. Figure 1.4 presents a schematic illustration of a semiconductor band diagram where the photoexcitation and recombination processes occur. When light of a photon energy greater than the band gap energy of a semiconductor, (a) carrier excitations are created, and they relax their energy through the following steps: (b) electron-phonon thermallization, (c) band-to band radiative recombination, (d) trap-assisted recombination (Shockely-Read-Hall recombination), and (e) Auger recombination. The total carrier recombination process consists of radiative recombination and nonradiative recombination (SRH recombination and Auger recombination).

$$PL\ intensity\colon I(t) = -\frac{dn}{dt} = \left(\frac{1}{\tau_{rad}}\right)n = \frac{B}{N}n^2 \tag{1.1}$$

In a PL process, excess photoexcited electrons and holes decay by electrons demoted from the conduction band to empty states (holes) in the valence band. Energy lost by an electron transition is given up as a photon via radiative recombination in Eq. 1.1. This radiative recombination occurs spontaneously, and the rate of change in the conduction band electron concentration by radiative recombination is PL intensity.[46,47]

## 1.3 Ga Nanoparticles for Plasmonics

To date, plasmonics research has focused nearly exclusively on noble metals, such as Ag and Au NPs, due to their relatively low absorption losses in the visible spectrum.[48,49,50] However, their SPR energies are limited in the visible spectrum (< 3.5 eV). Also, Ag suffers from SPR damping due to air-induced surface corrosion.[51] Unlike gold and silver, SPR in the range 0.8 to 5.8 eV were recently reported for Ga NPs with average NP diameters ranging from 10 to 300 nm, as shown in Fig. 1.2,[52,53,54,55] exhibiting plasmonic activity in the ultraviolet. Furthermore, a comparison of literature reports for the optical constants of liquid (amorphous) Ga and Ag NPs reveals conductivity values which are of the same order of magnitude, presumably leading to low dissipation losses for Ga.[55] Thus, both the plasmon resonance tuning and the low dissipation losses for Ga NPs are very promising for plasmonic nanomaterials. Recently, close-packed surface arrays of Ga NP were demonstrated using ion-irradiation of semiconductor surfaces.[8,10,11] In addition, the influence of Ga NP diameter-dependent LSPR on GaAs near-band edge (NBE) PL has been reported, as shown in Fig. 1.3.[10] The GaAs PL enhancement induced by surface Ga NP arrays is attributed to the enhancement of incident EM field, leading to absorption enhancement in the GaAs. Furthermore, there has been growing research interest in NP assembly, whose optical response can be modulated by controlling the inter-particle distance and the spatial arrangement of NPs. In this regard, three-dimensional (3D) NP assemblies, where NPs do not lie on a single plane, multiple plasmonic coupling is expected to give rise to hybridized plasmon mode formation.[56] Although the influence of three-dimensional NP arrays of ErAs embedded in GaAsSb on infrared absorption in

semiconductors has been reported,[57] their influence on infrared emission has yet to be considered. In this thesis, we explore the formation and optical characterization of embedded GaAs:Ga nanocomposites fabricated by focused-ion beam (FIB) irradiation followed by MBE overgrowth. We use a combination of experiments and computations to determine the influence of the Ga NP diameter ($d_{Ga}$) and NP depth (i. e. overgrown layer thickness) on the enhancement of GaAs near-band-edge (NBE) emission, revealing a physical mechanism based upon NP-induced absorption enhancement, EHP generation by LSP-excitation, and SE rate reduction.

### 1.4 GaN Nanostructures for Optoelectronics

Due to its direct wide bandgap, GaN is of interest for high temperature electronic and visible optoelectronic applications.[58] GaN typically crystallizes in a wurtzite (WZ) structure,[59] but zincblende (ZB) GaN has also been reported, offering several advantages over WZ GaN, including higher carrier mobilities[60,61] and lower bandgaps (3.2-3.23 eV[62,63] vs. 3.42 eV). Piezoelectric WZ GaN has potential applications in field-effect transistors tuned by applying stress to the device.[64] However, the built-in piezoelectric and spontaneous polarization of WZ GaN induce a quantum confined Stark effect (QCSE), leading to a reduced recombination probability of electrons and holes and consequently limiting the performance of optoelectronic devices, as shown in Fig. 1.6.[65,66,67] Thus, interest in polarization-free ZB GaN is rapidly increasing.[68,69] To eliminate the QCSE, which leads to a red shift of the luminescence as well as a reduced radiative recombination

rate, nonpolar or semipolar orientations of GaN began to attract attention.[70] The metastable ZB cubic phase of GaN is expected to have no polarization fields.[71,72]

To fabricate group III-nitride QDs using self-assembly, the Stranski-Krastanow (SK) growth method and droplet epitaxy (DE) method have been utilized. For the misfit-driven SK growth, the QD size, density and shape are limited by the lattice mismatch. Thus, ultra-small QDs are not typically possible via the SK method. On the other hand, the DE growth enables more flexibilities for tuning QD sizes, densities, and materials combinations.[73,74,75,76,77,78,79,80] GaN QDs have been achieved by DE on various substrates such as AlGaN on 6H-SiC(0001),[81] c-$Al_2O_3$,[82] Si(111),[83,84,85] and AlN on 3C-SiC(001),[86,87,88] with either a $NH_3$-gas source MBE[87,89] or a N plasma MBE.[88,89,90,91,92,93,93] Since WZ QDs and ZB QDs are reported for growth on 6H-SiC(0001)[88] and 3C-SiC(001),[91,92,93,94] respectively, it appears that the GaN QD crystal structure for DE is determined by the structure of the substrate. Furthermore, the QD density and size may be tailored via variation in the Ga flux for droplet formation,[90,93,94] nitridation temperatures,[88,90,98] and plasma power.[98] Generally, a trend of higher (lower) density and smaller (larger) size with decreasing (increasing) Ga flux[98] and decreasing (increasing) nitridation temperatures[86,88] is reported.

It has been reported that ZB GaN nanocrystals (NCs) were nucleated in GaAs via matrix-seeded growth, with the maximum NC radius of ~1.75 nm.[90] Thus, to obtain ZB GaN, we use the DE process to produce small QDs, which is not possible by the SK approach. To form small-sized and close-packed GaN QDs, we investigated the self-assembly of QDs using Ga droplet deposition, followed by crystallization in the presence of nitrogen species. In this thesis, we have studied the influence of substrate orientations

for epitaxial growth as well as the influence of nitridation temperatures on QD size distribution, as shown in Fig. 1.7.

To date, GaN NWs and films have been grown in the WZ form on Si(001),[91,92,93] Si(111),[94,95,96] and c-$Al_2O_3$,[97] $SiO_2$,[98,99] and GaAs(111).[100] ZB GaN films have been demonstrated on GaAs(001),[101] Si(001),[102] 3C-SiC substrates.[103,104] However, ZB GaN NWs have not yet been reported on any substrates with any growth methods. Alternatively, the ZB phase of GaN is potentially free of polarization fields, which may reduce internal electric fields that can be detrimental to ultraviolet optoelectronic device performance. Typically, on Si (001) substrates, WZ GaN NWs are grown with N-rich conditions,[99] and GaN films are grown in either ZB[107] or WZ[92] using Ga-rich conditions. Although the formation of WZ NWs and films is considered to be related to the formation of a $SiN_x$ interlayer,[98] a predictive method to control $SiN_x$ interlayer formation has yet to be established. In this thesis, we demonstrate the growth of WZ NW vs. ZB-WZ mixed film and NW growth via control of $SiN_x$ interlayer formation, using a two-step molecular beam epitaxy (MBE) process consisting of Ga pre-deposition followed by GaN growth directly on Si (001). We discuss the influence of Ga flux on the formation of various GaN nanostructures, as shown in Fig. 1.7, and their optical properties. For low Ga fluxes, $SiN_x$ formation preceeds the formation of WZ NWs. On the other hand, for high Ga fluxes, the Si surface is Ga-saturated, leading to ZB GaN film and eventually ZB/WZ-layered film formation. Pre-deposition with a high Ga flux, followed by GaN growth with a low Ga flux, results in the formation of mixed ZB/WZ phase NWs. We discuss the optical properties of the films and NWs, presenting photoluminescence spectra consisting of the

GaN ZB donor-acceptor-pair (DAP) emission for films, as well as the emissions related to ZB and WZ DAP and excitonic transitions for NWs.

## 1.5 Dissertation Objectives

The first part of this thesis work focuses on the formation embedded Ga NP size and their influence on GaAs PL efficiency. The influence of the Ga NP size and buried depth on GaAs NBE emission was examined. Close-packed arrays of Ga NPs embedded in GaAs are fabricated using off-normal focused-ion-beam irradiation, followed by molecular-beam-epitaxy. Using a combination of PL spectroscopy and electromagnetic computations, we discuss new insights into PL enhancement mechanisms of GaAs:Ga nanocomposites. This approach provides an opportunity to enhance the PL efficiency from a variety of semiconductor heterostructures, using a seamless approach to embed non-noble metals during epitaxy.

The middle part of this thesis is devoted to selective growths of ZB, WZ, and polycrystalline GaN QDs by DE. The influence of substrates and nitridation temperatures on the crystal structures and size of GaN QDs was examined. GaN QDs were grown on various substrates by the DE method using MBE with nitrogen plasma. In particular, by varying the surface conditions of Si substrates, we first demonstrate selective growth of polycrystalline, ZB, and WZ GaN QDs, and reveal the growth mechanism of Ga droplet coalescence during nitridation.

In the final part of this thesis, we examine the nucleation, transformation, and optical properties of GaN nanostructures. GaN NWs and films were prepared using a two-

step method consisting of Ga pre-deposition followed by nitridation leading to GaN epitaxy on silicon. For low Ga fluxes, $SiN_x$ formation preceeds the formation of the WZ nanowire. On the other hand, for high Ga fluxes, the Si surface is Ga-saturated, leading to ZB GaN film and eventually ZB/WZ-layered film formation. Finally, we demonstrate, for the first time, the formation of mixed ZB/WZ phase NWs via pre-deposition with a high Ga flux, followed by GaN growth with a low Ga flux. We examine the optical properties of the films and NWs, presenting photoluminescence spectra consisting of the GaN ZB donor-acceptor-pair (DAP) emission for films, as well as the emissions related to ZB and WZ DAP and excitonic transitions for NWs.

### 1.6 Dissertation Organization

This dissertation is organized as follows. Chapter 2 describes the experimental procedures used for this thesis work, including focused ion beam (FIB) irradiation, molecular beam epitaxy (MBE), reflection high-energy electron diffraction (RHEED), atomic force microscopy (AFM), scanning electron microscopy (SEM), X-ray diffraction (XRD), and photoluminescence (PL) experiments.

In Chapter 3, we discuss the formation of embedded Ga NP arrays in GaAs using Ga+ focused-ion beam irradiation of GaAs, followed by MBE overgrowth. We use a combination of experiments and computations to determine the influence of the Ga NP diameter ($d_{Ga}$) and NP depth on the enhancement and reduction of GaAs NBE PL efficiency, revealing a physical mechanism based upon NP-induced absorption enhancement, EHP generation by LSP-excitation, and SE rate reduction.

Chapter 4 presents the investigations of the selective formation of ZB, WZ, and polycrystalline GaN QDs using DE. The influence of substrates and nitridation temperatures on the crystal structures of GaN QDs is examined. WZ GaN QDs were grown on c-GaN and Si(111) substrates, while ZB GaN QDs were grown on r-$Al_2O_3$ and Si(001) substrates. We discuss the influence of nitridation temperature QD diameter and density.

In Chapter 5, we demonstrate the growth of WZ NW as well as ZB-WZ mixed film and NW growth via control of $SiN_x$ interlayer formation, using a two-step MBE process consisting of Ga pre-deposition followed by GaN growth. We investigate the influence of Ga flux on the structural and optical properties of GaN nanostructures. We also discuss the optical properties of the films and NWs, presenting photoluminescence spectra consisting of the GaN ZB donor-acceptor-pair (DAP) emission for films, as well as the emissions related to ZB and WZ DAP and excitonic transitions for NWs. Finally in Chapter 6, we present a summary and suggestions for future work.

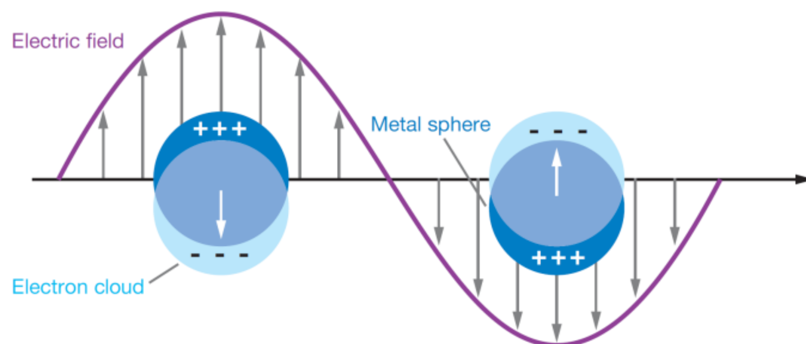


Fig. 1.1 A schematic diagram illustrating localized surface plasmon resonance (LSPR) of metallic NPs induced by electric field. Reprinted figures with permission from K. A. Willets and R. P. Van Duyne, *Annu. Rev. Phy. Chem.* **58**, 267 (2007).

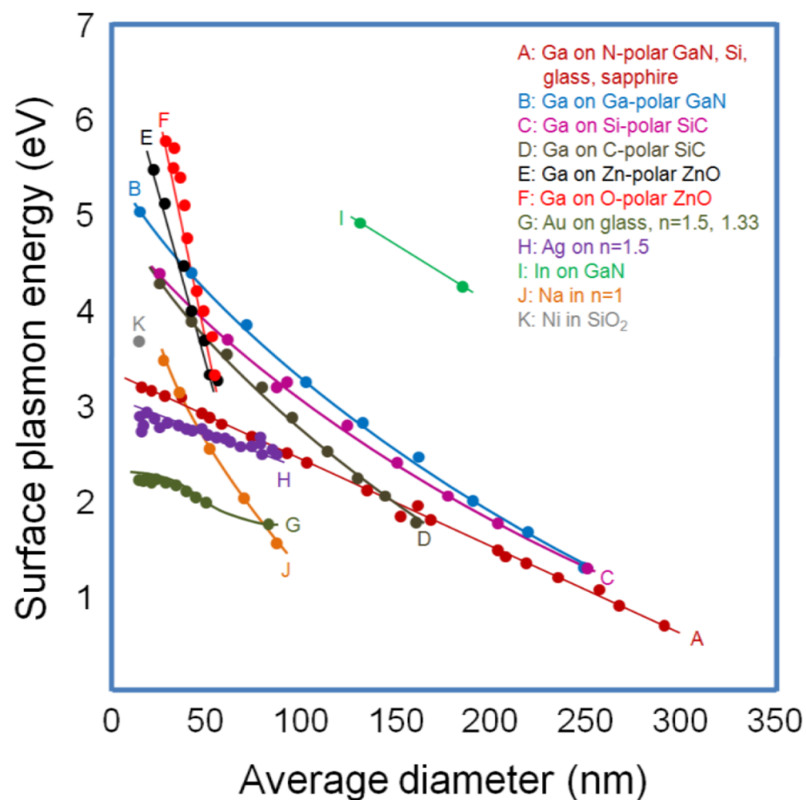


Fig. 1.2 A plot of localized surface plasmon resonance (LSPR) energy vs. average diameter of various metallic nanoparticles (NPs) including Ga, Au, Ag, In, Na, and Ni. The plot reveals that LSPR energies of metallic NPs decrease with increasing average diameter of NPs. Especially, LSPR energies of Ga NPs are tunable in the wide range 0.8 to 5.8 eV. Reprinted figure with permission from Myungkoo Kang Ph.D. thesis, University of Michigan, Ch.1, 2014.

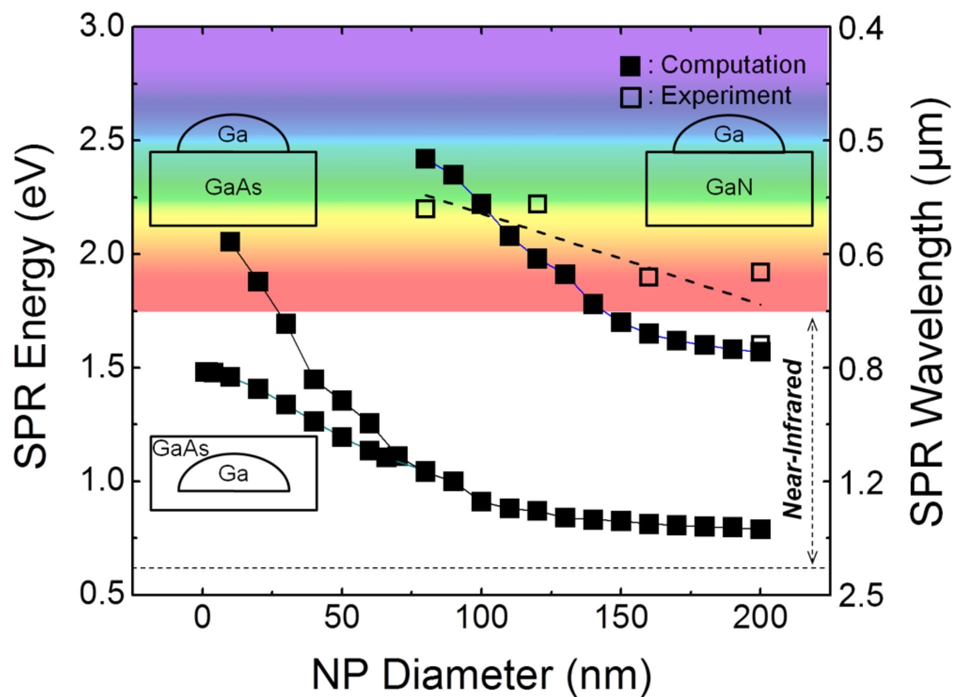


Fig. 1.3 Plots of calculated and measured localized surface plasmon resonance (LSPR) energy vs. average diameter of Ga NP. The calculations assume that a Ga NP is either in GaAs or on GaAs and GaN. The plot reveals that Ga LSPR energies range from 0.8 to 2.5eV, showing a decreasing trend with increasing diameter of NPs.

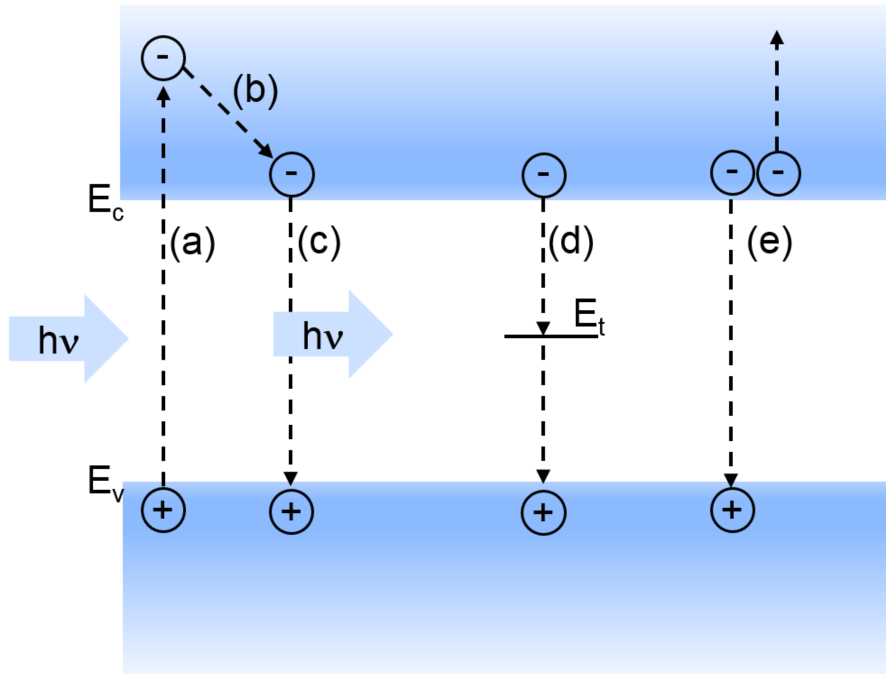


Fig. 1.4 a schematic illustration of a semiconductor band diagram where the photoexcitation and recombination processes occur. (a) carrier excitation by incident photon energy, (b) electron-phonon thermallization, (c) band-to-band radiative recombination, (d) trap-assisted recombination (Shockley-Read-Hall recombination), and (e) Auger recombination.

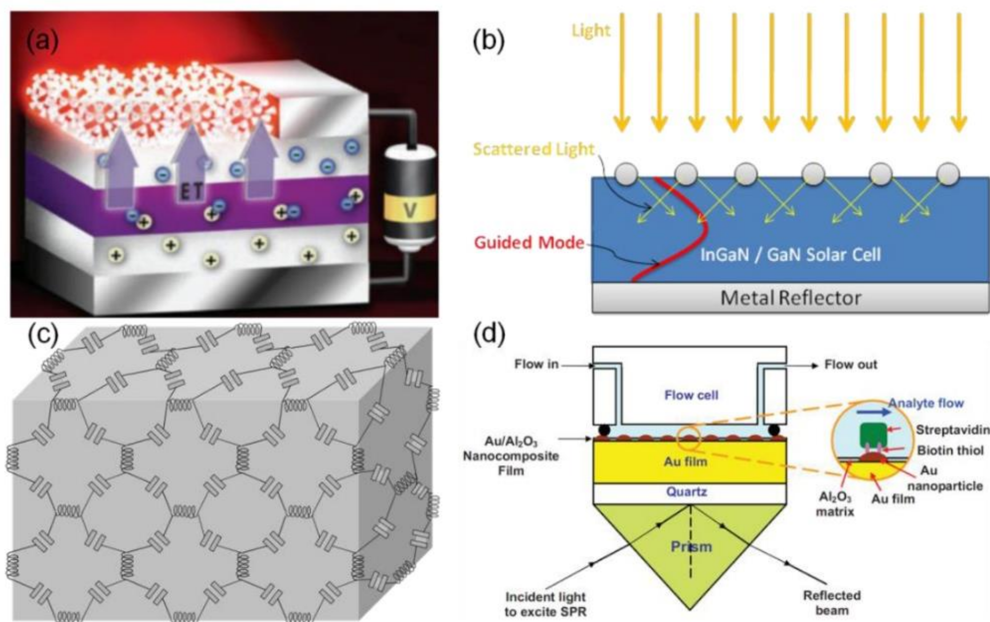


Fig. 1.5 Schematic diagrams of metallic NP LSPR-utilized (a) light emitting device, Reprinted figures with permission from M. Stockman, *Nat. Mater.* **3**, 423 (2004), (b) solar cell, Reprinted figures with permission from V. E. Ferry *et al.*, *Adv. Mater*. **22**, 4794 (2010), (c) metamaterial, Reprinted figures with permission from A. Alu *et al., Opt. Exp.* **14**, 1557 (2006), and (d) biosensor, Reprinted figures with permission from S. Gao *et al.*, *Adv. Funct. Mater.* **20**, 78 (2010).

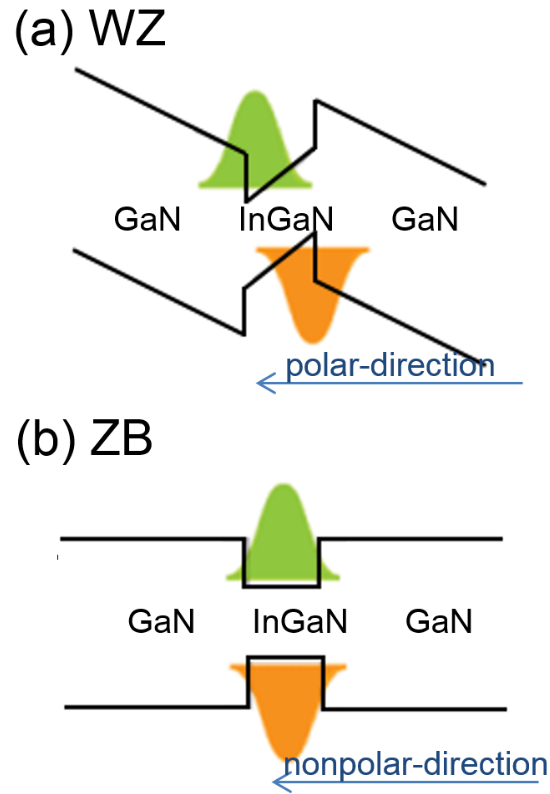


Fig. 1.6 Schematic band diagram of GaN/InGaN heterostructures. (a) WZ structures: built-in polarization field slows carrier dynamics. (b) ZB structures: built-in polarization field is screened.[105]

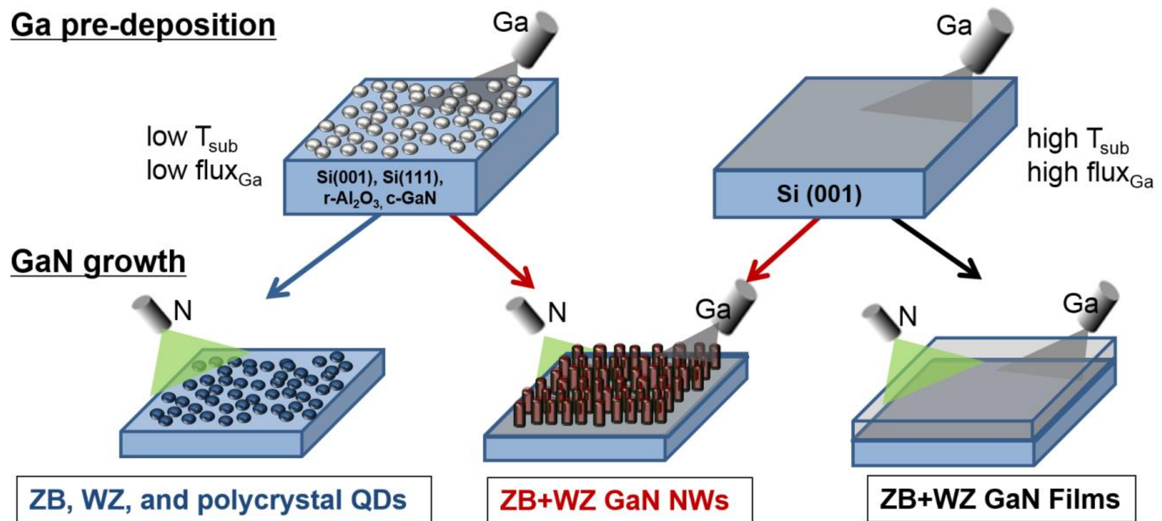


Fig. 1.7 Schematic MBE growth processes for GaN QDs, NW, and films. Using various surface treatments and Ga deposition parameters, polycrystalline, ZB, and WZ GaN QDs on Si(001), r-$Al_2O_3$, Si(111), and c-GaN substrates were fabricated via DE method. In addition, using a two-step growth method of Ga pre-deposition followed by GaN growth, ZB and WZ mixed phase of GaN NWs and films were grown.

## 1.7 References


[1] K.A. Willets, R.P. Van Duyne. Annu. Rev. Phys. Chem., 58 (2007).

[2] S. Pillai, K. R. Catchpole, T. Trupke, and M. A. Green, *J. Appl. Phys.* **101**, 093105 (2007).

[3] C. W. Cheng, E. J. Sie, B. Liu, C. H. A. Huan, T. C. Sum, H. D. Sun, and H. J. Fan, *Appl. Phys. Lett.* **96**, 071107 (2010).

[4] P. Spinelli and A. Polman, *Opt.Express* **20**, A641 (2012).

[5] C. W. Chen, C. H. Wang, C. M. Wei, and Y. F. Chen, *Appl. Phys. Lett.* **94**, 071906 (2009).

[6] K. Okamoto, I. Niki, A. Shvartser, Y. Narukawa, T. Mukai, and A. Scherer, *Nature Mater.* **3**, 601 (2004).

[7] Quality factors are defined by the resonance frequency and the broadening induced by intrinsic losses.

[8] M. Kang, T. W. Saucer, M. V. Warren, J. H. Wu, H. Sun, V. Sih, and R. S. Goldman, *Appl. Phys. Lett.* **101**, 081905 (2012).

[9] P. Wu, T. Kim, A. Brown, M. Losurdo, G. Bruno, and H. Everitt, *Appl. Phys. Lett.* **90**, 103119 (2007).

[10] M. Kang, A. A. Al-Heji, J. Lee, T. W. Saucer, J. H. Wu, L. Zhao, A. L. Katzenstein, D. L. Sofferman, V. Sih, and R. S. Goldman, *Appl. Phys. Lett.* **103**, 101903 (2013).

[11] Q. Wei, J. Lian, W. Lu, and L. Wang, *Phys. Rev. Lett.* **100**, 076103 (2008).

[12] W. Guo, M. Zhang, A. Banerjee, P. Bhattacharya, *Nano Lett.* **10**, 3355 (2010).

[13] T. N. Bhat, M. K. Rajpalke, B. Roul, M. Kumar, S. B. Krupanidhi, *J. Appl. Phys.* **110**, 093718 (2011).

[14] S. Strite, J. Ruan, Z. Li, A. Salvador, H. Chen, D.J. Smith, W.J. Choyke, and H.

Morkoc, *J. Vac. Sci. Technol. B* **9**(4), 1924 (1991).

[15] S.C. Lee, X.Y. Sun, S.D. Hersee, S.R.J. Brueck, *J. Cryst. Growth* **279**, 289 (2005).

[16] T. Huault, J. Brault, F. Natali, B. Damilano, D. Lefebvre, L. Nguyen, M. Leroux, and J. Massies, *Appl. Phys. Lett.* **92**(5), 051911 (2008).

[17] F. Widmann, J. Simon, B. Daudin, G. Feuillet, J. L. Rouviere, N. T. Pelekanos, and G. Fishman, *Phys. Rev. B* **58**(24), 15989 (1998).

[18] C. W. Hu, A. Bell, F. A. Ponce, D. J. Smith, and I. S. T. Tsong, *Appl. Phys. Lett.* **81**(17), 3236 (2002).

[19] T. Kondo, K. Saitoh, Y. Yamamoto, T. Maruyama, and S. Naritsuka, *Physica Status Solidi a Applications and Materials Science.* **203**(7), 1700–1703 (2006).

[20] M.A. Reed, R.J. Randall, R.J. Aggarwal, R.J. Matyi, T.M. Moore, A.E. Wetsel, *Phys. Rev. Lett.* **60**, 535 (1988)

[21] T. Schmidt, M. Tewordt, R.H. Blick, R.J. Haug, D. Pfannkuche, K. von Klitzing, A. Förster, H. Lüth, *Phys. Rev. B* **51**, 5570 (1995)

[22] M. Griebel, K.M. Indlekofer, A. Förster, H. Lüth, *J. Appl. Phys.* **84**, 6718 (1998)

[23] E. Calleja, M.A. Sanchez-Garcia, F.J. Sanchez, F. Calle, F.B. Naranjo, E. Munoz, U. Jahn, K. Ploog, *Phys. Rev. B* **62**, 16826 (2000)

[24] K.A. Bertness, A. Roshko, L.M. Mansfield, T.E. Harvey, N.A. Sanford, *J. Cryst. Growth* **300**, 94 (2007)

[25] R. Meijers, T. Richter, R. Calarco, T. Stoica, H.P. Bochem, M. Marso, and H. Lüth, *J. Cryst. Growth* **289**, 381 (2006).

[26] L. Cerutti, J. Ristic, S. Fernandez-Garrido, E. Calleja, A. Trampert, K.H. Ploog, S. Lazic, J.M. Calleja, *Appl. Phys. Lett.* **88**, 213114 (2006)

[27] R.S. Wagner, W.C. Ellis, *Appl. Phys. Lett.* **4**, 89 (1964)

[28] J. A. Dionne, and H. A. Atwater, *MRS Bull.* **37**, 717 (2012).

[29] O. A. Yeshchenko, I. M. Dmitruk, A. A. Alexeenko, M. Y. Losytskyy, A. V. Kotko, and A. O. Pinchuk, *Phys. Rev. B.* **79**, 235438 (2009).

[30] K. Okamoto, I. Niki, A. Shvartser, Y. Narukawa, T. Mukai, and A. Scherer, *Nature Mater.* **3**, 601 (2004).

[31] H. A. Atwater, and A. Polman, *Nature Mater.***9**, 205 (2010).

[32] A. J. Haes, S. L. Zou, G. C. Schatz, and R. P. Van Duyne, *J. Phys. Chem. B* **108**, 6961 (2004).

[33] C. M. Soukoulis, S. Linden, and M. Wegener, *Science* **315**, 47 (2007).

[34] S. Pillai, K. R. Catchpole, T. Trupke, and M. A. Green, *J. Appl. Phys.* **101**, 093105 (2007).

[35] C. W. Cheng, E. J. Sie, B. Liu, C. H. A. Huan, T. C. Sum, H. D. Sun, and H. J. Fan, *Appl. Phys. Lett.* **96**, 071107 (2010).

[36] G. Xu, M. Tazawa, P. Jin, S. Nakao, and K. Yoshimura, *Appl. Phys. Lett.* **82**, 3811 (2003).

[37] H. Mertens, J. Verhoeven, A. Polman, and F. D. Tichelaar, *Appl. Phys. Lett.* **85**, 1317 (2004).

[38] G. Sun, J. B. Khurgin, and R.A. Soref, *Appl. Phys. Lett.* **94**, 101103 (2009).

[39] P. Spinelli and A. Polman, *Opt.Express* **20**, A641 (2012).

[40] M. P. Hanson, A. C. Gossard, and E. R. Brown, *J. Appl. Phys.* **102**, 043112 (2007).

[41] Y.P. Hsieh, C.T. Liang, Y.F. Chen, C.W. Lai, and P.T. Chou, *Nanotechnology* 18, 415707 (2007).

[42] C. W. Chen, C. H. Wang, C. M. Wei, and Y. F. Chen, *Appl. Phys. Lett.* **94**, 071906 (2009).

[43] M. De Lourdes Ruiz Peralta, U. Pal, and R. Sanchez Zeferino, *ACS Appl. Mater. Interfaces* **4**, 4807 (2012)

[44] X. D. Zhou, X. H. Xiao, J. X. Xu, G. X. Cai, F. Ren, and C. Z. Jiang, *EPL*, **93**, 57009 (2011).

[45] U. Strauss, W. W. Rühle, and K. Köhler, *Appl. Phys. Lett.* **62**, 55 (1993).

[46] T. Matsusue, and H. Sakaki, *Appl. Phys. Lett.* **50** (20), 1429 (1987).

[47] U. Strauss, W. W. Ruhle, and K. Kohler, *Appl. Phys. Lett.* **62** (1), 55 (1993).

[48] H. Dai, M. Li, Y. Li, H.Yu, F. Bai, and X. Ren, *Opt. Express*, **20**, A502 (2012).

[49] M. Rycenga, C. M. Cobley, J. Zeng, W. Li, C. H. Moran, Q. Zhang, D. Qin, and Y. Xia, *Chem. Rev.* **111**(6), 3669–3712 (2011).

[50] D. Derkacs, S. H. Lim, P. Matheu, W. Mar, and E. T. Yu, *Appl. Phys. Lett.* **89**(9), 093103 (2006).

[51] P. C. Wu, M. Losurdo, T. H. Kim, M. Giangregorio, G. Bruno, H. O. Everitt, and A. S. Brown, *Langmuir* **25**, 924 (2009).

[52] P. C. Wu, T. H. Kim, A. S. Brown, M. Losurdo, G. Bruno, and H. O. Everitt, *Appl. Phys. Lett.* **90**, 103119 (2007).

[53] P. C. Wu, C. G. Khoury, T. H. Kim, Y. Yang, M. Losurdo, G. V. Bianco, T. Vo-Dinh, A. S. Brown, and H. O. Everitt. *J. Am. Chem. Soc.* **131**, 12032 (2009).

[54] P. C. Wu, M. Losurdo, T. H. Kim, S. Choi, G. Bruno, and A. S. Brown. *J. Vac. Sci. Technol. B* **25**, 1019 (2007).

[55] Y. Yang, N. Akozbek, T-H. Kim, J. M. Sanz, F. Moreno, M. Losurdo, A. S. Brown, and H. O. Everitt, *ACS Photonics* **1**, 582 (2014).

[56] N. J. Halas, S. Lal, W. Chang, S. Link, and P. Nordlander, *Chemical Reviews, vol. 111*, no. 6, pp. 3913–3961, 2011.

[57] M. P. Hanson, *J. Appl. Phys.* **102**, 043112 (2007).

[58] I. Akasaki and H. Amano, *Jpn. J. Appl. Phys.* **36**, 5393(1997).

[59] C.-Y. Yeh, Z.W. Lu, S. Froyen, A. Zunger, *Phys. Rev. B* 46, 10086 (1992).

[60] P. Das and D. K. Ferry, *Solid-State Electron.* **19**, 851 (1976).

[61] H. Yang, L.X. Zheng, J.B. Li, X.J. Wang, D.P. Xu, Y.T. Wang, X.W. Hu, and P.D. Han, *Appl. Phys. Lett.* **74**, 2498 (1999).

[62] G. Ramírez-Flores, H. Navarro-Contreras, A. Lastras-Martínez, R. C. Powell, and J. E. Greene, *Phys. Rev. B* **50**, 8433 (1994).

[63] Z. Sitar, M. J. Paisley, J. Ruan, J. W. Choyke, and R. F. Davis, *J. Mater. Sci. Lett.* **11**, 261 (1992).

[64] Z. L. Wang, *Adv. Mater.* **19**, 889 (2007).

[65] T. Schupp, T. Meisch, B. Neuschl, M. Feneberg, K. Thonke, K. Lischka, and D. J. As, *J. Cryst. Growth* **312**, 3235 (2010).

[66] D. J. As, *Microelectron. J.* **40** 204 (2009).

[67] T. Schupp, T. Meisch, B. Neuschl, M. Feneberg, K. Thonke, K. Lischka, and D. J. As, *J. Cryst. Growth* **312**, 3235 (2010).

[68] S. V. Novokiv, C. T. Foxon, and A. J. Kent, *Phys. Status Solidi C* 8, No5 1439 (2011).

[69] T. Lei *J. Appl. Phys.* **71**, 4933 (1992).

[70] H. Masui, S. Nakamura, S. P. DenBaars & K. Mishra, *IEEE Trans. Electron Devices,* **57**, 88 (2009).

[71] T.X. Wang, Y. Li, and Y.M. Liu, *Phys. Status Solidi B* **248**, 1671 (2011).

[72] C. Adelmann, E. Martinezguerrero, F. Chabuel, J. Simon, B. Bataillou, G. Mula, L. Dang, N. Pelekanos, B. Daudin, and G. Feuillet, *Mater. Sci. Eng. B* **82**, 212 (2001).

[73] G. P. Dimitrakopulos, E. Kalesaki, J. Kioseoglou, Th. Kehagias, A. Lotsari, L. Lahourcade, E. Monroy, I. Hausler, H. Kirmse, W. Neumann, G. Jurczak, T. D. Young, P. Dluzewski, P. Komninou, and T. Karakostas, *J. Appl. Phys.*, **108,** 104304 (2010).

[74] M-H. Kim, F. S. Juang, Y. G. Hong, C. W. Tu and S-J. Park, *J. Crystal Growth,* **251**, 465 (2003).

[75] M. Burger, T. Schupp, K. Lischka and D. S. As, *Phys. Status Solidi (c)*, **9**(5), 1273 (2012).

[76] K. K. Lee, W. A. Doolittle, T-H. Kim, A. S. Brown, G. S. May, S. R. Stock, Z. R. Dai & Z. L. Wang, *J. Crystal Growth*, **231**, 8 (2001).

[77] C. Santori, S. Gotzinger, Y. Yamamto, S. Kato, K. Hushino and Y. Arakawa, *Appl. Phys. Lett.*, **87**, 051916 (2005).

[78] D. J. As, *Microelectron J.*, **40**, 204 (2009).

[79] J. Simon, N. T. Pelekanos, C. Adelmann, E. Martinez-Guerrero, R. Andre, B. Daudin, Le Si Dang and H. Mariette, *Phys. Rev. B*, **68** 035312 (2003).

[80] E. Martinez-Guerrero, F. Chabuel, B. Daudin, J. L. Rouviere and H. Mariette, *Appl. Phys. Lett.*, **81**, 5117 (2002).

[81] K. Kawasaki, D. Yamazaki, A. Kinoshita, H. Hirayama, K. Tsutsui and Y. Aoyagi, *Appl. Phys. Lett.* **79**, 2243 (2001).

[82] Y. Wang, A. S. Özcan, C. Sanborn, K. F. Ludwig, A. Bhattacharyya, R. Chandrasekaran, T. D. Moustakas, L. Zhou, and D. J. Smith, *J. Appl. Phys.*, **102**, 073522 (2007).

[83] T. Maruyama, H. Otsuboa, T. Kondoa, Y. Yamamotob, and S. Naritsuka, *J. Crystal Growth*, **301**, 486 (2007).

[84] S. Naritsuka, T. Kondoa, H. Otsuboa, K. Saitoha, Y. Yamamotob, and T. Maruyama, *J. Crystal Growth*, **300,** 118 (2007).

[85] T. Kondo, K. Saitoh, Y. Yamamoto, T. Maruyama, and S. Naritsuka, *Phys. Status Solidi (a)*, **203**, 1700 (2006).

[86] T. Schupp, T. Meisch, B. Neuschl, M. Feneberg, K. Thonke, K. Lischka and D. J. As, *J. Crystal Growth*, **312**, 3235 (2010).

[87] T. Schupp, T. Meisch, B. Neuschl, M. Feneberg, K. Thonke, K. Lischka and D. J. As, *J. Crystal Growth*, **323**, 286 (2011).

[88] M. Burger, T. Schupp, K. Lischka and D. S. As, *Phys. Status Solidi (c)*, **9**(5), 1273 (2012).

[89] K. Kawasaki, D. Yamazaki, A. Kinoshita, H. Hirayama, K. Tsutsui and Y. Aoyagi, *Appl. Phys. Lett.* **79**, 2243 (2001).

[90] A. W. Wood, X. Weng, Y. Q. Wang, and R. S. Goldman, *Appl. Phys. Lett.* **99**, 093108 (2011).

[91] W. Guo, A. Banerjee, P. Bhattacharya and B. S. Ooi, *Appl. Phys. Lett.* **98**, 193102 (2011).

[92] W. Guo, M. Zhang, P. Bhattacharya, and J. Heo. *Nano lett.***11**,1434 (2011).

[93] C. Chèze, L. Geelhaar, A. Trampert and H. Riechert, *Appl. Phys. Lett.* 97, 043101 (2010).

[94] R. Calarco, R. J. Meijers, R. K. Debnath, T. Stoica, E. Sutter, and H. Lüth, *Nano lett.* **7**, 2248 (2007).

[95] Y. S. Park, C. M. Park, D. J. Fu, T. W. Kang and J. E. Oh, *Appl. Phys. Lett.* **85**, 5718 (2004).

[96] S. F. Garrido, J. Grandal, E. Calleja, M. A. Sánchez-García and D. López-Romero, *J. Appl. Phys.* **106**, 126102 (2009).

[97] C. Chèze, L. Geelhaar, O. Brandt, W. M. Weber, H. Riechert, S. Münch, R. Rothemund, S. Reitzenstein, A. Forchel, T. Kehagias, P. Komninou, G. P. Dimitrakopulos, and T. Karakostas, *Nano Research*, **3**, 528 (2010).

[98] M. Hiroki, H. Asahi, H. Tampo, K. Asami, and S. Gonda *J. Crystal Growth* **209**, 387 (2000).

[99] G. Nouet, P. Ruterana1, H. Tampo, and H. Asahi, *J. Phys.: Condensed Matter*, **14**, 12697 (2002).

[100] S.V. Novikov, C.R. Staddon, F. Luckert, P.R. Edwards, R.W. Martin, A.J. Kent, C.T. Foxon, *J. Crystal Growth* **350**, 80 (2012).

[101] S.V. Novikov, N.M. Stanton, R.P. Campion, C.T. Foxon, A.J. Kent *J. Crystal Growth* **310**, 3964 (2008).

[102] D. J. As, *Microelectron. J.* **40** 204 (2009).

[103] A. Philippe, C. Bru-Chevallier, M. Vernay, G. Guillot, J. Hübner, B. Daudin, G. Feuillet, *Mater Science and Engin. B*, **59**, 168 (1999).

[104] M. Feneberg, M. Röppischer, C. Cobet, N. Esser, J. Schörmann, T. Schupp, D. J. As, F. Hörich, J. Bläsing, A. Krost, and R. Goldhahn, *Phys. Rev. B* **85**, 155207 (2012).

[105] S-H. Park and S-L. Chuang, *Semicon. Sci. Technol.* **17**, 686 (2002).

# Chapter 2

# Experimental Procedures

## 2.1 Overview

This chapter describes the experimental procedures used for the synthesis and characterization of focused ion beam (FIB) irradiation-induced Ga droplet arrays, GaAs overgrowths of Ga droplet arrays, and GaN nanostructures. For these experiments, undoped semi-insulating GaAs (001), Si (001), and Si (111) substrates were used. All the post-irradiation overgrowths and GaN nanostructure growths were carried out in a Varian modified GEN II molecular beam epitaxy (MBE) system. Following irradiations or MBE growths, surface morphologies were examined using scanning electron microscopy (SEM) and atomic force microscopy (AFM). The structures of GaAs:Ga nanocomposites and GaN nanostructures were examined using X-ray diffraction (XRD). To examine the optical emission efficiency of GaAs:Ga nanocomposites and GaN nanostructures, photoluminescence (PL) spectra were collected. All procedures were carried out by the author except where noted.

## 2.2 Focused Ion Beam Irradiation

All FIB irradiation described in this thesis was carried out in a FEI NOVA 200 dual beam workstation shown schematically in Fig. 2.1. The FIB system consists of an ion beam column, an electron beam column, an energy dispersive x-ray, and secondary electron detectors, in a high vacuum chamber with $10^{-5}$ Torr base pressure. This system combines a high-resolution secondary electron microscope for surface imaging, a Ga+ FIB for irradiation and patterning, and X-ray microanalysis for characterization. During FIB irradiation, surface imaging is achieved via the collection of secondary electrons.

All samples were irradiated at room temperature. The FIB voltage, current, pitch size, dwell time, dose rate, and ion fluence, magnification, and irradiation time are 5 KeV, 0.23 nA, 6.1 nm pitch, 50 ns, $5.1\times10^{3}$ dose/sec, $5\times10^{18}$ ions/cm$^{2}$, $\times$20K, and 300s, respectively. FIB irradiation was carried out at two angles of ion-beam incidence ($\theta_i$), as shown in the schematics of the orientation of electron beams (dashed line) and ion beams (dotted line) with respect to the sample surface, shown in Figs. 2.1 (b).

## 2.3 Molecular Beam Epitaxy

The GaAs:Ga nanocomposite and GaN nanostructure samples discussed in this thesis were grown in a Modified Varian Gen II MBE system. Molecular beam epitaxy (MBE) is a vacuum evaporation technique for epitaxial growth of high quality films one atomic layer at a time.[1,2] The process is performed in an ultra-high vacuum chamber, where an epitaxial film is formed via chemical interaction of molecular beams on a heated crystalline substrate surface.[3] The molecular beams are produced by sublimation or

evaporation of heated solids or liquids, and the incoming molecules are so reactive that epitaxial growth can occur at conditions far from equilibrium.

The Modified Varian Gen II MBE system, as illustrated in Figure 2.2, consists of separately pumped load-lock, buffer, and growth chambers connected by magnetic transfer rods and trolleys. The growth chamber source flange houses seven solid sources (Ga, In, Al, Si, Be, Bi, and As cracker) and N plasma source, and the source materials are contained in pyrolytic boron nitride (PBN) crucibles located in Knudsen effusion cells. The molecular beam flux is exponentially dependent on the temperature of the effusion cell controlled by heating the filaments surrounding the PBN crucible. The effusion cell temperature is monitored by a thermocouple in contact with the crucible, and the beam flux is measured by an ionization gauge sitting at the growth position. The exposure of each molecular beam is controlled by computer controlled pneumatic shutters. The flux of the rf $N_2$ plasma source is controlled by a mass flow controller (MFC).

To reproducibly control the N flux during GaN nanostructure growths, we struck the plasma and then monitored the partial pressure of 14 amu (active N) in the chamber with a residual gas analyzer (RGA). The MFC was then adjusted before the growth of each sample so that the N flux was constant for each growth. Since our GaN growths consist of separate Ga droplet formation and droplet nitridation steps for GaN QDs and GaN epitaxial growth of GaN films and NWs, to prevent N plasma from incorporating with the Ga droplets during the Ga droplet formation step, our plasma source was gate valve controlled. The plasma source was mounted behind a pneumatic gate valve and separately pumped by a turbo pump so that the plasma may be struck with the gate valve closed.

Samples are held in the growth chamber at either growth or transfer position by a manipulator referred to as the CAR (Continuous Azimuthal Rotation). During epitaxial growth, the CAR is typically rotated at 10 rpm to ensure the film uniformity. In addition, the growth chamber contains facilities for *in situ* reflection high-energy electron diffraction (RHEED), which will be described in Section 2.4. The growth chamber is pumped by a CTI Cryo-Torr 8 cryopump and a Varian sputter-ion pump, and the growth chamber pressure is monitored by an ionization gauge located on the chamber wall. During growth, the growth chamber is cooled down with liquid nitrogen ($LN_2$), which helps achieve a base pressure of $< 3\times10^{-10}$ Torr.

All substrates were mounted on In (for GaAs overgrowths) or In-free (for GaN nanostructure growths) blocks, baked in the load-lock chamber for 8 hours at 150 ºC, and then outgassed in the buffer chamber for at least 30 minutes at 180 ºC. Subsequently, the substrate was transferred into the growth chamber with the transfer rod.

For GaAs overgrowths, all films were grown on "epi-ready" GaAs substrates which had been irradiated with FIB to produce surface Ga droplet arrays. All samples were In-mounted molybdenum blocks ($T > 150°C$), and pre-baked at 150°C for 8 hours in the load-lock. In the growth chamber, the substrate temperature was continuously raised to the growth temperature without As overpressure. Substrate temperatures ($T_{sub}$) were determined using a spring-loaded thermocouple in direct contact with the backside of the molybdenum block, and calibrated based on the difference between the $T_{CAR}$ and $T_{sub}$.

For GaN growths, all nanostructures were grown on Si (001) or Si (111) substrates which had been chemically etched with a 5 % dilute HF solution, consisting of 2mL of 49 % HF and 18mL of DI water. All samples were grown on In-free blocks and pre-baked at

150°C for 8 hours in the load-lock. Prior to growth, the temperature of each sample was calibrated using the oxide desorption temperature. The oxide desorption temperature was defined as the temperature at which the RHEED pattern transformed from a diffuse 1×1 to a streaky 2×1 (7×7) pattern for Si (001) (Si (111)) surfaces. The substrate temperature ($T_s$) was increased to the point where a streaky 2×1 or 7×7 RHEED pattern is observed, considered to be the surface oxide desorption temperature 880 ℃. Once we found the thermocouple temperature corresponding to $T_s$=880℃, the substrate temperature was raised by an additional 20 °C for 10 minutes to ensure complete desorption of surface oxide. Some of the Si (001) samples were not heated up to $T_s$=900 °C, leaving a native oxide layer on the surfaces.

### 2.4 Reflection High-Energy Electron Diffraction

The surface reconstructions were monitored *in situ* with a STAIB RH 30 RHEED source, operating at 18 keV. The electron beam from the RHEED gun is accelerated and directed onto the sample surface at a grazing angle of ~1°. The electrons that are diffracted by the sample surface then impinge on a phosphor screen on the other side of the growth chamber, as shown in Figure 2.2. A charge coupled device (CCD) camera is used to collect the luminescence from the phosphor screen. RHEED patterns were used to monitor the surface reconstruction during the GaAs overgrowth and GaN nanostructure growth. For a smooth single crystal surface, electrons are reflected from the surface, penetrating the very top atomic layers. The reciprocal space is therefore composed of a set of one-dimensional streaks along the surface normal.[4] For a surface containing crystal islands, the corresponding diffraction pattern would consist of spots. For a polycrystalline structure,

which is composed of many different crystallites with different orientations, the corresponding diffraction pattern consists of concentric rings.[5]

## 2.5 Atomic Force Microscopy

The surface morphology of the Ga NP arrays on GaAs, GaAs:Ga nanocomposites, and GaN QDs was investigated using tapping mode atomic force microscopy (AFM) with Bruker Dimension Icon AFM in the Electron Microbeam Analysis Laboratory (EMAL) at the University of Michigan. We used etched silicon Nanoscience AFM probes with tip radius < 10 nm, length = 125 μm, resonance frequency = 300 kHz, and spring constant = 40 N/m for imaging. The AFM scanning head consists of a piezoelectric tube scanner with the x-, y-, and z- electrodes oriented. The z-motion is achieved by expanding or contracting the piezoelectric tube with an applied voltage to the z-electrode. Similarly, the x- and y-motion of the AFM tip is achieved by applying a voltage to the x- and y- electrodes to enable the bending of the piezoelectric tube in the x- and y- directions, respectively. Figure 2.3 shows a schematic of (a) straight and (b) bended piezoelectric tube during AFM tip scanning on a flat surface. The bending of the piezoelectric tube results in an offset of the laser reflection on the photodiode. The offset of the laser reflection usually leads to a curvature distortion in the output morphology (a.k.a. "bowing") from the scanning surface, which is more significant for larger area scanning.[6] To correct the bowing in the AFM images, all as-collected AFM images were flattened by subtracting a quadratic background in the lateral directions using Scanning Probe Image Processor (SPIP).

## 2.6 Scanning Electron Microscopy

FEI Nova 200 Nanolab dual-beam scanning electron microscopy (SEM) system was used to image GaAs:Ga nanocomposites and GaN nanostructures. Both plan-view and side-view SEM were used to image the surfaces and cross-sections. Typical SEM imaging conditions involved 10 keV electrons with a beam current of 98 pA. The working distance from the electron beam column to sample surfaces was maintained to be 5 mm.

## 2.7 X-Ray Diffraction

The crystallinity of GaAs:Ga nanocomposites and GaN nanostructures was determined using x-ray diffraction (XRD), conducted with a 12 kW Rigaku rotating anode source (Cu k$\alpha$ target $\lambda = 0.1542$ nm and graphite monochromator). Prior to the XRD scans of GaAs:Ga nanocomposites and GaN nanostructure samples, a Si (001) sample was measured to ensure that the equipment was aligned. For $\theta/2\theta$ scans, a sample is rotated by an angle $\theta$, while the detector is rotated by an angle $2\theta$. The X-ray source was operated at 40 kV and 100 mA. In addition, grazing incidence X-ray diffraction (GIXRD) analysis was also used. In this measurement mode, the angle between the source and sample surface was kept fixed at an incident angle ($\theta_i$) ranging from 1 to 8°. For GIXRD analysis, X-ray source was operating at 30 kV and 10 mA to avoid damage on the detector. For both $\theta/2\theta$ scans and GIXRD scans, the measurements were performed with a scan step of 0.01 degree, and scan rate of 1 deg/min. To identify the diffraction peaks from GaAs:Ga nanocomposites and GaN nanostructures, pattern indexing was performed with JADE software (Materials

Data, Inc.), using the Powder Diffraction File (PDF), which is a database of X-ray powder diffraction patterns maintained by the International Center for Diffraction Data (ICDD).[7]

### 2.8 Photoluminescence

Spatially-resolved PL measurements were performed on the samples mounted in a helium flow cryostat operating at 10K, using a 633 nm CW Helium-Neon laser. Pump powers varied from 0.34 mW, as measured before a 0.7 NA infinity corrected objective. The diameter of the normally-incident focused laser on the sample was 5 μm, and a confocal microscope configuration was used to collect the emission from a 3 μm diameter spot within only the FIB patterned regions. PL was recorded using a 150 G/mm reflection grating in a 0.75 m spectrometer and a liquid nitrogen cooled Si CCD detector. To take into account the Ga NP size dependence of the pump laser absorption and DAP emission, for each sample, the PL spectrum was normalized by the integrated intensity of the absorbed laser light, defined as the difference between the laser spectrum and laser-induced surface reflectivity. PL enhancement ratios were then defined as the ratio of the normalized PL intensities for regions of the GaAs layer with and without Ga NPs. The PL measurements for the GaAs:Ga nanocomposites were performed by Dr. Jieun Lee in Prof. Sih's research group. The PL measurements for the GaN nanostructures were performed by Tyler Hill and Adam Katcher in Prof. Deng's research group.

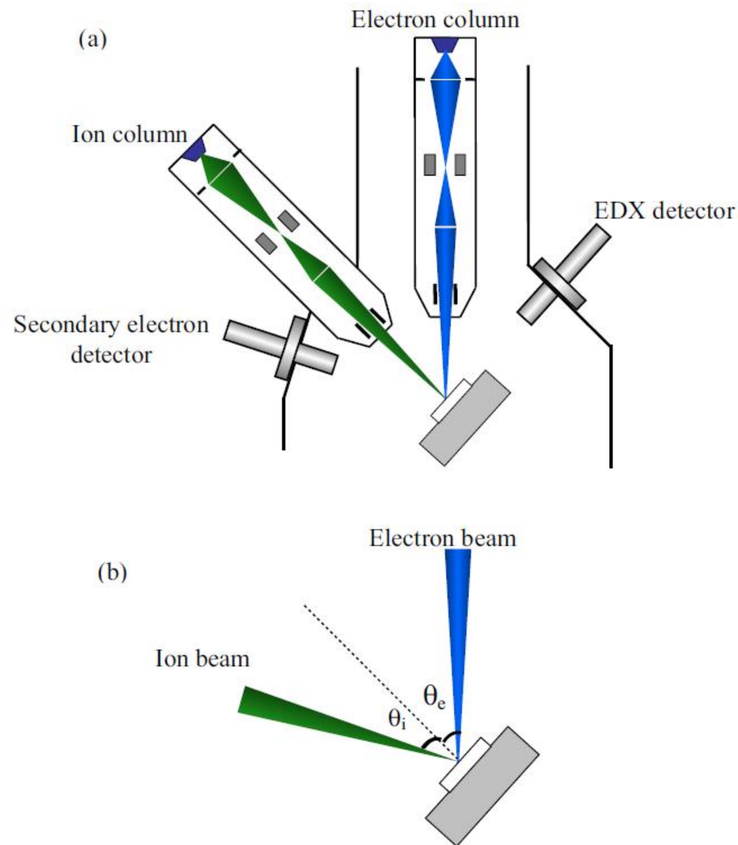


Fig. 2.1 (a) Schematic of NOVA 200 dual beam workstation, and (b) schematic of relative orientations of the electron beam, the ion beam, and the sample surface normal (dashed line). The electron beam angle of incidence, $\theta_e$ is defined as the angle between the incident electron beam and the sample surface normal. The ion beam angle of incidence, $\theta_I$, is defined as the angle between the incident ion beam and the sample surface normal. The angle between the ion and electron beam column is fixed at 52°. Therefore, to achieve normal-incidence FIB irradiation, $\theta_I$=0°, the sample must be tilted to 52° with respect to the electron beam. The angle between the electron beam column and secondary electron detector is 90°. Reprinted figure with permission from Myungkoo Kang Ph.D. thesis, University of Michigan, Ch.2, 2014.

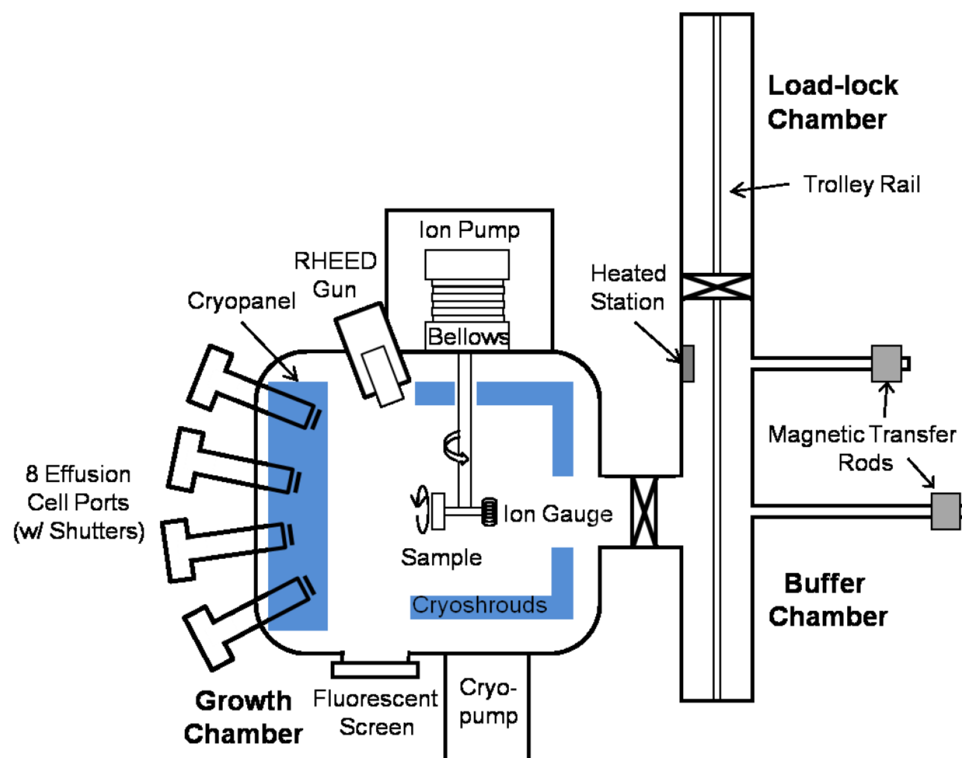


Fig. 2.2 Schematic (top-down view) of the Modified Varian Gen II molecular beam epitaxy system used in this thesis study. Ga, Al, In, Si, Be, Bi and As solid sources, and rf $N_2$ plasma source are located in the effusion cell ports. Reprinted figure with permission from Simon Huang Ph.D. thesis, University of Michigan, Ch.2, 2015.

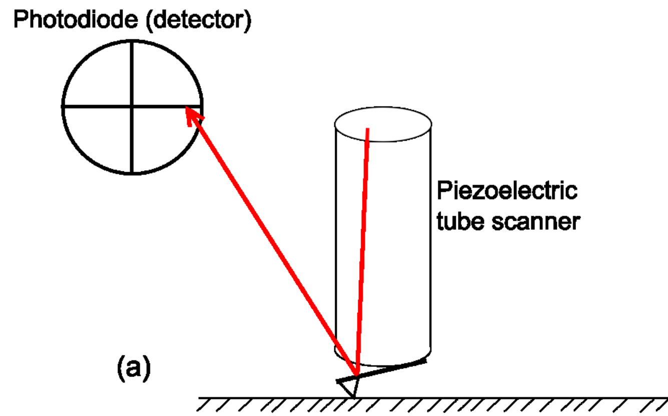


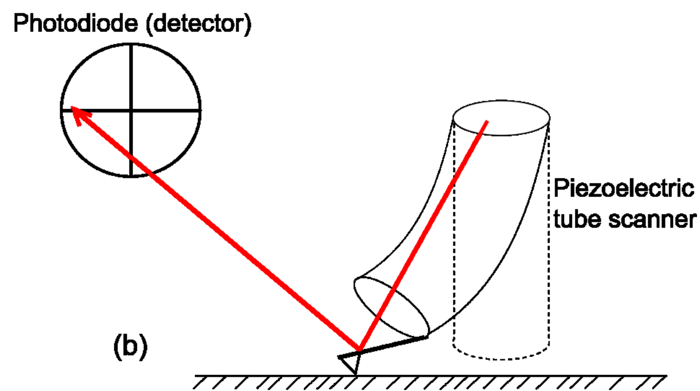


Fig. 2.3 Schematic of (a) straight and (b) bended piezoelectric tube during AFM tip scanning on a flat surface. The laser reflection from the tip to the photodiode is indicated by the red line with an arrow. Reprinted figure with permission from Simon Huang Ph.D. thesis, University of Michigan, Ch.2, 2015.

**2.9 References**

[1] A.Y. Cho and J.R. Arthur, *Progr. Solid State Ch.* **10**, 157 (1975).

[2] A.Y. Cho, *J. Crys. Growth* **202**, 1 (1999).

[3] C.T. Foxon, and B.A. Joyce, *Growth and Characterisation of Semiconductors* (Adam Hilger, 1991) pp. 35.

[4] W. Braun, *Applied RHEED* (New York: Springer) (1999).

[5] F. Tang, T. Parker, G-C. Wang and T-M. Lu, *J. Phys. D: Appl. Phys.,* **40** R427 (2007).

[6] R. Howland and L. Benatar, *A Practical Guide: To Scanning Probe Microscopy*. (Park scientific instruments, 1996).

[7] The International Centre for Diffraction Data, www.icdd.com

# Chapter 3

# Formation of embedded Ga nanoparticle (NP) arrays and their influence on GaAs photoluminescence

## 3.1 Overview

This chapter describes our investigations of the formation of embedded Ga nanoparticle (NP) arrays and their influence on GaAs photoluminescence (PL) efficiency. Close-packed arrays of Ga NPs embedded in GaAs are fabricated using off-normal focused-ion-beam irradiation, followed by molecular-beam-epitaxy. Using a combination of PL spectroscopy and electromagnetic computations, we identify a regime of NP size and depth where NP-induced electron-hole pair (EHP) generation is increased, leading to enhanced GaAs near-band-edge (NBE) PL efficiency. As the NP depth and size are increased, the reduced spontaneous emission rate becomes overwhelmed by the NP-induced EHP generation enhancement, leading to reduced NBE PL efficiency. We successfully fabricate the embedded GaAs:Ga nanocomposites and demonstrate PL enhancement induced by Ga NP arrays. Furthermore, we discuss new insights into PL enhancement mechanisms. This approach provides an opportunity to enhance the PL efficiency from a variety of semiconductor heterostructures, using a seamless approach to embed non-noble metals during epitaxy.

### 3.2 Background: Ga Metallic Nanoparticle Surface Plasmon Resonances

When electromagnetic (EM) radiation is incident upon metallic nanoparticles (NPs), collective oscillations, termed localized surface plasmon resonances (LSPR), are generated.[1] Recently, noble metal NP-semiconductor interfaces have shown significant promise for light absorption and emission applications.[2,3,4,5,6,7,8,9,10] Metallic NPs in semiconductors generate LSPR depending on particle size, shape, the refractive index of NPs and semiconductors, and the separation distance between the NPs and semiconductors,[1,4,7,11] leading to enhanced light absorption[12] and emission.[3,8] The NP-induced localized field enhances light absorption in the semiconductor at energies close to the LSPR energy ($E_{LSPR}$), resulting in enhanced electron-hole pair (EHP) generation.[12,13] In the light emission process, when $E_{LSPR}$ is comparable to the emission energy of the semiconductor, the spontaneous emission (SE) rate in the semiconductor is enhanced. Depending on the geometry of the semiconductor and metal, such as the separation distance between the semiconductor and metal, this SE rete enhancement in turn leads to the enhancement of radiative recombination.[8,11] In addition, if $E_{LSPR}$ is greater than the emission energy of the semiconductor, the NPs act as a source to excite EHP in the semiconductor by a resonant energy transfer (RET) process, consequently resulting in enhanced emission.[14,15] On the other hand, NP-induced emission reduction has been observed depending on the band structures of the NPs and semiconductor due to a direct electron transfer (DET) from the semiconductor to the NPs when they are directly in contact.[16,17] When the semiconductor has larger work function than the metal NPs, its Fermi energy level lies lower than the Fermi energy level of the NPs, resulting in the

electron transfer from the semiconductor to the metal NP. To date, materials research and device fabrication have focused nearly exclusively on Ag and Au NP dispersions in two dimensions,[7,8,12,15] with plasmon resonances limited to visible wavelengths.[3]

Recent, Ga NPs, with LSPR quality factors comparable to those of Ag and Au, [18,19] and plasmon energies tunable from the infrared to the ultraviolet wavelength ranges, have been reported.[18,20,21] Furthermore, close-packed surface arrays of Ga NPs were recently demonstrated using ion-irradiation of semiconductor surfaces.[18,22] Although the influence of three-dimensional NP arrays on infrared absorption in semiconductors has been reported,[13] their influence on infrared emission has yet to be considered. In addition, the complete analysis on the PL enhancement mechanisms of any semiconductor-metal nanocomposites, considering absorption, emission, RET process and DET process, has not been demonstrated. Here, we use a combination of experiments and computations to determine the influence of the Ga NP diameter ($d_{Ga}$) and NP depth (i. e. overgrown layer thickness) on the enhancement and reduction of GaAs near-band-edge (NBE) emission, revealing a physical mechanism based upon NP-induced 1) absorption enhancement, 2) EHP generation by LSP-excitation, and 3) SE rate reduction induced by Ga NPs, as shown in Fig. 3.1.

### 3.3 Fabrication of embedded GaAs:Ga Nanocomposites

Figure 3.2 presents a schematic diagram depicting the fabrication process of embedded GaAs:Ga nanocomposites, which consists of FIB-irradiation and MBE overgrowth. For these studies, 2D close-packed Ga NP arrays were prepared on semi-

insulating GaAs (001) surfaces using an FEI Nova 200 Nanolab dual beam FIB system with 5 keV voltage, 0.23 nA current, 6.1 nm pitch, and 50 ns dwell time.[20] Several 20 μm × 20 μm regions were raster scanned with off-normal incidence Ga+ irradiation ($\theta_{ion}$ = 52° and 30°), as shown in Fig. 3.2 (a).[19] Within 30 minutes of removal from the FIB chamber, the NP array samples were introduced into the load-lock of a GEN II MBE chamber. Following a load-lock bakeout at 150 °C for 8 hours, the NP array samples were transferred to the MBE chamber for overgrowth. The NP array samples were then heated to 300 °C for 10 minutes under $As_2$ flux of $5.4 \times 10^{-6}$ Torr, at which point a diffuse (1 × 1) RHEED pattern was observed. Subsequently, 20 to 500 nm thick GaAs layers were grown at 300 °C, using a growth rate of 1 μm/hr and a V/III beam-equivalent pressure ratio of 12. As shown in Fig. 3.2 (b), at the end of each overgrowth, a RHEED pattern consisting of concentric rings revealed the presence of polycrystalline GaAs. Figure 3.3 shows the cross-sectional transmission electron microscopy images of the embedded GaAs:Ga nanocomposite with NP depth of 500nm. The GaAs overgrown layer exhibits polycrystalline structure. Following overgrowth, the surface morphology was examined using tapping-mode atomic force microscopy (AFM) with Si probes. Spatially-resolved PL measurements were performed on samples mounted in a liquid-He flow cryostat operating at 10 K, using a HeNe laser with 633 nm excitation wavelength, incident laser power of 0.38 mW, and a 5 μm-diameter beam spot.

### 3.4 Morphology of GaAs:Ga Nanocomposites

Figure 3.4 presents AFM images of unpatterned regions (left), FIB-patterned regions at $\theta_{ion} = 52°$ (middle), and FIB-patterned regions at $\theta_{ion} = 30°$ (right) for NP depth of (a) 0nm (i.e. as-FIB NP), (b) 20nm, (c) 50nm, (d) 100nm, (e) 200nm, and (d) 500nm, with corresponding fast Fourier transforms (FFTs) as insets. For the $\theta_{ion}$ = 52° (30°) patterned regions shown in the middle of Fig. 3.4 (a) (in the right of Fig. 3.3 (a)), close-packed arrays with $\langle d_{Ga} \rangle = 40 \pm 6$ nm ($66 \pm 18$ nm), height $\langle h_{Ga} \rangle = 8 \pm 0.6$ nm (10 $\pm$ 3.3 nm) and inter-droplet spacing $\langle d_{Ga\text{-}Ga} \rangle = 72 \pm 9$ nm ($108 \pm 12$ nm), are observed. Following overgrowth of the unpatterned regions, as shown in the left sides of Fig. 3.4 (b) - (f), circular FFT patterns are observed, indicating an isotropic distribution of surface features. For the arrays of $d_{Ga}$=40nm NPs, the FFT shown in the middle of Fig. 3.4 (a) exhibits a hexagonal spot pattern with a split center spot, suggesting the presence of a six-fold symmetry with a superimposed two-fold symmetry, consistent with the AFM image of elongated hexagonal arrays of NPs. The raster scanning of the ion beam induces Ga mass transport, eventually leading to the elongation of close-packed Ga NP arrays along the scan direction.[23] Following overgrowth of the NP arrays to achieve NP depths of 50nm and 100 nm, similar elongated hexagonal arrays of NPs are observed, as shown in the middle of Fig. 3.4 (b)-(d). Finally, for NP depth of 200 nm and 500 nm, shown in the middle of Fig. 3.4 (e)-(f), an isotropic distribution of surface features is observed. However, as shown in the right of Fig. 3.4 (a)-(f), for all the arrays of $d_{Ga}$=66nm NPs with NP depths of 0 – 500nm, circular FFT patterns are observed, indicating an isotropic distribution of surface features.

### 3.5 Influence of Ga NP size and Depth on GaAs Photoluminescence

As illustrated in the top of Fig. 3.4, spatially-resolved PL measurements were performed on the unpatterned regions (top-left of Fig. 3.4) and patterned regions with $\theta_{ion}$ = 52° (top-middle of Fig. 3.4) and 30° (top-right of Fig. 3.4). Figure 3.5 shows the NP depth (overgrown layer thickness) dependence of the GaAs PL intensities for patterned regions with $d_{Ga}$=40nm and 66nm (green and blue line), in comparison with that from the unpatterned regions (black dashed line). Within the range 1.475 to 1.525 eV, the polycrystalline GaAs NBE emission, including the band-to-band (BtB) emission at 1.515 eV and the donor-acceptor pair (DAP) emission at 1.491 eV, are apparent.[24,25] Since the 633 nm laser penetration depth in GaAs is ~280nm, which is significantly lower than the GaAs wafer thickness (~600μm), transmission through both the FIB patterned and unpatterned regions is expected to be negligible. To take into account the influence of the surface morphology on the incident laser absorption and NBE emission, for each sample, the PL spectra were normalized by the integrated intensity of the absorbed laser light, defined as the difference between the laser spectra and the surface-induced laser reflection.[26] To consider the total reflected light at the GaAs surface, we estimate the light scattered out at the polycrystalline GaAs/air interface (i.e. diffuse reflection), assuming perfect transmission at the polycrystalline GaAs/single crystalline GaAs interface. Since the GaAs surfaces are not flat, as shown in the AFM images of Fig. 3.4, we calculate the fraction of the light scattered by surface roughness (diffuse reflection) to the total reflected light consisting of the scattered light (diffuse reflection) and the reflected light (specular reflection), defined as the total integrated scatter (TIS) equation,

$$TIS = \frac{\text{diffuse reflection}}{\text{specular reflection} + \text{diffuse reflection}} = [1 - \exp(-(\frac{4\pi \cos\theta\sigma}{\lambda})^2)]$$

, using the RMS roughness values (σ) obtained from the AFM images and the normal incident (θ=90°) light wavelength (λ) of 633nm. In Fig. 3.6, RMS roughness (left) and TIS (right) for unpatterned regions (i.e. "w/o NP"), patterned regions irradiated at $\theta_{ion}$ = 52° (i.e. "$d_{Ga}$=40nm"), and patterned regions irradiated at $\theta_{ion}$ = 30° (i.e. "$d_{Ga}$=66nm") are plotted as a function of NP depths. For each patterned and unpatterned region, we then estimate the total integrated reflected light at the GaAs surface, with the calculated TIS values and the measured reflection spectra.

For all NP depths, the intensities of the DAP emissions are higher than those of the BtB emissions, both decreasing with increasing NP depth. For $d_{Ga}$=40nm (66nm), the DAP and BtB emissions are enhanced (reduced) in the presence of Ga NPs whose depths are ≤100nm, as shown in Figs. 3.5 (a) and (b). For NP depth of 200nm, the emission intensity is reduced for the patterned region, in comparison to the unpatterned region, as shown in Fig. 3.5 (c). Finally, as shown in Fig. 3.5 (d), for NP depth=500nm, the PL spectra from the patterned and unpatterned regions are similar, suggesting a negligible influence of NP arrays on PL emission. To quantify the Ga NP-induced emission enhancement and reduction, we compare the NP depth-dependence of the PL enhancement ratio, estimated as the ratio of the integrated PL intensities for patterned and unpatterned regions, as shown in Fig. 3.5 (e). For $d_{Ga}$=40nm with the NP depths up to 100 nm, the PL enhancement ratio is 1.42, independent of NP depth. However, for NP depths exceeding 100 nm, the enhancement ratio is below or similar to 1.0. In addition, for $d_{Ga}$=66nm, all the enhancement ratios are below or similar to 1.0, revealing PL reduction in the presence of Ga NP arrays.

### 3.6 FDTD Simulations

#### 3.6.1 Overview

To gain physical insight into the influence of the Ga NP diameter and depth on the GaAs NBE emission, we compute the absorptance and SE rate ratios of nanocomposites, in comparison to that of pristine GaAs. Figure 3.7 shows the PL enhancement mechanisms that will be considered in this chapter, which are absorption enhancement, LSP-excitation via RET process, and SE rate enhancement. We use finite-difference time-domain (FDTD) simulations to calculate the absorbed optical power of the nanocomposites.[12] As shown in Fig. 3.8, in our simulations, a broad-band (1 to 10 eV) plane wave is incident on a simulation volume of a 25nm-thick vacuum layer and a GaAs:Ga nanocomposite, consisting of a plane of hemispheroidal Ga NP arrays, with $d_{Ga}$ (inter-droplet spacing, $d_{Ga\text{-}Ga}$) of 40nm (72nm) and 66nm (108nm), is buried in GaAs at depths of 0, 20, 50, 100, 200, and 500nm below the surface. Since the vacuum layer is on the top of the nanocomposite, the simulation admits the reflectance of an incident radiation at the surface of GaAs. Using low temperature frequency-dependent complex permittivities of Ga[27] and GaAs[28,29] from the literature, we compute the total absorbed (injected) optical power by integrating the absorbed (injected) optical power per unit volume[30] over the entire simulated space, a 1μm×1μm×1μm volume, with a 1 $nm^3$ mesh size and perfectly matched layer boundary conditions, which allow attenuation without reflection at the boundary of the simulated space. First, absorption per unit volume is calculated according to Eq. 3.1.

$$\text{Absorption}\ \left(\frac{\mathrm{W}}{\mathrm{m}^3}\right):\ P_{abs}(\omega) = \frac{1}{2}\omega \mathrm{Im}\big(n(x,y,z,\omega)\big)E(x,y,z,\omega)^2 \qquad (3.1)$$

Total absorbed power is then calculated by integrating $P_{abs}$ within the simulation volume according to Eq. 3.2.

$$\text{Total absorbed power (W)}: \int P_{abs}(\omega)dV = \frac{1}{2}\omega \int \mathrm{Im}\big(n(x,y,z,\omega)\big)E(x,y,z,\omega)^2\, dV \qquad (3.2)$$

Finally, the absorptance is defined as the ratio of the total absorbed optical power to the total injected power as shown in Eq. 3.3.

$$\text{Absorptance: } \alpha_{NC} = \frac{\int P_{abs\ NC}(\omega)dV}{\int P_{incidence}(\omega)dV},\ \alpha_{GaAs} = \frac{\int P_{abs\ GaAs}(\omega)dV}{\int P_{incidence}(\omega)dV} \qquad (3.3)$$

To validate these simulations, we calculate and compare the reflectance of bulk GaAs to experimental data.[22,31] The simulated absorptance of bulk GaAs (at 300K) exhibits the absorption at 1.42eV presumably corresponding to the GaAs bandedge. To determine the reflectance of bulk GaAs, we assume negligible transmittance, such that *Absorptance* (E)=1-*Reflectance* (E). The resulting energy-dependent reflectance spectrum of bulk GaAs at 300K is similar to the measured reflectance reported by H. Ehrenreich et al.,[33] for which enhancements in reflectance are apparent at 3 and 5 eV.

### 3.6.2 Absorption Enhancement

Figure 3.9 presents the simulated absorptance of the Ga NP arrays (blue line), the GaAs matrix with hole arrays in the positions of Ga NP arrays (red dotted line), and the GaAs:Ga nanocomposite (black dashed line) for $d_{Ga}$=40nm and 66nm with NP depths of 20nm, 50nm, 100nm, 200nm, and 500nm. For photon energies exceeding 3eV, the energy-

dependent absorptance for all nanocomposites and GaAs matrices are identical, presumably due to the absence of absorption into Ga NPs. It is apparent that the absorptance of the Ga NP arrays (blue line) shows maxima between 1 and 3eV, coinciding with the reported LSPR of Ga NPs on GaN (1.5 – 2.4eV)[16,17] and on GaAs (1.4 – 2.0eV).[18] Thus, the absorptance of the nanocomposites (black dashed line) is also enhanced with respect to that of GaAs in the energy range of 1 to 3eV. Due to the attenuation of incident radiation, for depths ≥ 200nm, similar absorptance spectra are observed for the buried NPs, shown in Figs. 3.9 (d)-(e) and (i)-(j).

To determine the NP size and depth dependence of absorption enhancement, we compare the absorptance of the nanocomposites to that of GaAs matrix with hole arrays (i.e. GaAs matrix) in the positions of Ga NP arrays, as shown in Fig. 3.10 (a). Since our PL measurements are performed using 633nm HeNe laser, we define the ratio of absorptance of nanocomposite to that of GaAs matrix at the photon energy of 1.956eV as the absorption enhancement ratio: $\text{Absorption enhancement ratio} = \left(\frac{\alpha_{NC}}{\alpha_{GaAs}}\right)$ , where $\alpha_{NC}$ ($\alpha_{GaAs}$) is absorptance of nanocomposite (GaAs matrix). In addition, to consider the influence of LSPR of Ga NPs on the GaAs EHP generation, we quantify $E_{LSPR}$ of each NP size and NP depth at 10K. As shown in Fig. 3.10 (b), the energy dependence of NP absorptance exhibits a Lorentzian profile, with maxima that are redshifted with increasing NP size from 40nm to 66nm.[7,8] For each NP size and NP depth, we use the maximum likelihood estimation method to locate the maximum energy values,[32] and attribute them to the $E_{LSPR}$.

Figure 3.11 (a) shows the NP depth dependence of the absorption enhancement ratio for $d_{Ga}$=40 and 66nm for NP depths ranging from 20 to 500 nm. The enhancement in

absorption is decreasing with increasing NP diameter and depth, due to reduction in E-field enhancement induced by NP arrays. For NP depths below 100nm of $d_{Ga}$ = 40nm (66nm), the predicted absorption enhancement ratio is 1.2 – 1.34 (1.04 – 1.17), resulting in the EHP generation enhancement. However, for NP depths exceeding 200nm, the absorption enhancement ratio decreases to near 1.0, suggesting negligible NP-induced enhancement of EHP generation. The highest absorption enhancement ratio is predicted for $d_{Ga}$ = 40nm at a depth < 100nm.

### 3.6.3 EHP Generation via LSP-Excitation

To quantify the EHP generation enhancement induced by resonant energy transfer (RET), we calculate the ratio of the probability of exciting EHP in semiconductor by RET process to that by incident radiation of 1.965eV, $\Omega_{RET}$ / $\Omega_{SEMI}$,[33] which is lineally proportional to the ratio of $E_{LSPR}$ to $E_{g(GaAs)}$ according to Eq. 3.4.

$$\frac{\text{Probability of exciting EHP by RET}}{\text{Probability of exciting EHP by incident field}} = \frac{\Omega_{\mathrm{NP}}}{\Omega_{\mathrm{GaAs}}} = \frac{20\pi k h\nu^2}{n^5}\left(\frac{E_{LSPR}}{E_{incident}}\right)2\left(\frac{\int (h\nu - E_g)^{1/2}\frac{d\nu}{\nu^2}}{(h\nu - E_g)^{1/2}}\right) \tag{3.4}$$

The calculated $\Omega_{RET}$ / $\Omega_{SEMI}$ value ranges 0.25 – 0.06, decreasing with increasing NP depth. The plot of total probability of exciting EHP by RET process and incident radiation vs. NP depth is shown in Fig. 3.11 (b). The highest values ranging 1.15 – 1.25 are predicted for $d_{Ga}$ = 40nm at a depth < 100nm. Since the energy dependent absorptance of Ga NP arrays exhibit Lorentzian profiles, the $\Omega_{RET}$ / $\Omega_{SEMI}$ values are significant in spite of the smaller

$E_{LSPR}$ than $E_{g(GaAs)}$ for $d_{Ga}$=40nm(66nm) with NP depth exceeding 200nm(100nm), suggesting that the enhancement of EHP generation occurs for all NP sizes and depths. For NP depths below 100nm, the maxima in the absorptance spectra of Ga NP arrays suggest the presence of LSPR at 1.69 – 2.09 eV for $d_{Ga}$=40nm and 1.47 – 1.59 eV for $d_{Ga}$=66nm. For $d_{Ga}$ = 40 nm with NP depths up to 100nm and $d_{Ga}$ = 66nm with NP depths up to 50nm, $E_{LSPR}$ is greater than $E_{g\ (GaAs)}$, suggesting that the resonant energy transfer from the Ga NP to GaAs is expected to increase EHP generation, likely contributing to enhanced GaAs NBE emission.[12,13] On the other hand, for NP depths exceeding 200nm, $E_{LSPR}$ becomes smaller than $E_{g(GaAs)}$. In addition, for $d_{Ga}$ = 66 nm, $E_{LSPR}$ is in the vicinity of or smaller than $E_{g(GaAs)}$, independent of NP depth, suggesting that resonant energy transfer from Ga NP to GaAs NP is negligible. From the absorption enhancement and LSP-excitation, we calculate EHP concentration with and without Ga NP arrays. The EHP concentration from bulk GaAs, $n_{GaAs}$, is estimated to be $2.64\times10^{15}$ $cm^{-3}$, assuming incident laser power of 0.38mW, beam spot area of $1.57\times10^{-6}$ $cm^2$, and GaAs absorption coefficient of $3.89\times10^4$ $cm^{-1}$ at $\lambda$=633nm. The predicted EHP concentration for each NP size and depth, $n_{NP}$, is calculated according to $n_{NP} = n_{GaAs}(\alpha_{nanocomposite}/\alpha_{GaAs})(1+\Omega_{NP}/\Omega_{GaAs})$, as shown in Fig. 3.11 (c). The highest $n_{NP}$ values are predicted for $d_{Ga}$ = 40nm at a depth < 100nm.

### 3.6.4 Electron Transfer via DET process

Besides the EHP generation enhancement due to absorption enhancement and RET process, the electron transfer between semiconductors and metal NPs takes place when they are directly in contact each other. Depending on the band structures of semiconductor

and metal, the electrons can transfer from semiconductor (metal) to metal (semiconductor). When the Fermi level of metal is located below the conduction band (CB) level of semiconductor, the excited electrons in the semiconductor CB transfer to metal due to a direct electron transfer (DET) process, leading to the loss of charge carriers in the semiconductor. Since the electron affinity of GaAs is 4.07 eV and the Fermi energy of Ga is 4.25 eV, the electrons can easily transfer from GaAs to Ga NP at the interface, and consequently the free charge carrier density in GaAs is expected to decrease. Using GaAs absorption coefficient of $3.89\times10^{-4}$ $cm^{-1}$, the incident radiation energy of 1.956eV, and the incident optical power of 0.38mW, we quantify the number electrons generated by the incident radiation through a 1um-thick GaAs for the cases of bulk GaAs and GaAs/Ga NP nanocomposites. For this calculation, we assume that all photoexcited electrons in the vicinity of Ga NP arrays transfer to Ga NPs, and the absorbed optical power below the depth of NP arrays is decreased to 72% (for $d_{Ga}$=40nm) and 70% (for $d_{Ga}$=66nm) from the intrinsic absorbed power since the fill factors of Ga NP arrays are 28% (for $d_{Ga}$=40nm) and 30% (for $d_{Ga}$=66nm). The fraction of electrons transferred from GaAs CB to Ga $E_f$ is predicted to be 0.3 – 0.03 independent of NP sizes, decreasing with increasing NP depth. For NP depth of 20nm, the fraction of photoexcited electrons which can contribute to radiative emission, 70 % of photoexcited electrons are expected to recombine with radiative emission due to 30 % of photoexcited electron transfer to Ga NPs. However, for the fabricated GaAs:Ga nanocomposites, we assume that a monolayer-thick Ga oxide ($Ga_2O_3$) film was formed during the sample transfer from a FIB chamber to a MBE intro chamber.[34,35,36] Thus, we assume that the influence of direct electron transfer on EHP generation is negligible.

### 3.6.5 NP-induced Spontaneous Emission reduction

It has been established that the radiative recombination enhancement is possible through SPR coupling to the emission wavelength mainly due to the enhancement of spontaneous emission (SE) rate. To examine the influence of Ga NP arrays on the enhancement of SE rate, we calculated the Purcell enhancement factor (F) using Lumerical FDTD simulations, which quantifies the increase in the SE rate vs. NP depth, according to Eq. 3.5 and 3.6.

$$F = \frac{3}{4\pi^2}\frac{\lambda^3}{n^3}\frac{Q}{V_{mode}} \tag{3.5}$$

$$\text{SE rate ratio} = F\left(\frac{E(r)\mu}{|E_{max}||\mu|}\right)^2\left(\frac{1}{1+4Q^2\left(\lambda_{incident}/\lambda - 1\right)^2}\right) \tag{3.6}$$

As shown in Fig. 3.12 (a), the resulting SE rate ratios are below 1, suggesting that the SE rate is decreased with NP arrays, presumably due to the NP size- and depth-dependent $E_{LSPR}$. Figure 3.12 (b) shows the plot of the extracted $E_{LSPR}$ from Ga NP absorptance spectra vs. NP depth. The $E_{LSPR}$ values are NP size- and depth-dependent, decreasing with increasing NP size and increasing NP depth, presumably due to the Ga NP-induced changes of permittivity in the nanocomposites. To estimate NP size- and depth-dependent permittivity, we use Maxwell-Garnett effective medium approximations. In Fig. 3.12 (c), the calculated effective permittivity values for $d_{Ga}$=66nm is greater than that for $d_{Ga}$=40nm, and increases close to the bulk GaAs permittivity of 12.35 with increasing NP depth. Thus, the NP size- and depth-dependent $E_{LSPR}$ is attributed to the variations in the effective permittivity.

### 3.7 PL Enhancement Comparison of Theory and Experiment

Figure 3.13 shows the comparison between the measured GaAs PL enhancement ratio and the product of predicted fractions of absorption enhancement, LSP-excitation by RET process, and SE rate enhancement for (a) $d_{Ga}$= 40nm and (b) 66nm vs. NP depth. The PL enhancement is calculated according to Eq. 3.7.

$$\text{PL intensity} = \frac{n_{GaAs}}{\tau_{GaAs}}\left(\frac{\alpha_{NC}}{\alpha_{GaAs}}\right)\left(1+\frac{\Omega_{NP}}{\Omega_{GaAs}}\right)\left(\frac{1/\tau_{NC}}{1/\tau_{GaAs}}\right) \tag{3.7}$$

The decreasing trends of the measured and predicted enhancement ratios with increasing NP depth up to 100nm are similar for both $d_{Ga}$=40nm and 66nm cases. Based on the predicted influence of absorption enhancement, LSP-excitation by RET process, it is likely that the enhancement in GaAs NBE emission is attributed to the EHP generation enhancement induced by Ga NP arrays, which overwhelms the SE rate reduction. On the other hand, for $d_{Ga}$=66nm, the PL emission is reduced, presumably due to the lower SE rate ratios and the insignificant of absorption enhancement in this case.

### 3.8 Conclusions

In summary, we have examined the formation of embedded Ga NP arrays and their influence on GaAs NBE PL efficiency. Close-packed embedded arrays of $d_{Ga}$=40 and 66 nm were fabricated using off-normal FIB irradiation, followed by MBE overgrowth. We consider the influence of embedded Ga NP arrays on the electron transfer at the NP/GaAs interface and the absorption enhancement, using FDTD simulations. We identify a regime

of NP size and depth where NP-induced EHP generation enhancement by absorption and SP-excitation are enhanced, leading to enhanced NBE emission from GaAs. This approach provides an opportunity to enhance the PL efficiency from a variety of semiconductor heterostructures, using a seamless approach to embed non-noble metals during epitaxy.

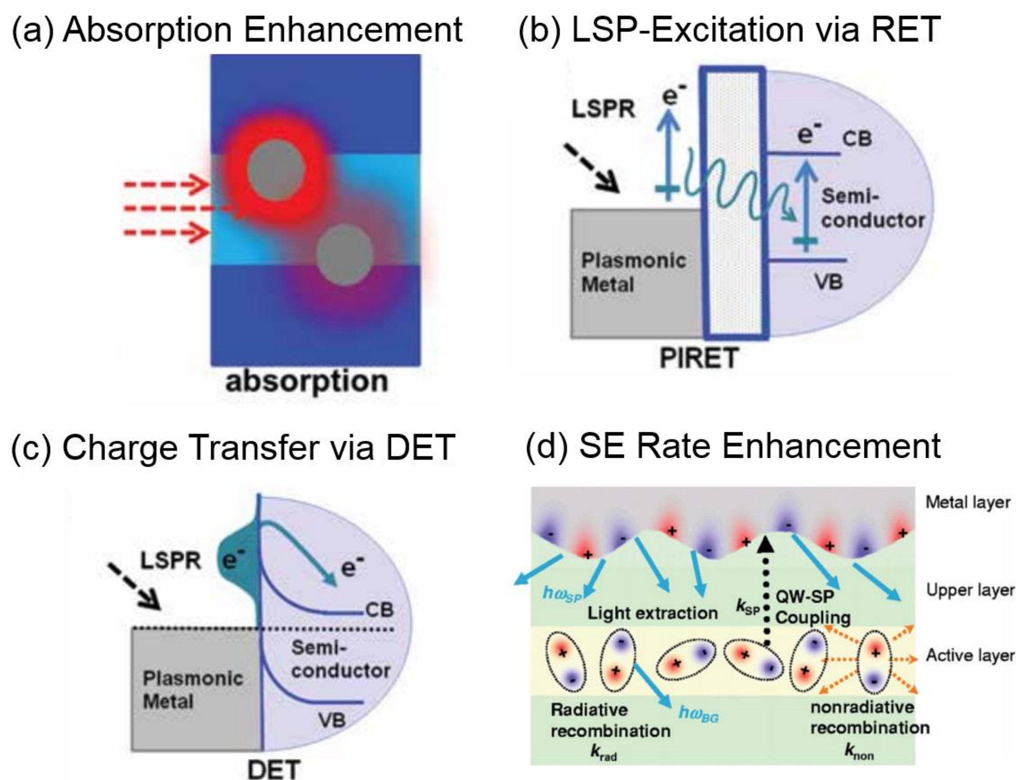


Fig. 3.1 Light-matter interactions at the interface of metal and semiconductor: (a) Absorption enhancement in plasmonic metal-semiconductor hetero-structures by localizing the incident field. Reprinted figures with permission from X. Lu *et al. Rev. Phys. Chem.* **60**, 167 (2009). (b) Plasmon-induced resonant energy transfer (RET) from metal to semiconductor, leading to charge separation in semiconductor. Reprinted figures with permission from S.K.Cushing *et al. The Electrochemical Society Interface* **66** (2013). (c) plasmon-induced direct electron transfer (DET) from metal(semiconductor) to semiconductor(metal), Reprinted figures with permission from S.K.Cushing *et al. The Electrochemical Society Interface* **66** (2013). (d) Semiconductor energy transferred to metal SP, leading to enhanced decay rate through semiconductor-SP coupling. Reprinted figures with permission from K. Okamoto *et al. Appl. Phys. Lett.* **87**, 071102 (2005).

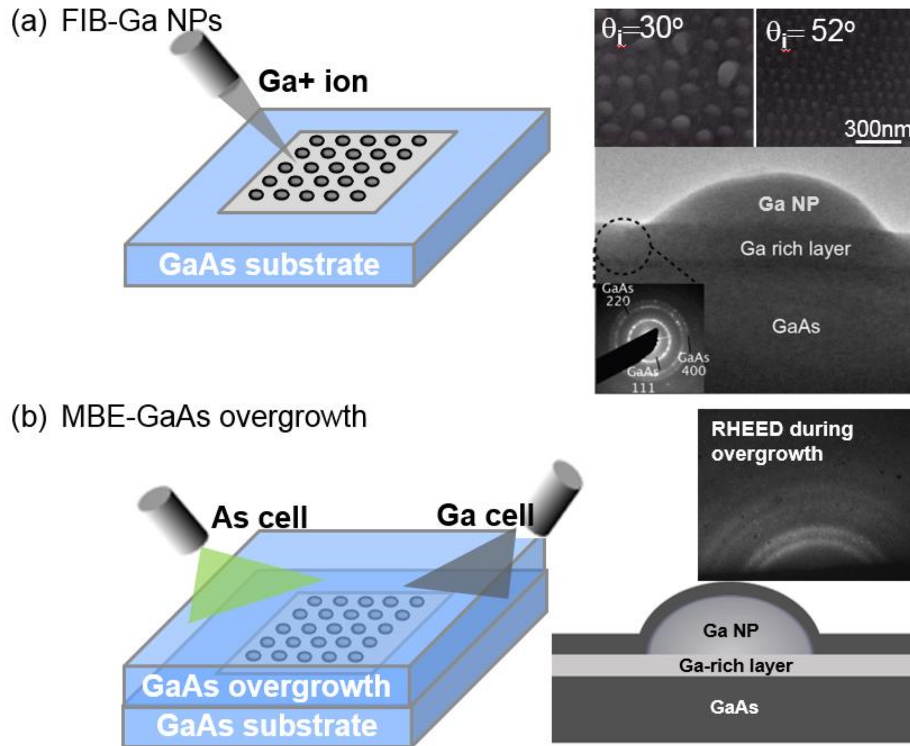


Fig. 3.2 A schematic diagram depicting the fabrication of embedded GaAs:Ga nanocomposites: (a) 2D close-packed Ga NP arrays using FIB system (left), SEM images collected from the Ga NP arrays fabricated on GaAs at $\theta_i = 30°$ and $52°$ (right-top), and cross-sectional TEM image of FIB-fabricated Ga NP showing Ga rich amorphous layer between Ga NP and GaAs (right-bottom). (b) MBE GaAs overgrowth of Ga NP arrays (left), concentric ring RHEED patterns collected during GaAs overgrowth (right-top), and a schematic diagram of cross-sectional structure of embedded GaAs:Ga nanocomposites (right-bottom).

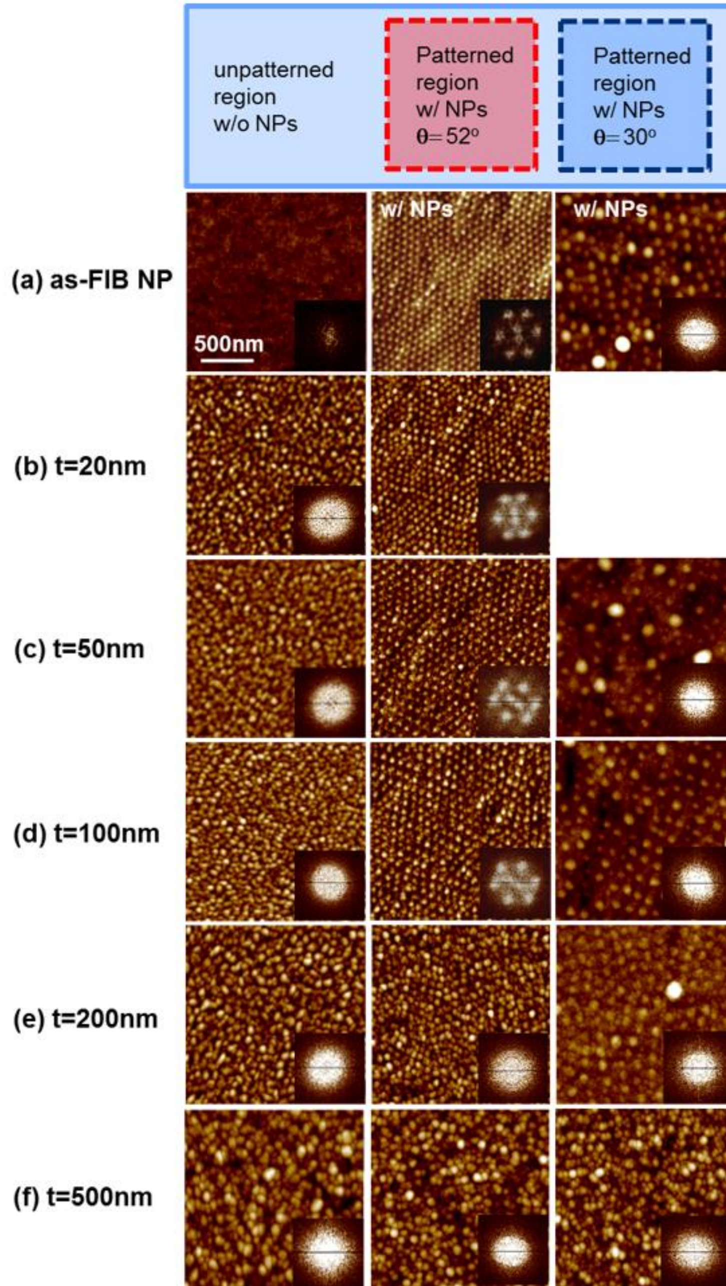


Fig. 3.3 AFM images of unpatterned regions (left), FIB-patterned regions at $\theta_{ion}$ = 52° (middle), and FIB-patterned regions at $\theta_{ion}$ = 30° (right) for NP depth of (a) 0nm (i.e. as-FIB NP), (b) 20nm, (c) 50nm, (d) 100nm, (e) 200nm, and (d) 500nm, with corresponding fast Fourier transforms (FFTs) as insets. For $d_{Ga}$ = 40 nm ($\theta_{ion}$ = 52°) NP arrays with depths of 0 - 100 nm, elongated close-packed surface arrays are observed, containing hexagonal FFT patterns including split center spots. For $d_{Ga}$ = 40 nm NP arrays with depths of 500nm and $d_{Ga}$ = 66 nm $\theta_{ion}$ = 30°) NP arrays with depths of 0 – 500nm, circular FFT patterns are observed, indicating an isotropic distribution of surface features.

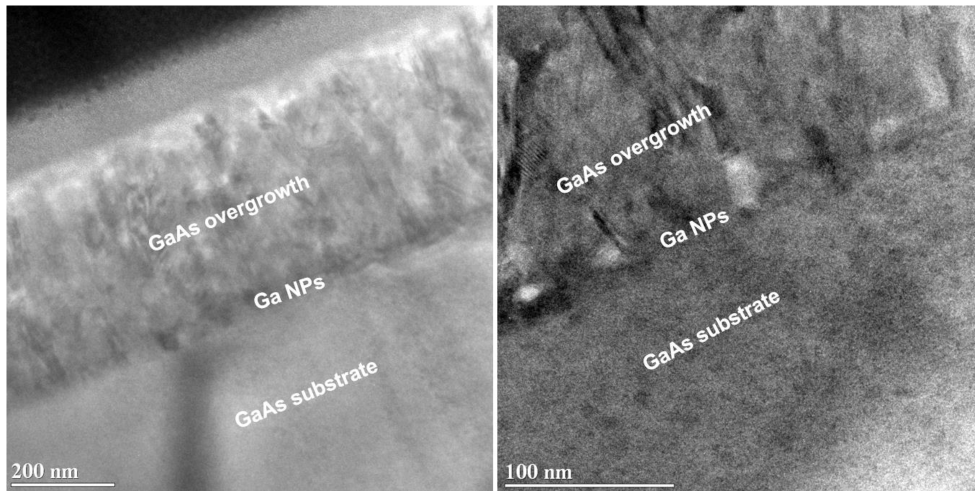


Fig. 3.4 cross-sectional HRTEM images of embedded GaAs:Ga nanocomposite with $d_{Ga}$=40nm and NP depth=500nm. The GaAs overgrown layer exhibits polycrystalline structure.

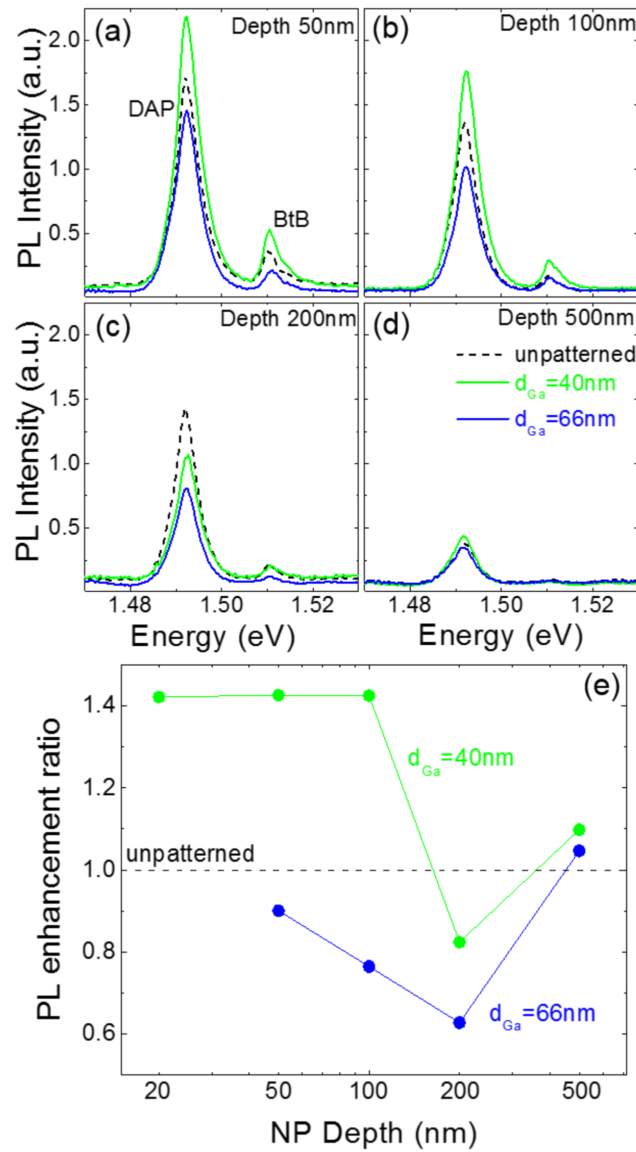


Fig. 3.5 GaAs PL intensities for both patterned regions with $d_{Ga}$=40nm and 66nm (green and blue line), in comparison with that from the unpatterned regions (black dashed line), for NP depth of (a) 50 nm, (b) 100nm, (c) 200nm, and (d) 500nm. The GaAs NBE emission, including BtB emission at 1.515 eV and DAP emission at 1.491 eV, are apparent. For $d_{Ga}$=40nm (66nm), DAP and BtB emissions are enhanced (reduced) in the presence of Ga NPs whose depths are ≤100nm. For NP depth of 200nm, the emission intensity is reduced for the patterned region, in comparison to the unpatterned region. For NP depth=500nm, the PL spectra from the patterned and unpatterned regions are similar.

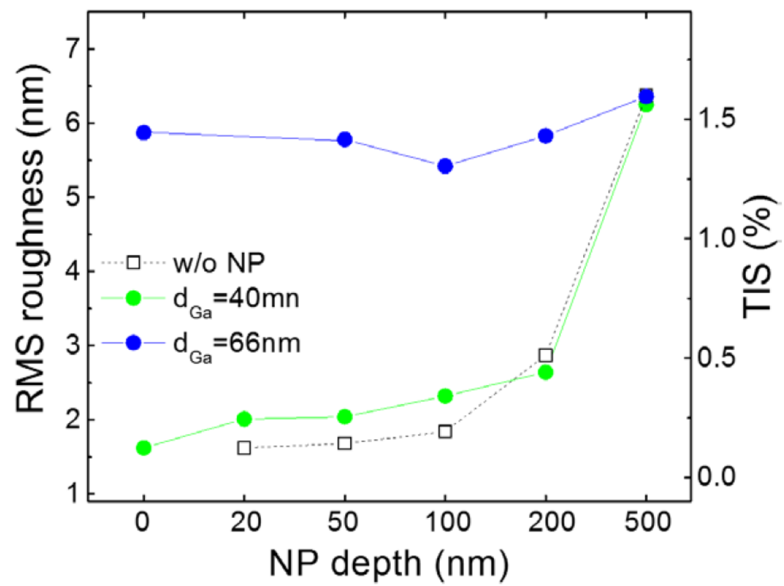


Fig. 3.6 NP depth dependence of RMS roughness (left) and TIS (right) for the unpatterned regions (black dashed line) and patterned regions with $d_{Ga}$=40nm and 66nm (green and blue line).

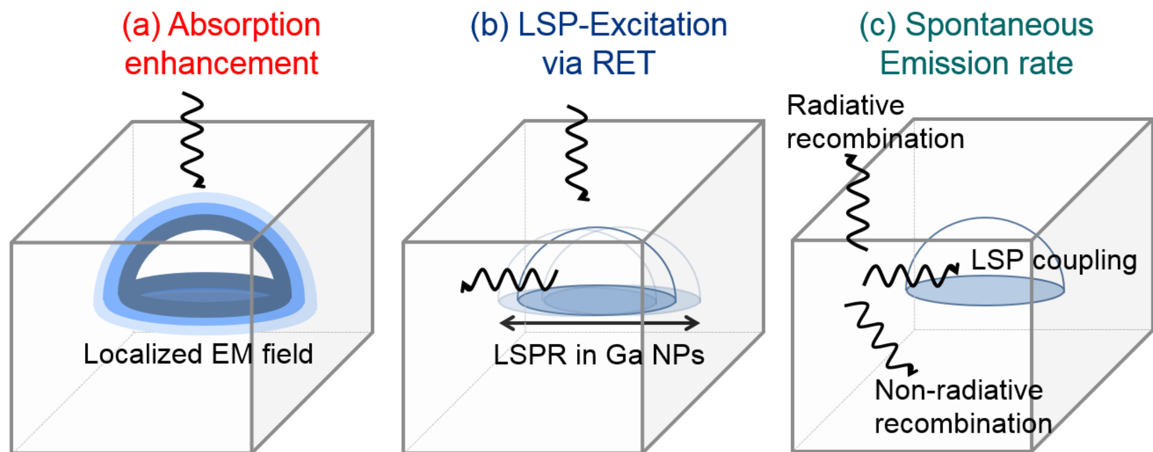


Fig. 3.7 PL enhancement mechanisms considered in the GaAs:Ga nanocomposites (a) Absorption enhancement induced by localized EM field due to LSPR of Ga NPs. (b) LSP-excitation via RET from Ga NP to GaAs. (c) SE rate enhancement through LSP coupling.

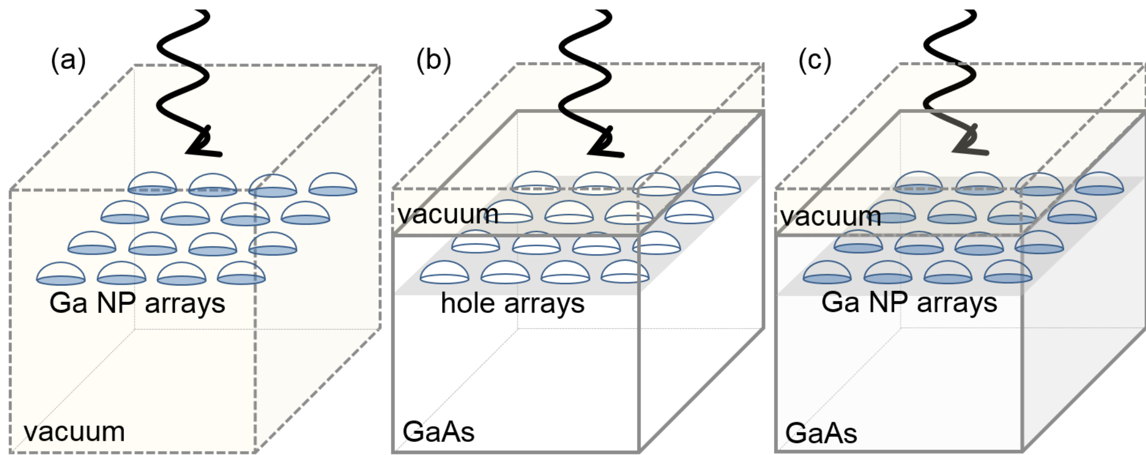


Fig. 3.8 schematic diagrams of FDTD absorptance simulation geometries. The simulation volume is a cube of 1 $um^3$ of GaAs with a 25nm-thick vacuum layer on the top. The hemi-spheroidal Ga NP arrays are buried at different depths ranging from 20 to 500 nm below the GaAs surface. (a) Ga NP arrays in vacuum, (b) GaAs with hole arrays at the position of Ga NP arrays, and (c) GaAs with Ga NP arrays.

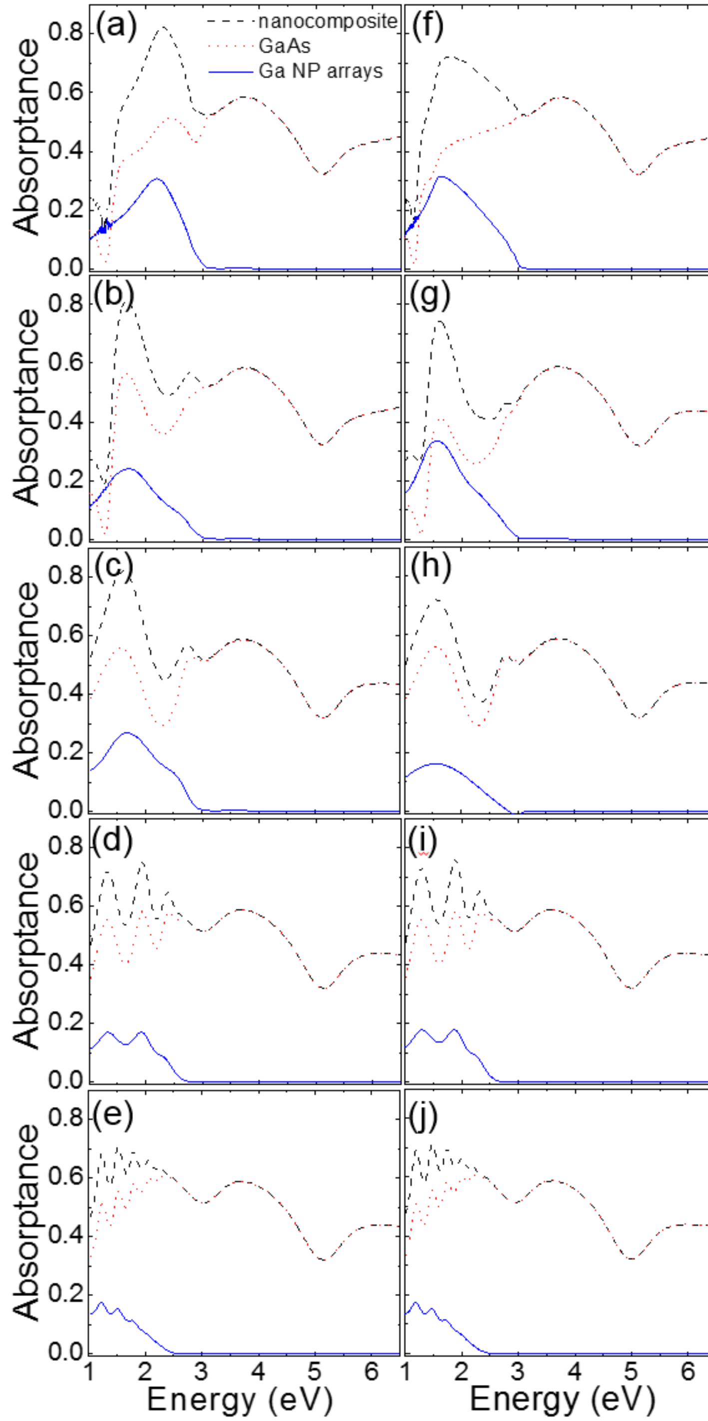


Fig. 3.9 The simulated absorptance for (a)–(e) $d_{Ga}$=40nm and (f)-(j) $d_{Ga}$=66nm at the NP depths of 20nm, 50nm, 100nm, 200nm, and 500nm. It is apparent that the absorptance of the Ga NP arrays shows maxima between 1 and 3eV, coinciding with the reported LSPR of Ga NPs on GaN (1.5 – 2.4eV) and on GaAs (1.4 – 2.0eV).

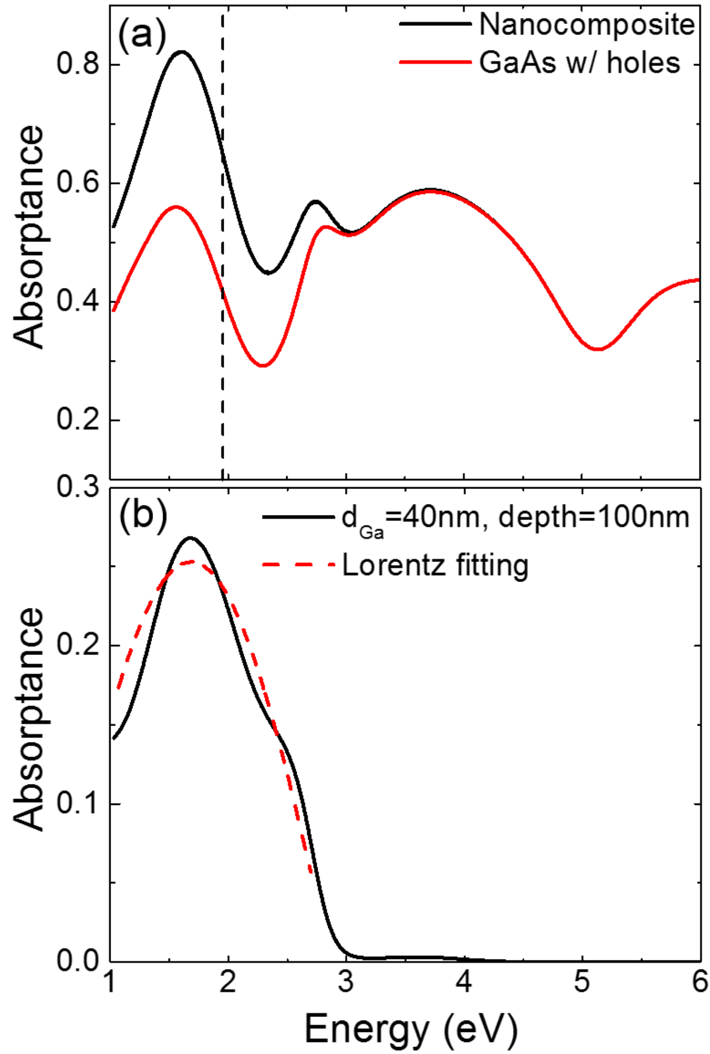


Fig. 3.10 (a) the absorptance spectrum of the nanocomposite (black line) and the GaAs matrix with hole arrays in the positions of Ga NP arrays (red line). The vertical dashed line indicated the incident photon energy of 1.956eV. (b) the absorptance spectrum of Ga NP arrays with $d_{Ga}$=40nm and NP depth=100nm.

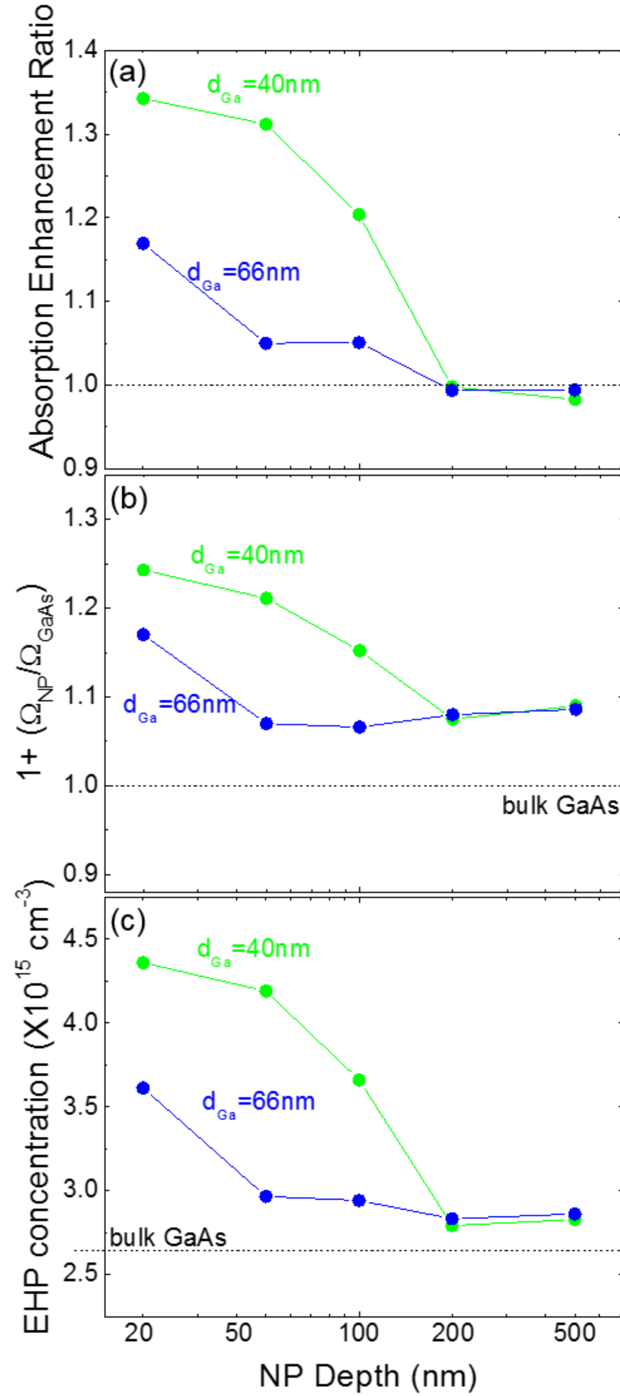


Fig. 3.11 (a) NP depth dependence of the absorption enhancement ratio for $d_{Ga}$=40 and 66nm for NP depths ranging from 20 to 500 nm. The enhancement in absorption is decreasing with increasing NP diameter and depth, due to reduction in E-field enhancement induced by NP arrays. (b) plots of total probability of exciting EHP by RET process and incident radiation vs. NP depth. (c) total EHP concentration generated via absorption enhancement and LSP-excitation vs. NP depth.

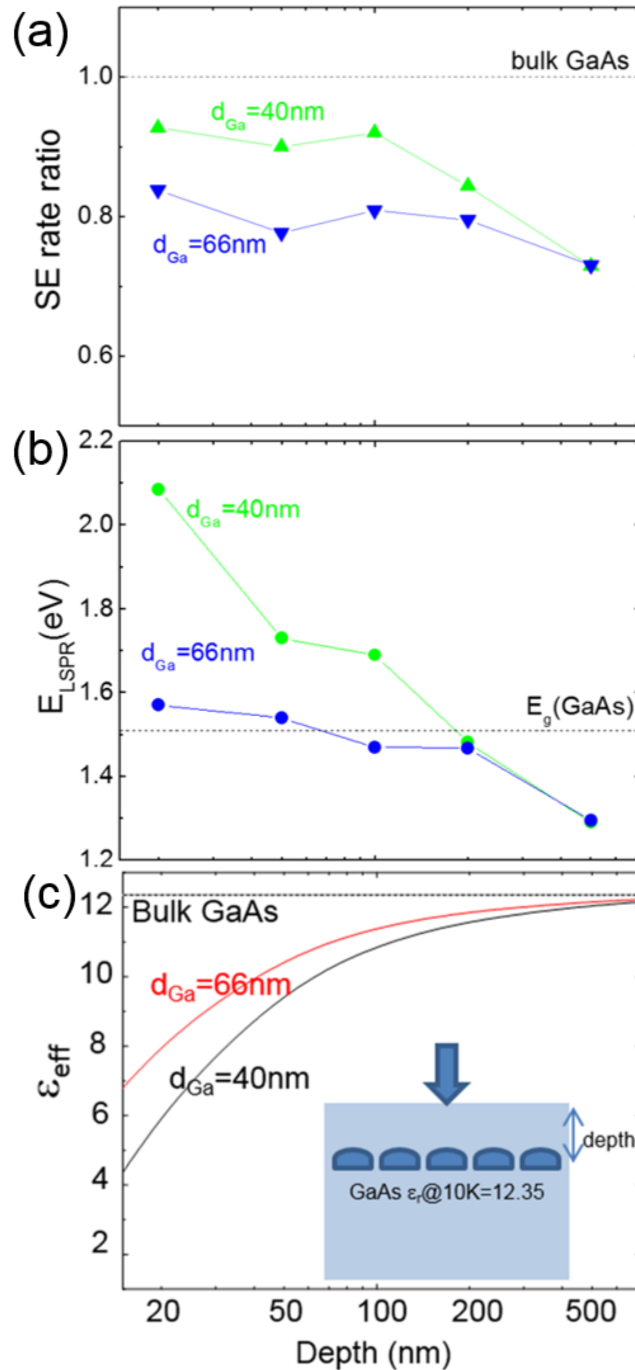


Fig. 3.12 (a) a plot of calculated spontaneous emission rate ratio vs. NP depth. The resulting SE rate ratios are below 1, suggesting that the SE rate is decreased with NP arrays, presumably due to the NP size- and depth-dependent $E_{LSPR}$. (b) a plot of the extracted $E_{LSPR}$ from Ga NP absorptance spectra vs. NP depth.(c) a plot of calculated effective permittivity vs. NP size and depth.

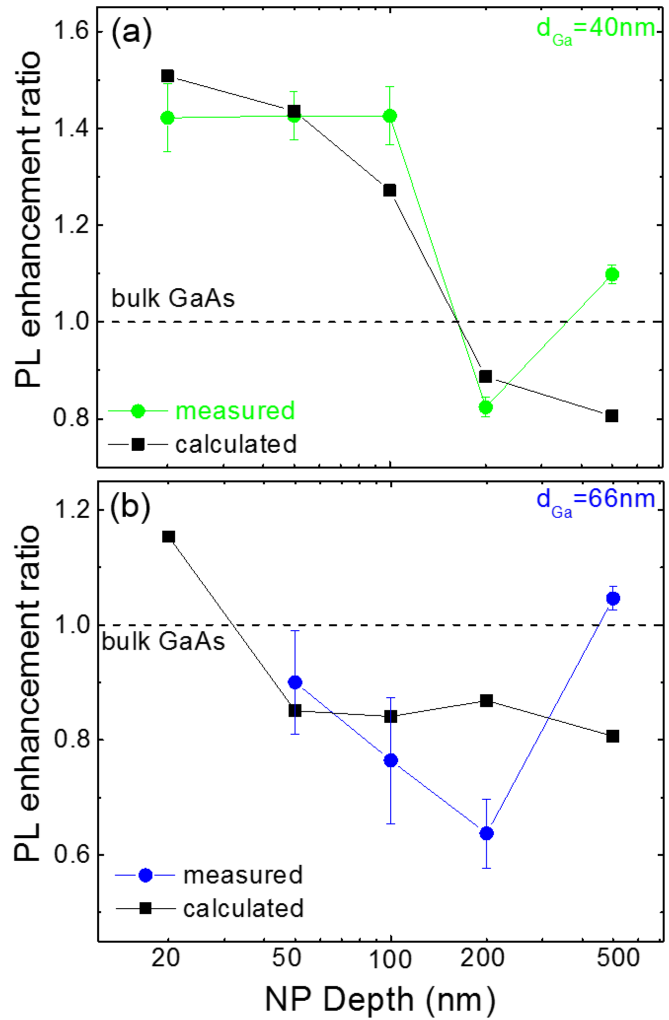


Fig. 3.13 the comparison between the measured GaAs PL enhancement ratio and the product of predicted fractions of absorption enhancement, LSP-excitation by RET process, and SE rate enhancement for (a) $d_{Ga}$= 40nm and (b) 66nm vs. NP depth. The decreasing trends of the measured and predicted enhancement ratios with increasing NP depth up to 100nm are similar for both $d_{Ga}$=40nm and 66nm cases.

### 3.9 References

[1] J. A. Dionne, and H. A. Atwater, *MRS Bull.* **37**, 717 (2012).

[2] O. A. Yeshchenko, I. M. Dmitruk, A. A. Alexeenko, M. Y. Losytskyy, A. V. Kotko, and A. O. Pinchuk, *Phys. Rev. B.* **79**, 235438 (2009).

[3] K. Okamoto, I. Niki, A. Shvartser, Y. Narukawa, T. Mukai, and A. Scherer, *Nature Mater.* **3**, 601 (2004).

[4] H. A. Atwater, and A. Polman, *Nature Mater.***9**, 205 (2010).

[5] A. J. Haes, S. L. Zou, G. C. Schatz, and R. P. Van Duyne, *J. Phys. Chem. B* **108**, 6961 (2004).

[6] C. M. Soukoulis, S. Linden, and M. Wegener, *Science* **315**, 47 (2007).

[7] S. Pillai, K. R. Catchpole, T. Trupke, and M. A. Green, *J. Appl. Phys.* **101**, 093105 (2007).

[8] C. W. Cheng, E. J. Sie, B. Liu, C. H. A. Huan, T. C. Sum, H. D. Sun, and H. J. Fan, *Appl. Phys. Lett.* **96**, 071107 (2010).

[9] G. Xu, M. Tazawa, P. Jin, S. Nakao, and K. Yoshimura, *Appl. Phys. Lett.* **82**, 3811 (2003).

[10] H. Mertens, J. Verhoeven, A. Polman, and F. D. Tichelaar, *Appl. Phys. Lett.* **85**, 1317 (2004).

[11] G. Sun, J. B. Khurgin, and R.A. Soref, *Appl. Phys. Lett.* **94**, 101103 (2009).

[12] P. Spinelli and A. Polman, *Opt.Express* **20**, A641 (2012).

[13] M. P. Hanson, A. C. Gossard, and E. R. Brown, *J. Appl. Phys.* **102**, 043112 (2007).

[14] Y.P. Hsieh, C.T. Liang, Y.F. Chen, C.W. Lai, and P.T. Chou, Nanotechnology 18, 415707 (2007).

[15] C. W. Chen, C. H. Wang, C. M. Wei, and Y. F. Chen, *Appl. Phys. Lett.* **94**, 071906 (2009).

[16] M. De Lourdes Ruiz Peralta, U. Pal, and R. Sanchez Zeferino, *ACS Appl. Mater. Interfaces* **4**, 4807 (2012)

[17] X. D. Zhou, X. H. Xiao, J. X. Xu, G. X. Cai, F. Ren, and C. Z. Jiang, *EPL*, **93**, 57009 (2011).

[18] Quality factors are defined by the resonance frequency and the broadening induced by intrinsic losses.

[19] M. Kang, T. W. Saucer, M. V. Warren, J. H. Wu, H. Sun, V. Sih, and R. S. Goldman, *Appl. Phys. Lett.* **101**, 081905 (2012).

[20] P. Wu, T. Kim, A. Brown, M. Losurdo, G. Bruno, and H. Everitt, *Appl. Phys. Lett.* **90**, 103119 (2007).

[21] M. Kang, A. A. Al-Heji, J. Lee, T. W. Saucer, J. H. Wu, L. Zhao, A. L. Katzenstein, D. L. Sofferman, V. Sih, and R. S. Goldman, *Appl. Phys. Lett.* **103**, 101903 (2013).

[22] Q. Wei, J. Lian, W. Lu, and L. Wang, *Phys. Rev. Lett.* **100**, 076103 (2008).

[23] M. Kang, J. H. W, D. L. Sofferman, I. Beskin, H. Y. Chen, K. Thornton, and R. S. Goldman, *Appl. Phys. Lett.* **103**, 072115 (2013).

[24] H. E. Bennett, and J. O. Porteus, *J. Opt. Soc. Am.* **51**(2), 123 (1961).

[25] P. B. Perry and A. E. Blakeslee, *J. Elec. Mater.* **8**(5), 635 (1979).

[26] J. E. Harvey, S. Schroder, N. Choi, and A. Duparre, *Opt. Eng.* **51**(1), 013402 (2012).

[27] M. W. Knight, T. Coenen, Y. Yang, B. J. M. Brenny, M. Losurdo, A. S. Brown, H. O. Everitt, and A. Polman, *ACS Nano* **9**, 2049 (2015).

[28] M. Scalora, M. A. Vincenti, V. Roppo, J. V. Foreman, J. W. Haus, N. Akozbek, and M. J. Bloemer, *IEEE/LEOS.* 132 (2009).

[29] I.Strzalkowski, S. Joshi, and C. R. Crowell, *Appl. Phys. Lett.* **28**, 350 (1976).

[30] We compute the electric fields within the simulated space, E(x,y,z,ω). The absorbed optical power per unit volume, $P_{abs}$, is then calculated according to

$$P_{abs}(\omega) = \frac{1}{2}\omega \mathrm{Im}(n(x,y,z,\omega))\,\mathrm{E}(\mathrm{x},\mathrm{y},\mathrm{z},\omega)^2 .$$

[31] H. R. Phillip, and H. Ehrenreich, *Phys. Rev.* **129**(4), 1550 (1963).

[32] T. S. Ferguson, *J. Am. Statist. Assoc.* **73**(361), 211 (1978).

[33] S. K. Cushing, J. Li, F. Meng, T. R. Senty, S. Suri, M. Zhi., M. Li., A. D. Bristow, and N. Wu, *J. Am. Chem. Soc* **134**, 15033 (2012).

[34] P. C. Wu, T. H. Kim, A. S. Brown, M. Losurdo, G. Bruno, and H. O. Everitt, *Appl. Phys. Lett.*, **90**, 103119 (2007).

[35] P. C. Wu, M. Losurdo, T.-H. Kim, M. Giangregorio, G. Bruno, H. O. Everitt, A. S. Brown, *Langmuir* **25**, 924 (2009).

[36] Y. Yang, N. Akozbek, T-H. Kim, J. M. Sanz, F. Moreno, M. Losurdo, A. S. Brown, and H. O. Everitt, *ACS Photonics,* **1**, 582 (2014).

# Chapter 4

# Droplet Epitaxy of GaN QDs

## 4.1 Overview

In this chapter, we report a growth method of zinc-blende (ZB) GaN quantum dots (QD) by droplet epitaxy (DE), a vapor–liquid–solid (VLS) process. In the DE process, liquid Ga droplets are created and subsequently nitridated to fabricate GaN quantum dots. Metallic nanoparticles on semiconductor surfaces can be converted into semiconductor QDs, which are promising candidates for light-emitting diodes.[1,2,3,4,5,6,7,8,9] Wide-bandgap quantum dots based on group III nitrides, such as the GaN-based material system, are of interest their possible applications in optoelectronic devices, such as blue light-emitting diodes.[10,11,12,13,14] However, the built-in electric fields consisting of spontaneous and piezoelectric polarization induce a Quantum Confined Stark Effect (QCSE), leading to a reduced probability for recombination of electrons and holes.[15,16] Since the QCSE may lead to a red shift of the luminescence and a reduced radiative recombination rate, nonpolar or semipolar orientations of GaN for optoelectronic devices are of increasing interest.[17] The metastable ZB phase of GaN is expected to be free of polarization fields. Recently, the radiative recombination time of cubic GaN QDs has previously been measured to be two orders of magnitude below the recombination time of wurtzite (WZ) GaN QDs.[18] The

minimum size of GaN QDs grown by Stranski-Krastanow (SK) method range from 20 to 35 nm in diameter,[3] which is limited by the misfit strain between the film and substrate. In addition, it has been reported that ZB GaN nanocrystals (NCs) were nucleated in GaAs via matrix-seeded growth, with the maximum NC radius of ~1.75 nm.[19]

Thus, we use the droplet epitaxy (DE) process to produce small QDs, which is not possible by SK approach, in order to obtain ZB phase. First, we present epitaxial WZ and ZB GaN QDs grown on c-plane GaN and r-$Al_2O_3$ substrate. In addition, by varying the surface conditions on Si substrates, GaN QDs grown on Si(001) without oxide desorption, Si(001) with oxide desorption, and Si(111) with oxide desorption show structure selectivity of polycrystalline, zinc-blende (ZB), and wurtzite (WZ) structure, respectively. We demonstrate, for the first time, ZB GaN QDs grown on Si (001) by the DE method, and the size ranges 17nm to 50nm, which is significantly larger than the maximum size of GaN NCs fabricated via matrix-seeded growth.

### 4.2 Background

The fabrication of semiconductor QDs has been demonstrated via various methods, including chemical synthesis,[20] pre-growth lithographic patterning,[21] ion-beam synthesis,[22,] and self-assembled epitaxial growth.[23,24] One of the most commonly used QD growth methods is the misfit-driven SK growth mode.[25,26,27,28] The SK growth generally initiates with deposition of a thin film on a lattice-mismatched substrate, leading to the formation of strained monolayers, as shown in Fig. 4.1 (left). The pseudomorphic layer-by-layer growth continues until the film reaches a critical thickness, which is inversely

proportional to the misfit strain between the film and the substrate,[29,30] at which point a transition from 2D to 3D growth occurs. Although the SK growth mode is convenient and commonly used for the fabrication of many III-V and group IV semiconductor QDs, the size and density of the SK-grown QDs are limited by the misfit between the film and the substrate. On the other hand, semiconductor QDs can also be grown epitaxially by an alternative approach termed "droplet epitaxy (DE)". Proposed by Nobuyuki Koguchi in 1991,[31] the DE technique typically involves deposition of metal droplets or islands on a substrate surface, followed by annealing under a group V flux to convert the metal droplets/islands to semiconductor QDs, as shown in Fig. 4.1 (right). For DE, the QD size and density are not limited by the misfit strain since the formation of metal droplets is driven by surface tension rather than misfit strain.[32] In addition, without the requirement of a lattice mismatch, DE enables QD growth even in lattice-matched systems, such as GaAs/AlGaAs and GaAs/GaAs.[33] The multi-step process of DE growth also allows the fabrication of a wide range of nanostructures. By varying the As flux used for annealing the metal droplets, quantum rings or even concentric double-ring structures are achievable via DE.[34,35] Recently, Somaschini et al. have demonstrated GaAs nanostructures with tunable aspect ratios on Si (ranging from low aspect ratio QDs to high aspect ratio nanowires), where the GaAs QDs formed by DE are used as seeds for NW growth.[36] The high tunability of QD density and size by DE is exploited to tailor the NW density and size without using metal catalysts, which opens up opportunities for integrating III-V semiconductors on Si.

Wide-bandgap GaN QDs are of great interest for their possible applications in optical and quantum optical devices. For WZ GaN, the built-in electric fields induce a

quantum confined Stark effect (QCSE),[37] leading to a reduced recombination probability of electrons and holes in confined states, while ZB GaN has no polarization fields.[38,39] To fabricate group III-nitride quantum dots using self-assembly, the SK and DE method have been applied with the minimum sizes ranging ~10 to 30 nm.[40,41,42,43,44,45,46,47] GaN QDs have been achieved using DE on various substrates such as AlGaN on 6H-SiC(0001),[9] c-$Al_2O_3$,[48] Si(111),[49, 50, 51] and AlN on 3C-SiC(001),[27,38,39,52] with either $NH_3$-gas source MBE[9, 37] and N plasma MBE.[36, 38, 39, 40, 41, 42, 43] The crystal structures of GaN QDs by DE method is determined by the structure of substrates showing WZ on 6H-SiC(0001)[9], and ZB on 3C-SiC(001),[40,41,42,43] and the QD density and size can be controlled by varying exposed Ga amount for droplet formation,[39, 42, 43] nitridation temperatures,[9,37,39] and plasma power.[39]

To form small-sized and close-packed GaN QDs, we investigated the self-assembly of QDs using Ga droplets, which are crystallized on the substrate surface by annealing in the presence of nitrogen species. Here, we have studied the influence of substrate orientations using Si (100) and r-plane sapphire substrates for epitaxial growth, as well as the influence of nitridation temperatures on QD size distribution and densities.

### 4.3 Experimental Details

The GaN QDs were grown on epi-ready c-GaN[1], epi-ready r-$Al_2O_3$, Si (001), and Si (111) substrates by molecular beam epitaxy (MBE), using solid Ga and rf N plasma

---

[1] c-GaN bulk substrates were obtained from Kyma technologies.

sources, as shown in Fig. 4.2. The growths on different substrates were done separately. For c-GaN and r-$Al_2O_3$ wafers, there was no chemical or thermal cleaning applied. For Si wafers, the substrates were cleaned with a 5% HF solution, consisting of 2mL of 49% HF and 18mL of DI water, to remove native silicon oxides. Following HF cleaning, the substrates were transferred to the MBE chamber for GaN growth. Prior to growth, each Si sample was thermally cleaned by raising $T_s$ to 900ºC for 10 minutes to ensure complete desorption of surface oxide. Some of the Si (001) samples were not heated up to $T_s$=900 °C, leaving a native oxide layer on the surfaces.

For Ga droplet formation, the substrate temperature ($T_s$) was decreased to 185 °C for c-GaN, 30 °C for r-$Al_2O_3$[53] and 550 °C for Si, and the growth chamber background pressure gradually dropped to < $1.5\times 10^{-9}$ Torr. At $T_{Ga}$, and 7.5 ML (5.5ML, 205ML) Ga was deposited with a rate of 0.75 ML/s (0.55ML/s, 0.68 ML/s) for Si (c-GaN, r-$Al_2O_3$) substrates. Following Ga droplet formation, nitridation of Ga droplets was performed at an elevated substrate temperature of 185°C for r-$Al_2O_3$, 800°C for r-$Al_2O_3$ and various temperatures of 550, 650, and 720°C for Si under an active nitrogen plasma flux. N plasma power and flux were fixed to be 350W and $1.0\times10^{-6}$ Torr, monitored by the partial pressure of 14 amu measured with a residual gas analyzer.

The surface morphology of the Ga droplets before and after nitridation was examined *ex situ* with tapping mode atomic force microscopy (AFM), using etched Si probes. The crystallinity of GaN QDs on r-$Al_2O_3$ was determined using x-ray diffraction (XRD), conducted with a 12 kW Rigaku rotating anode source (Cu target and graphite monochromator) at an incident angle ($\theta_i$) of 0.3° for grazing incident (GI) XRD. Spatially-resolved PL measurements were performed on samples mounted in a liquid-He flow cryostat operating at 10 K, using a Ti-Sapphire laser with 267 nm excitation wavelength,

incident laser power of 0.38 mW, and a 5 μm-diameter beam spot. The PL measurements were done by Tyler Hill in Prof. Deng's research group.

## 4.4 Droplet Epitaxy on c-GaN substrates

We describe Ga droplet nucleation and conversion to GaN QDs for DE on c-plane GaN. Figure 4.3 shows RHEED patterns collected during outgassing along (b) <1100> axis, (c) <2110> axis, during Ga droplet formation along (d) <1100> axis, (c) <2110> axis, and during nitridation along (f) <1100> axis, (g) <2110> axis, with a schematic atomic structure of WZ c-plane GaN in Fig. 4.3 (a). As shown in Fig. 4.3 (b) and (c), a c-plane GaN surface shows a streaky RHEED pattern, suggesting a flat surface. Once Ga deposition starts, the surface is covered with Ga, leading to hazy RHEED patterns shown in Fig. 4.3. (d) and (e). Finally, during nitridation on Ga droplets, spotty RHEED patterns appear in the WZ c-plane GaN diffraction streaks, suggesting epitaxial growth of WZ GaN QDs on c-GaN. Figure 4.4 (a) and (b) show the AFM images of the sample surface (a) before and (d) after GaN DE. The resulting diameter and height of GaN QDs grown on c-GaN are 22 ± 2.8 nm and 2.8 ± 1.6 nm, respectively, with a QD density of $2.2\times10^{11}$ $cm^{-2}$. To examine the atomic coherency between a c-GaN substrate and GaN QDs, high resolution TEM (HRTEM) was performed, as shown in Fig. 4.4 (c). The HRTEM images show the coherent atomic alignments between the substrate and GaN QDs, suggesting the epitaxial growth of GaN QDs.

## 4.5 Droplet Epitaxy on r-$Al_2O_3$ substrates

For GaN DE on r-$Al_2O_3$, we describe the nucleation of Ga droplets and their conversion to GaN QDs. Figures 4.5 (a) and (b) show AFM images collected before and after nitridation. Prior to nitridation, the AFM image, presented in Figure 4.5 (a), shows Ga droplet diameter of 90 ± 20 nm. After nitridation, the surface contains GaN QD chains shown in Fig. 4.5 (b), presumably due to a ripening process of the Ga droplets during heating of the sample to nitridation temperature of 800°C. To examine the crystal structure of GaN on r-$Al_2O_3$, we perform GIXRD with an incident angle of 0.3°. The resulting GIXRD data is shown in Fig. 4.5 (c), with an inset of the RHEED pattern collected during nitridation. A diffraction peak at $2\theta = 40°$, corresponding to GaN (002) plane, is observed, revealing the presence of ZB GaN atop the r-$Al_2O_3$ substrate. In addition, the RHEED pattern shows the cubic GaN pattern along <110>. Figure 4.5 (d) shows the PL spectrum of GaN grown on r-$Al_2O_3$, presenting a ZB GaN band-edge emission peak at 3.16eV, with an emission peak at 3.47eV presumably from WZ GaN band-edge. Therefore, growth on r-$Al_2O_3$ allows for the growth of ZB GaN QDs. This is the first demonstration of ZB GaN QDs on semi-polar surfaces via the DE method.

## 4.6 Droplet Epitaxy on Si substrates

RHEED patterns collected during droplet epitaxy of GaN QDs on Si substrates are shown in Fig. 4.6 for (a) Si (001) without oxide desorption, (b) Si (001) with oxide desorption, and (c) Si (111) with oxide desorption. In Fig. 4.6 (a), concentric ring patterns

are observed, suggesting the existence of polycrystalline GaN. This is presumably due to the thin silicon oxide layer that inhibits the epitaxial growth of GaN QDs. For the growth on Si(001) with oxide desorption shown in Fig. 4.6 (b), the RHEED patterns consist of cubic spots, suggesting the existence of cubic phase GaN QDs. Finally, in Fig. 4.6 (c), for growth on Si(111) with oxide desorption, the hexagonal spotty patterns are observed, presumably due to the formation of WZ GaN QDs. The growth process of GaN QDs on Si(001) with oxide desorption consists of the nucleation of Ga droplets on the cubic Si surface and subsequent crystallization of Ga droplets to form GaN.

For a detailed analysis on the RHEED pattern changes during ZB GaN QDs growth on Si(001) with oxide desorption, Fig. 4.7 (a) and (b) present the Si and GaN atomic structures on (100) planes along <100> and <110> axis. The lattice constants of cubic-Si and GaN are 0.543nm and 0.452nm, respectively. Figure 4.8 presents the RHEED patterns of the sample grown on thermally cleaned Si (001), collected during (a) Si surface along Si<100> axis, (b) Si surface along Si<110>, (c) 7.5ML Ga droplet deposition along Si<100> axis, (d) 7.5ML Ga droplet deposition on along Si<100> axis, (e) nitridation on along GaN <100> axis, and (f) nitridation on along GaN <110> axis. Before growth, the Si surface was annealed in situ and the surface quality of the Si 2×1 reconstruction was verified by RHEED at $T_{sub} = 880^{\circ}C$, as shown in Fig. 4.8 (a) and (b). The distances between the streaks are $0.184A^{-1}$ and $0.260A^{-1}$, which correspond to the planar distance of the Si (100) and Si (110) planes, respectively. Figure 4.8 (c) and (d) show the RHEED patterns collected during 7.5ML Ga deposition for Ga droplet formation. The RHEED patterns become diffuse, presumably due to Ga-coverage of the Si surface. Finally, the RHEED patterns collected during nitridation show spotty patterns indicative of cubic phase GaN

QDs, with inter-streak distances of $0.221A^{-1}$ and $0.313A^{-1}$, which correspond to the planar distance of GaN (100) and GaN (110) planes.

Following growth, the surface morphologies were examined via AFM, as shown in Fig. 4.9 for (a) Ga droplets at $T_{Ga}$=550°C, (b) GaN QDs at $T_{nit}$=550°C, (c) 650°C, (d) 720°C for Si (001) without oxide desorption, (e) Ga droplets at $T_{Ga}$=550°C, (f) GaN QDs at $T_{nit}$=550°C, (g) 650°C, (h) 720°C for Si (001) with oxide desorption, and (i) Ga droplets at $T_{Ga}$=550°C, (j) GaN QDs at $T_{nit}$=550°C, (k) 650°C, (l) 720°C for Si (111) with oxide desorption. In all cases, the corresponding QD diameter distributions are presented in Fig. 4.10 (a)-(c). We fit the diameter distributions with a Gaussian distribution for GaN QD frequency as a function of diameter and used the maximum likelihood estimation method to obtain the most probable QD diameter, which is equivalent to the mean diameter. The corresponding GaN QD size distributions are presented in Fig. 4.10 (a)-(c) with the frequency defined as the percentage of islands with diameters within a specified range. Interestingly, the QD size distributions show the trend of increasing QD size with increasing nitridation temperatures. Figure 4.11 (a)-(c) show the plots of the (a) density, (b) mean diameter, and (c) mean height of Ga droplets and GaN QDs grown at 550, 650, and 720°C vs. nitridation temperatures. The density, mean diameter and height values of 7.5ML Ga droplets are $1.22 \times 10^{11}$ cm$^{-2}$, 20 ± 5, and 3 ± 1 nm for Si(001) without oxide desorption, $9.6 \times 10^{9}$ cm$^{-2}$, 34.2 ± 3, and 8 ± 2 nm for Si(001) with oxide desorption, $7.5 \times 10^{10}$ cm$^{-2}$, 23 ± 4, and 4.2 ± 2 nm for Si(111) with oxide desorption. These Ga droplet values are similar to those from QDs grown at $T_{nit}$ of 550°C, which suggests a one-to-one conversion from Ga droplets to GaN QDs presumably due to the same Ga deposition temperature and nitridation temperature. On the other hand, it is evident that the QD density

decreases with increasing nitridation temperature, while the mean diameter and height values increase with increasing nitridation temperature. For polycrystalline GaN QDs on Si(001) without pre-growth oxide desorption, the density, mean diameter, and height values range from $1.44 \times 10^{11}$ cm$^{-2}$ to $1.12 \times 10^{10}$ cm$^{-2}$, from 18.2 ± 6 to 39.9 ± 7 nm, and from 2.8 ± 1 to 8.4 ± 2 nm, respectively, indicating decreasing (increasing) trend of density (diameter and height) with increasing nitridation temperatures. For ZB GaN QDs on Si(001) with pre-growth oxide desorption, the density, mean diameter, and height values range from $8.4 \times 10^{9}$ cm$^{-2}$ to $5.5 \times 10^{9}$ cm$^{-2}$, from 35 ± 7 to 53.4 ± 17 nm, and from 7.2 ± 1 to 12.9 ± 4 nm, respectively, indicating decreasing (increasing) trend of density (diameter and height) with increasing nitridation temperatures. For WZ GaN QDs on Si(111) with pre-growth oxide desorption, the density, mean diameter, and height values ranges from $6.4 \times 10^{10}$ cm$^{-2}$ to $6.7 \times 10^{9}$ cm$^{-2}$, from 24 ± 10 to 48.4 ± 14 nm, and from 4.5 ± 2 to 7.1 ± 3 nm, respectively, indicating decreasing (increasing) trend of density (diameter and height)with increasing nitridation temperatures. Increasing the nitridation temperature to 650°C and 720°C apparently induces a coalescence process of Ga droplets during nitridation, leading to decrease in density and increases in diameter and height. In addition, as shown in Fig. 4.12, the estimated GaN QD volume values are in the range of 1.5 – 4.0 $\times 10^{14}$ nm$^{3}$ cm$^{-2}$, which are independent on the nitridation temperature. Thus, it is unlikely that Ga droplets undergo thermal desorption during nitridation at the elevated temperatures of 650°C and 720°C.

### 4.7 Conclusions

In summary, we have investigated the formation of Ga droplets and their conversion to GaN QDs via the DE method with an rf N plasma source. The influence of substrate preparation, and substrate temperature during nitridation on the formation of GaN QDs is examined, with emphasis on QD size distribution and crystallinity. We report epitaxial growths of WZ and ZB GaN QDs on c-plane GaN and r-plane $Al_2O_3$ substrate. In addition, by varying the surface conditions of Si substrates, GaN QDs grown on Si (100) without oxide desorption, Si (100) with oxide desorption, and Si (111) with oxide desorption show polycrystalline, ZB, and WZ structure, respectively. We observe a one-to-one conversion from Ga droplets to GaN QDs when the Ga deposition and nitridation temperatures are equal at 550°C. Increasing the nitridation temperature to 650°C and 720°C apparently induces a coalescence process of Ga droplets during nitridation, leading to decrease in density and increases in diameter and height. This is the first demonstration of ZB GaN QDs nucleation and coalescence process on Si substrates via the DE method.

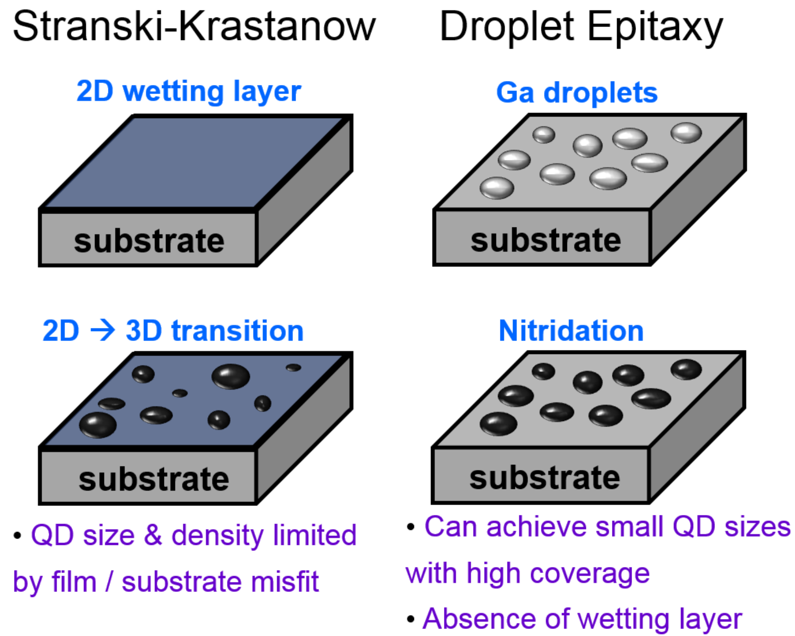


Fig. 4.1 Schematic of QD growth via the (left) Stranski-Krastanov (SK) growth mode where 3D islands form as the wetting layer reaches the critical thickness; (right) droplet epitaxy (DE) growth mode where metal droplets are crystallized into semiconductor QDs via exposure to an nitrogen flux.

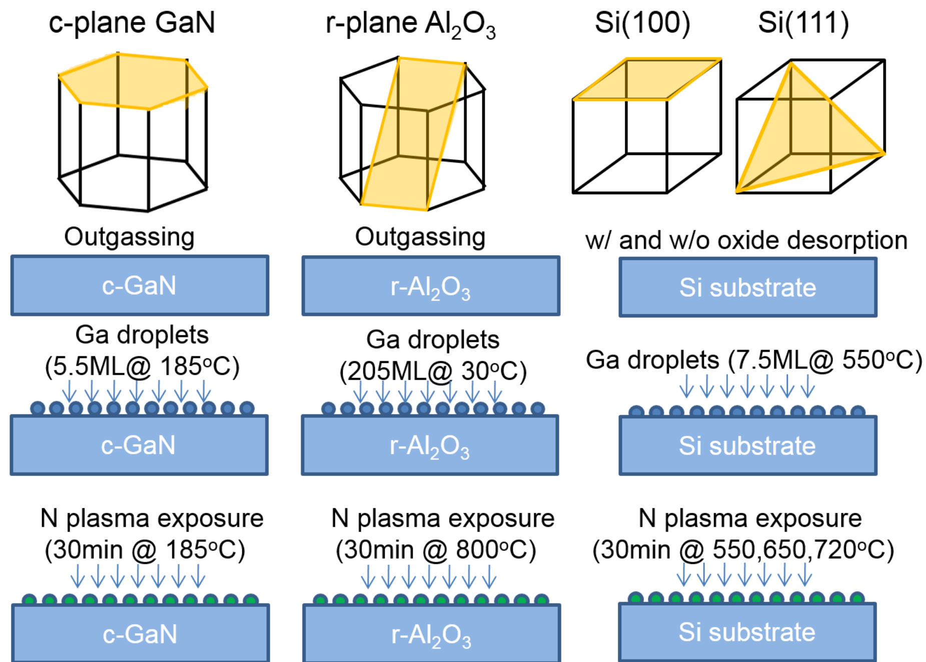


Fig. 4.2 (left) Schematic GaN DE growth procedure for c-GaN substrate: 1) sample outgassing at 800°C for 10min in the MBE chamber, 2) Ga droplet formation at 185°C with 0.5ML/s for 10sec, 3) nitridation with 350W 1sccm N plasma at 185°C for 30min, (middle) Schematic GaN DE growth procedure for r-$Al_2O_3$ substrate: 1) sample outgassing at 800°C for 10min in the MBE chamber, 2) Ga droplet formation at 30°C with 0.68ML/s for 5min, 3) nitridation with 350W 1sccm N plasma at 800°C for 30min, (right) Schematic GaN DE growth procedure for Si substrate: 1) thermal oxide desorption at 900°C for 10min in the MBE chamber, 2) Ga droplet formation at 550°C with 0.75ML/s for 10sec, 3) nitridation with 350W 1sccm N plasma at 550, 650 and 720°C for 30min

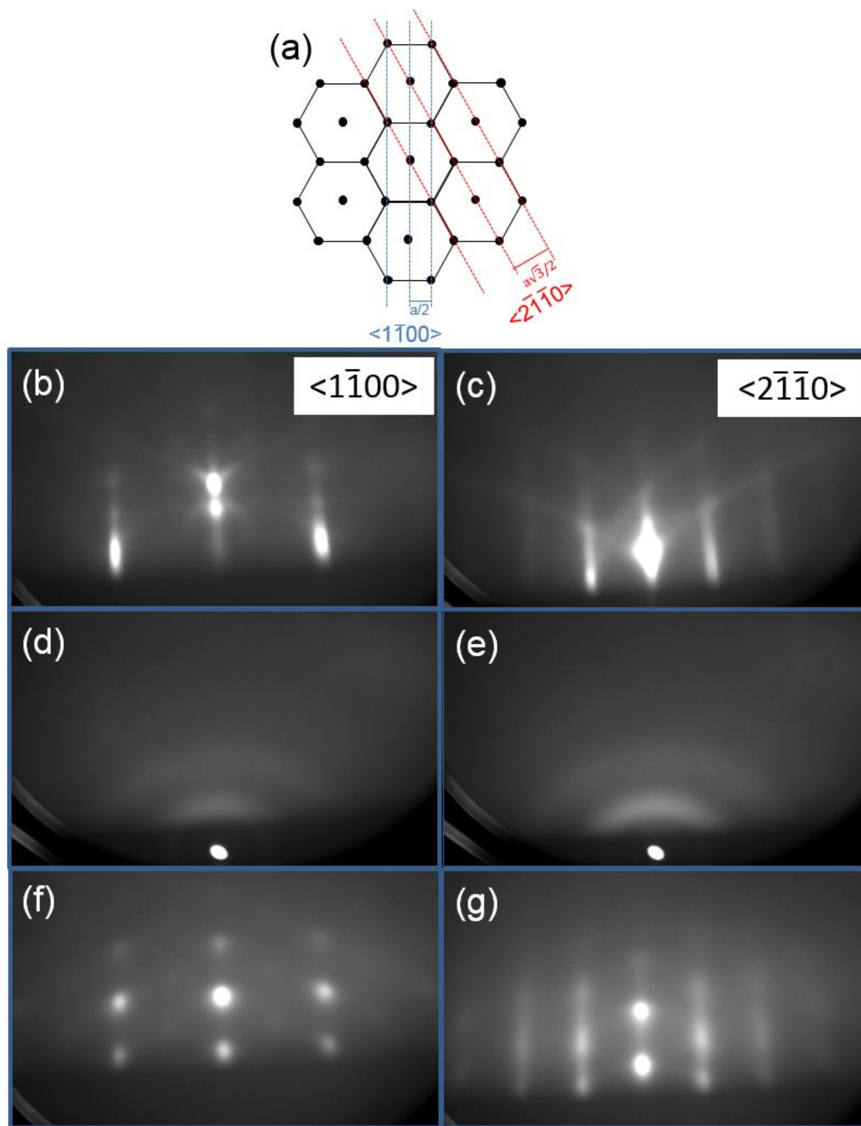


Fig. 4.3 (a) Schematic atomic structure of WZ c-plane GaN, RHEED patterns collected during outgassing along (b) <1100> axis, (c) <2110> axis, during Ga droplet formation along (d) <1100> axis, (c) <2110> axis, and during nitridation along (f) <1100> axis, (g) <2110> axis.

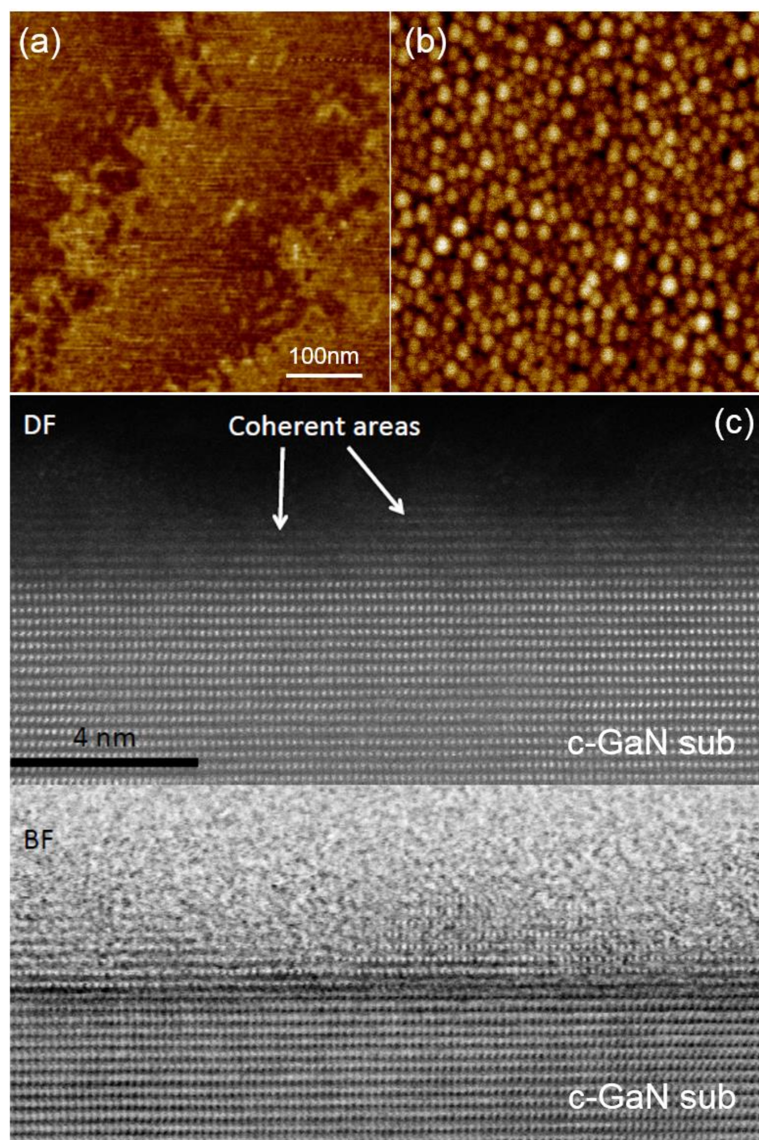


Fig. 4.4 (a) AFM image of c-plane GaN surface, (b) AMF image of GaN QDs on c-GaN after nitridation, (c) Dark field (top) and Bright field (bottom) HRTEM images of coherent WZ GaN QDs grown on c-GaN.

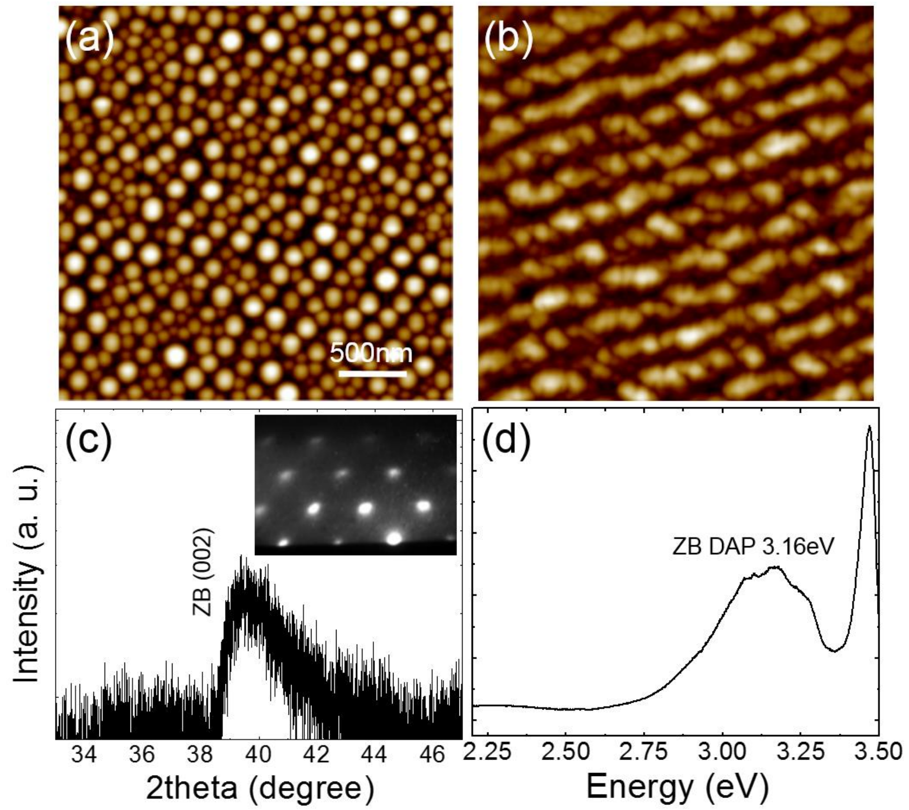


Fig. 4.5 (a) AFM image of 205ML Ga droplets on r-$Al_2O_3$, (b) AMF image of GaN QDs on r-$Al_2O_3$ after nitridation, (c) GIXRD data with ZB GaN (002) peak at 2theta of 40$^o$, (d) 10K PL data with GaN ZB band edge emission peak at 3.16eV.

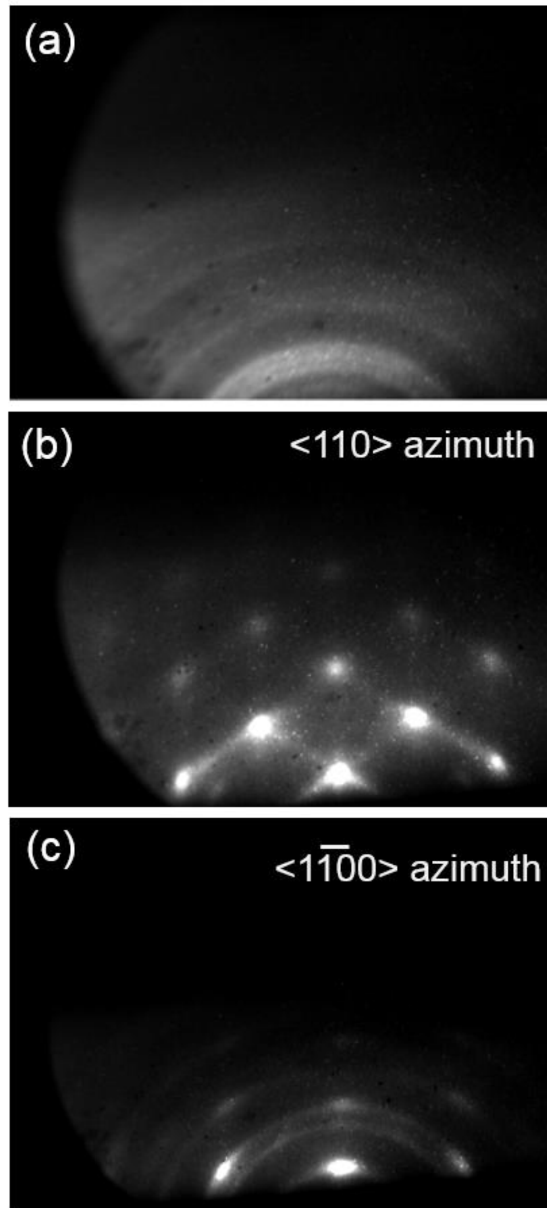


Fig. 4.6 RHEED patterns taken during nitridation steps. (a) concentric ring patterns suggesting polycrystalline GaN grown on Si (001) without thermal oxide desorption. (b) cubic spotty patterns suggesting ZB GaN grown on Si (001) with thermal oxide desorption. (c) hexagonal spotty patterns suggesting WZ GaN grown on Si (111) with thermal oxide desorption.

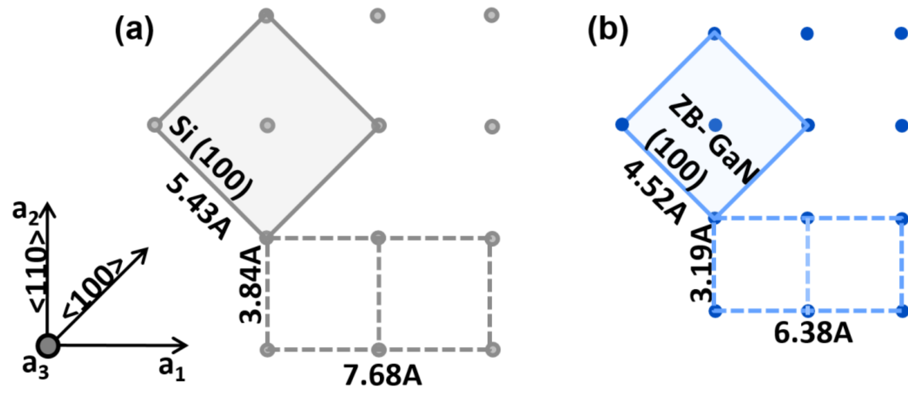


Fig. 4.7 Schematic atomic structure of (a) Si (001) and (b) GaN (001) along <100> axis and <110> axis. The spheres represent the atoms at the first layer of Si (001) and GaN (001) planes with the lattice parameters of 0.543nm for Si and 0.452nm for GaN.

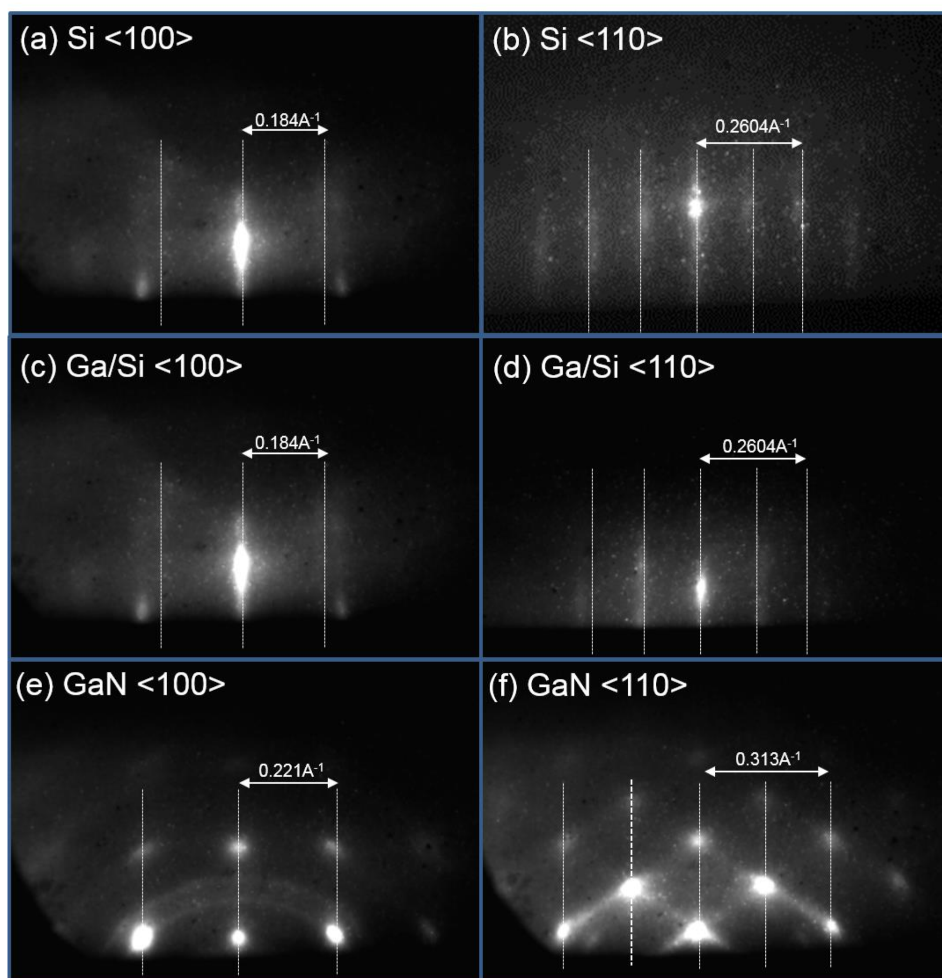


Fig. 4.8 RHEED patterns of the sample grown on thermally cleaned Si (001), collected during (a) Si surface along Si<100> axis, (b) Si surface along Si<110>, (c) 7.5ML Ga droplet deposition along Si<100> axis, (d) 7.5ML Ga droplet deposition on along Si<100> axis, (e) nitridation on along GaN <100> axis, and (f) nitridation on along GaN <110> axis.

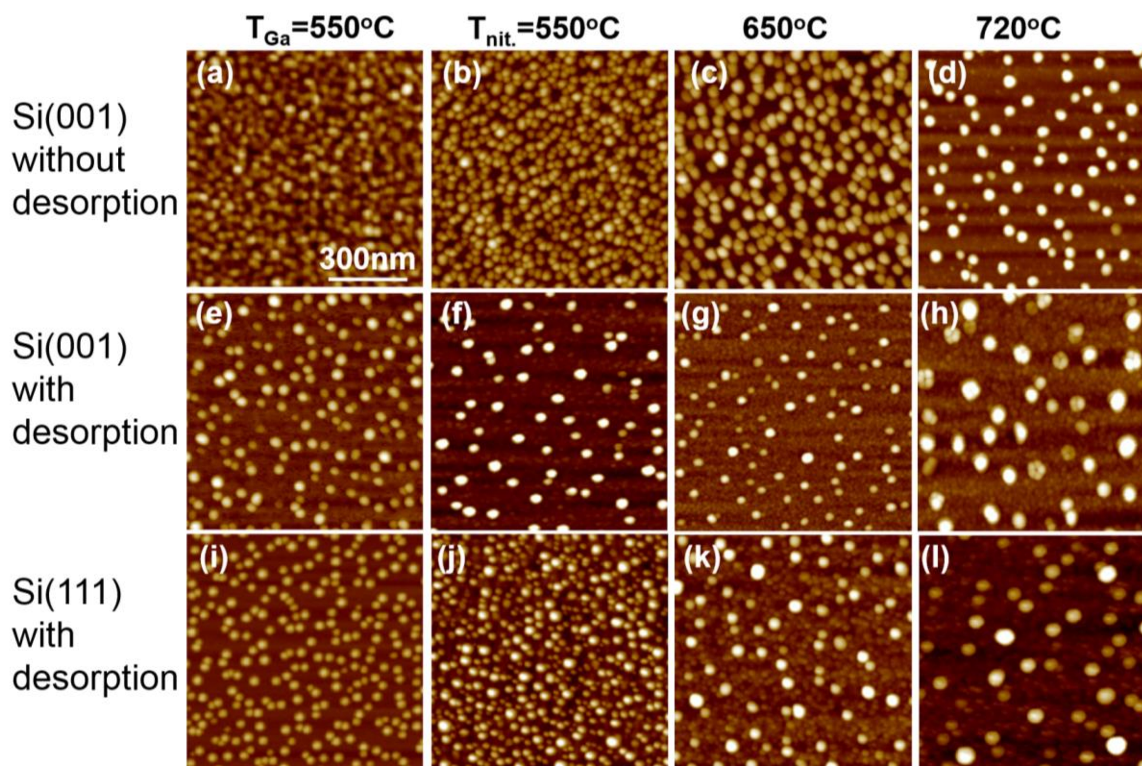


Fig. 4.9 AFM images of (a), (e), and (i) for Ga droplets on Si, and (b)-(d), (f)-(h), and (j)-(l) for Ga N QDs on Si, (a) $T_{Ga}$=550°C, (b) $T_{nit}$=550°C, (c) 650°C, (d) 720°C for Si (001) without oxide desorption, (e) $T_{Ga}$=550°C, (f) $T_{nit}$=550°C, (g) 650°C, (h) 720°C for Si (001) with oxide desorption, and (i) $T_{Ga}$=550°C, (j) $T_{nit}$=550°C, (k) 650°C, (l) 720°C for Si (111) with oxide desorption.

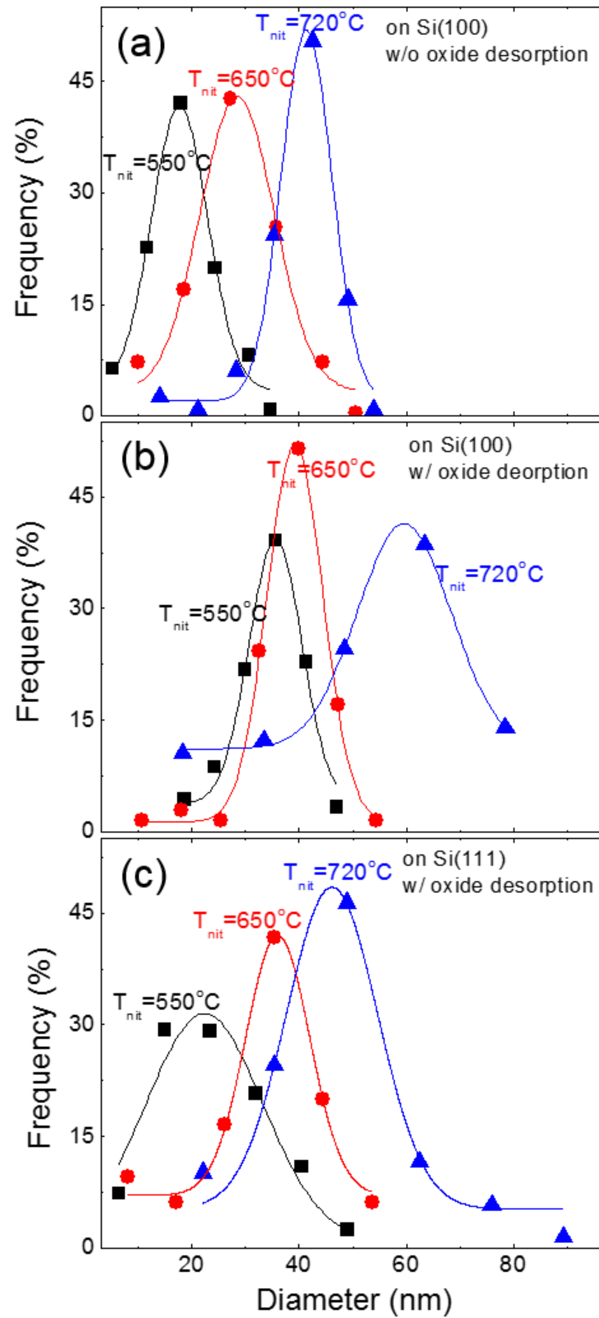


Fig. 4.10 The corresponding GaN QD size distributions (a) GaN QDs grown on Si (001) without oxide desorption from Fig. 4.6(a)-(c), (b) GaN QDs grown on Si (001) with oxide desorption from Fig. 4.6(d)-(g), and (c) GaN QDs grown on Si (111) with oxide desorption from Fig. 4.6(h)-(j). The Frequency is the percentage of islands with diameters within a specified range.

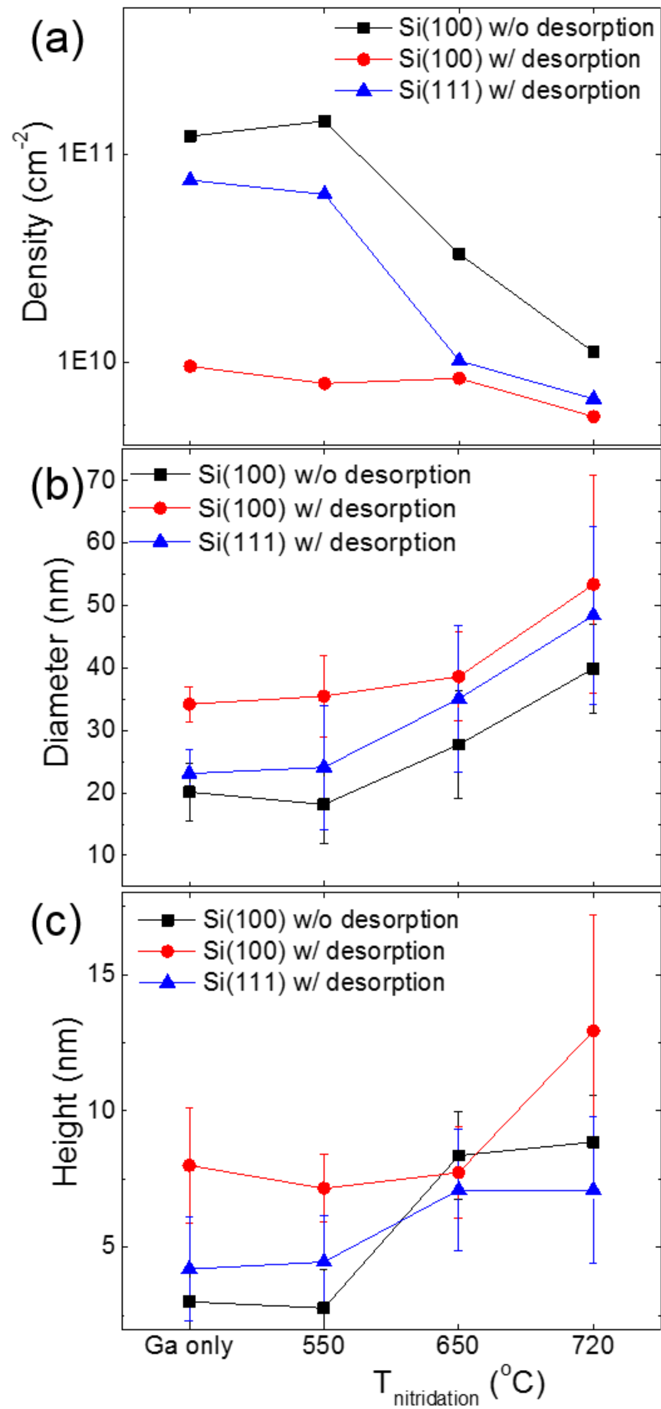


Fig. 4.11 Plots of the (a) density, (b) mean diameter, and (c) mean height of Ga droplets and GaN QDs grown at 550, 650, and 720$^{\circ}$C.

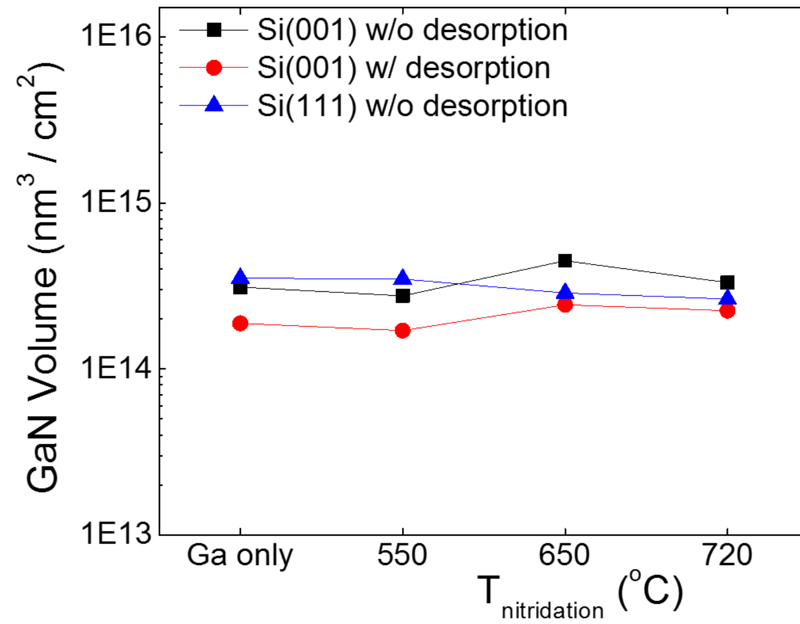


Fig. 4.12 Plots of the GaN QD volume per unit area estimated from QD density, diameter and height. The estimated GaN QD volume values are in the range from 1.5E14 to 4E14 nm$^3$/cm$^2$, independent on nitridation temperature.

## 4.8 References

---

[1] K. Kawasaki, D. Yamazaki, A. Kinoshita, H. Hirayama, K. Tsutsui and Y. Aoyagi, *Appl. Phys. Lett.* **79**, 2243 (2001).

[2] T. Lei, M. Fanciulli, R. J. Molnar, T. D. Moustakas, R. J. Graham and J. Scalon, *Appl. Phys. Lett.* **59**, 944 (1991).

[3] M. Miyamura, K. Tachibana and Y. Arakawa, *Appl. Phys. Lett.* **80**, 3937 (2002).

[4] J. Brown, F. Wu, P. M. Petroff and J. S. Speck, *Appl. Phys. Lett.* **84,** 690 (2004).

[5] T. Kondo, K. Saitoh, Y. Yamamoto, T. Maruyama and S. Naritsuka, *Phys. Stat. Sol. (a)* **203**, 1700 (2006).

[6] T. Schupp, T. Meisch, B. Neuschl, M. Feneberg, K. Thonke, K. Lischka and D. J. As, *J. Crystal Growth*, **312**, 3235 (2010).

[7] S. Hasegawa, S. Nishida, T. Yamashita and H. Asahi, *Thin Solid Films,* **487**, 260 (2005).

[8] H. P. D. Schenk, G. D. Kipshidze, V. B. Lebedev, S. Shokhovets, R. Goldhahn, J. Kraublich, A. Fissel and W. Richter, *J. Crystal Growth*, **201/202**, 359 (1999).

[9] M. Losurdo, P. Capezzuto, G. Bruno, P. R. Lefebvre and E. A. Irene, *J. Vac. Sci. Technol. B* **16**(5), 2665 (1998).

[10] S. Nakamura, M. Senoh, S. Nagahama, N. Iwasa, T. Yamada, T. Matsushita, H. Kiyoku and Y. Sugimoto, *Jpn. J. Appl. Phys.*, **35**, L74 (1996).

[11] P. Kung, C. J. Sun, A. Saxler, H. Ohsato, and M. Razeghi, *J. Appl. Phys.*, **75**(9), 4515 (1994).

[12] M. Suzuki and T. Uenoyama, *J. Appl. Phys.*, **80**(12), 6868 (1996).

[13] K. Domen, K. Horino, A. Kuramata and T. Tanahashi, *Appl. Phys. Lett.*, **71**(14), 1996 (1997).

[14] S. Chichibu, T. Azuhaht, T. Sota and S. Nakamura, *Appl. Phys. Lett.*, **69**(27), 4188 (1997).

[15] T. Takeuchi, C. Wetzel, S. Yamaguchi, H. Sakai, H. Amano and I. Akasaki, *Appl. Phys. Lett.*, **73**(12), 1691 (1998).

[16] D. A. B. Miller, D. S. Chemla, T. C. Damen, A. C. Gossard, W. Wiefmann, T. H. Wood and C. A. Burrus, *Phys. Rev. Lett.*, **53**, 2173 (1984).

[17] H. Masui, S. Nakamura, S. P. DenBaars & K. Mishra, *IEEE Trans. Electron Devices,* **57**, 88 (2009).

[18] J. Simon, N.T. Pelekanos, C. Adelmann, E. Martinez-Guerrero, R. Andre, B. Daudin, L. S. Dang, and H. Mariette, *Phys. Rev. B* **68,** 035312 (2003).

[19] A. W. Wood, X. Weng, Y. Q. Wang, and R. S. Goldman, *Appl. Phys. Lett.* **99**, 093108 (2011).

[20] M. L. Steigerwald, A. P. Alivisators, J. M. Gibson, T. D. Harris, R. Kortan, A. J. Muller, A. M. Thayer, T. M. Duncan, D. C. Douglass, and L. E. Brus, *J. Am. Chem. Soc.* **110**, 3046 (1988).

[21] S. Birudavolu, N. Nuntawong, G. Balakrishnan, Y. C. Xin, S. Huang, S. C. Lee, S. R. J. Brueck, C. P. Hains, and D. L. Huffaker, *Appl. Phys. Lett.* **85**, 2337 (2004).

[22] X. Weng, S. J. Clarke, W. Ye, S. Kumar, A. Daniel, R. Clake, J. Holt, J. Sipowska, A. Francis, V. Rotberg, and R. S. Goldman, *J. Appl. Phys.* **92**, 4012 (2002).

[23] L. Goldstein, F. Glas, J. Y. Marzin, M. N. Charasse, and G. Le Roux, *Appl. Phys. Lett.* **47**, 1099 (1985).

[24] N. Koguchi, S. Takahashi, and T. Chikyow, *J. Cryst. Growth* **111**, 688 (1991).

[25] I. N. Stranski, and L. Krastanow, *Akademie der Wissenschaften Wien* **146** 797 (1938).

[26] M. Miyamura, K. Tachibana, and Y. Arakawa, *Appl. Phys. Lett.* **80**, 3937 (2002).

[27] T. Schupp, T. Meisch, B. Neuschl, M. Feneberg, K. Thonke, K. Lischka and D. J. As, *Phys. Status Solidi (c)*, **8**(5), 1495 (2011).

[28] M. Burger, T. Schupp, K. Lischka and D. S. As, *Phys. Status Solidi (c)*, **9**(5), 1273 (2012).

[29] Y. Tu and J. Tersoff, *Phys. Rev. Lett.* **93**, 216101 (2004).

[30] H. R. Eisenberg and D. Kandel, *Phys. Rev. Lett.* **85**, 1286 (2000).

[31] N. Koguchi, S. Takahashi, and T. Chikyow, *J. Cryst. Growth* **111**, 688 (1991).

[32] C. Heyn, A. Stemmann, A. Schramm, H. Welsch, W. Hansen, and A. Nemcsics, *Phys. Rev. B* **76**, 075317 (2007).

[33] K. Watanabe, N. Koguchi, and Y. Gotoh, Jpn. *J. Appl. Phys*., Part 2 **39**, L79 (2000).

[34] T. Mano, and N. Koguchi, *J. Cryst. Growth* **278**, 108 (2005).

[35] T. Mano, T. Kuroda, S. Sanguinetti, T. Ochiai, T. Tateno, J. Kim, T. Noda, M. Kawabe, K. Sakoda, G. Kido, and N. Koguchi, *Nano Lett.* **5**, 425 (2005).

[36] C. Somaschini, S. Bietti, A. Trampert, U. Jahn, C. Hauswald, H. Riechert, S. Sanguinetti, and L. Geelhaar, *Nano Lett.* **13**, 3607 (2013).

[37] K. Kawasaki, D. Yamazaki, A. Kinoshita, H. Hirayama, K. Tsutsui, and Y. Aoyagi, *Appl. Phys. Lett.* **79**, 2243 (2001).

[38] T. Schupp, T. Meisch, B. Neuschl, M. Feneberg, K. Thonke, K. Lischka and D. J. As, *J. Crystal Growth*, **312**, 3235 (2010).

[39] T. Schupp, T. Meisch, B. Neuschl, M. Feneberg, K. Thonke, K. Lischka and D. J. As, *J. Crystal Growth*, **323**, 286 (2011).

[40] G. P. Dimitrakopulos, E. Kalesaki, J. Kioseoglou, T. Kehagias, A. Lotsari, L. Lahourcade, E. Monroy, I. Hausler, H. Kirmse, W. Neumann, G. Jurczak, T. D. Young, P. Dluzewski, Ph. Komninou and Th. Karakostas, *J. Appl. Phys.*, **108,** 104304 (2010).

[41] M-H. Kim, F. S. Juang, Y. G. Hong, C. W. Tu and S-J. Park, *J. Crystal Growth,* **251**, 465 (2003).

[42] M. Burger, T. Schupp, K. Lischka and D. S. As, *Phys. Status Solidi (c)*, **9**(5), 1273 (2012).

[43] K. K. Lee, W. A. Doolittle, T-H. Kim, A. S. Brown, G. S. May, S. R. Stock, Z. R. Dai & Z. L. Wang, *J. Crystal Growth*, **231**, 8 (2001).

[44] C. Santori, S. Gotzinger, Y. Yamamto, S. Kato, K. Hushino and Y. Arakawa, *Appl. Phys. Lett.*, **87**, 051916 (2005).

[45] D. J. As, *Microelectron J.*, **40**, 204 (2009).

[46] J. Simon, N. T. Pelekanos, C. Adelmann, E. Martinez-Guerrero, R. Andre, B. Daudin, Le Si Dang and H. Mariette, *Phys. Rev. B*, **68** 035312 (2003).

[47] E. Martinez-Guerrero, F. Chabuel, B. Daudin, J. L. Rouviere and H. Mariette, Control *Appl. Phys. Lett.*, **81**, 5117 (2002).

[48] Y. Wang, A. S. Özcan, C. Sanborn, K. F. Ludwig, A. Bhattacharyya, R. Chandrasekaran, T. D. Moustakas, L. Zhou, and D. J. Smith, *J. Appl. Phys.*, **102**, 073522 (2007).

[49] T. Maruyama, H. Otsuboa, T. Kondoa, Y. Yamamotob, and S. Naritsuka, *J. Crystal Growth*, **301**, 486 (2007).

[50] S. Naritsuka, T. Kondoa, H. Otsuboa, K. Saitoha, Y. Yamamotob, and T. Maruyama, *J. Crystal Growth*, **300,** 118 (2007).

[51] T. Kondo, K. Saitoh, Y. Yamamoto, T. Maruyama, and S. Naritsuka, *Phys. Status Solidi (a)*, **203**, 1700 (2006).

[52] M. Burger, T. Schupp, K. Lischka and D. S. As, *Phys. Status Solidi (c)*, **9**(5), 1273 (2012).

[53] P.C. Wu, Ph. D. Thesis, Duke University, 2009

# Chapter 5

# Formation and Optical Properties of Zincblende-Wurtzite GaN Films and Nanowires

## 5.1 Overview

In this chapter, we investigate the nucleation, transformation, and optical properties of GaN nanostructures induced by Ga pre-deposition, followed by GaN epitaxy on Si (001). We demonstrate, for the first time, a growth process consisting of pre-deposition at high Ga flux, followed by GaN growth at low Ga flux, thereby resulting in GaN nanowire (NW) ensembles with a significant zinc-blende (ZB) content. Gallium pre-deposition with a high Ga flux, without nitrogen enables Ga saturation of the Si surface, without the $SiN_x$ interlayer formation. Subsequent GaN film or NW growth leads to the formation of the mixed phase of ZB and wurtzite (WZ). We discuss the role of the N-free Ga pre-deposition on ZB GaN nucleation and growth. We examine the optical properties of the films and NWs, presenting photoluminescence (PL) spectra consisting of the GaN ZB donor-acceptor-pair (DAP) emission for films, as well as the emissions related to ZB and WZ DAP and excitonic transitions for NWs.

## 5.2 Background

GaN is a III-V direct band gap semiconductor with enormous potential for optoelectronic device application from the blue to the near ultraviolet wavelengths.[1,2,3] In addition, GaN on Si (001) is a promising candidate for high efficiency light emitters compatible with well-established conventional CMOS technology.[1,4] GaN-based NW structures are the subject of intense research for solid-state lighting.[1,5,6] However, the wurtzite (WZ) form of GaN is the thermodynamically stable phase.[7] For WZ GaN, the built-in piezoelectric and spontaneous polarization induce a quantum confined Stark effect, leading to a reduced recombination probability of electrons and holes and consequently limit the performance of optoelectronic devices.[8,9] Thus, interest in polarization-free zincblende (ZB) GaN is rapidly increasing.[10,11] To date, GaN NWs and films have been grown in WZ form on Si(001),[1,12,13,14] Si(111),[15,16,17] and c-$Al_2O_3$,[18] $SiO_2$,[19,20] and GaAs(111).[21] For ZB GaN films, it has been demonstrated on GaAs(001),[9,22] Si(001),[11] and 3C-SiC.[23,24] However, to our knowledge, there has not yet been a report of ZB GaN NWs on any substrates, regardless of growth methods.

Typically, on Si (001) substrates, WZ GaN NWs are grown under N-rich conditions,[1,5,6] and GaN films are grown in either ZB[11] or WZ[2] under Ga-rich conditions. Although the formation of WZ NWs and films is considered to be related to the formation of $SiN_x$ interlayer,[1,5,6] a predictive method to control $SiN_x$ interlayer formation has yet to be established. Here, we demonstrate the growth of WZ NW vs. ZB-WZ mixed film and NW growth via controlling $SiN_x$ interlayer formation, using a two-step molecular beam epitaxy (MBE) growth method, consisting of Ga pre-deposition followed by GaN growth

directly on Si (001), all in the absence of a foreign metal catalyst. We discuss the influence of the Ga flux on the structural and optical properties of GaN nanostructures. For the lowest Ga flux, GaN grows as WZ NWs. As the Ga flux is increased, ZB-WZ GaN film growth is observed. Further increases in Ga flux lead to a saturation of the growth rate, mainly due to the N-limited film growth process. Finally, we demonstrate, for the first time, a growth process consisting of pre-deposition at high Ga flux, followed by GaN growth at low Ga flux, thereby resulting in GaN NW ensembles with a significant ZB content.

### 5.3 Experimental Details

For these studies, GaN films and NWs were grown on Si (001) substrates via MBE, using solid Ga and an $N_2$ rf plasma source. Si (001) substrates were chemically cleaned with 5% HF solution to remove native silicon oxides in a fume hood. Following HF cleaning, the substrates were transferred to the MBE chamber for GaN growth. The surface reconstruction was monitored *in situ* with an 18 keV reflection high energy electron diffraction (RHEED) source. The substrates were heated to 880 °C for 10 minutes to remove remaining silicon oxides, at which point a streaky (1×1) RHEED pattern transformed to a streaky (2×1) RHEED pattern, suggesting oxide-free Si (2×1) surface reconstruction. Each sample contained GaN grown at 780 - 860°C using a two-step growth method of N-free Ga pre-deposition for 3 min followed by GaN growth for 3 hr, with various Ga beam-equivalent pressures (BEPs) ranging from $1.0\times10^{-8}$ to $1.5\times10^{-7}$ Torr at a fixed N plasma flux of $1.0\times10^{-6}$ Torr, monitored by the partial pressure of 14 amu determined with a residual gas analyzer in the MBE chamber. For the Ga pre-deposition

step, the N plasma was controlled by a gate valve to prevent the Si surface from nitridation. Following GaN growth, the GaN morphology was examined using an FEI Nova 200 Nanolab scanning electron microscopy (SEM). The crystallinity of GaN was determined using x-ray diffraction (XRD), conducted with a 12 kW Rigaku rotating anode source (Cu target and graphite monochromator) at an incident angle ($\theta_i$) ranging from 1 to 8° for low-incident-beam-angle diffraction (LIBAD) method.[25] Spatially-resolved PL measurements were performed on samples mounted in a liquid-He flow cryostat operating at 10 K, using a Ti-Sapphire laser with 267 nm excitation wavelength, incident laser power of 0.38 mW, and a 5 μm-diameter beam spot. The PL measurements were done by Adam Katcher in Prof. Deng's research group.

### 5.4 Formtion of Zincblende-Wurtzite GaN Films and Nanowires

To examine the dependence of the GaN morphology on Ga flux and growth temperature ($T_{growth}$), sets of GaN samples were grown at various Ga BEPs of $0.1\times10^{-7}$ - $1.5\times10^{-7}$ Torr, with $T_{growth}$ varying from 780°C to 860°C. The GaN morphologies are summarized in the plots of $T_{growth}$ and growth rate vs. Ga BEP in Fig. 5.1 (a), where red dots (black squares) denote NW (film). In the regime of Ga BEP $<0.3\times10^{-7}$ Torr and $T_{growth}$ <800°C, GaN morphology consists of NWs. At higher Ga BEP and $T_{growth}$, GaN grows as films.

Figure 5.1 (b) presents the Ga BEP dependence of the GaN growth rate at a $T_{growth}$ of 800°C, with insets which illustrate the growth of NWs and film. The growth rate increases with increasing Ga BEP until ~$0.9\times10^{-7}$ Torr, and saturates at the Ga BEP

exceeding $0.9\times10^{-7}$ Torr. For the Ga BEP $<0.3\times10^{-7}$ Torr regime, GaN grows in NWs with the lowest growth rate of ~1.1 nm/min. For the Ga BEP of $0.3\text{-}1.0\times10^{-7}$ Torr regime, the morphology transition from GaN NWs to films is observed, with the increase of growth rate from 1.1 to 1.5 nm/min. For the Ga BEP $>1.0\times10^{-7}$ Torr regime, the saturated growth rate of GaN films is observed. Since a fixed N plasma flux of $1.0\times10^{-6}$ Torr is applied to all the growths, GaN grows in NWs (films) at the N/Ga flux ratio above 33 (below 13). In the NW growth regime where the N/Ga flux ratios are above 33, the growth is under N-rich conditions, limited by Ga flux. Thus, the growth rate is increasing with Ga BEP. On the other hand, in the film growth regime where the N/Ga flux ratios are below 13, the growth is under Ga-rich conditions, limited by N flux of $1.0\times10^{-6}$ Torr, leading to the saturation of the growth rate.

Now we discuss mechanisms for GaN growth in the NW and film regimes. Figure 5.2 (a) presents an illustration of GaN growth at 800°C with N/Ga flux ratio=33. Prior to GaN growth, the clean Si surface is exposed to a Ga BEP of $0.3\times10^{-7}$ Torr for 3 min, followed by GaN growth with the same Ga BEP and N flux of $1.0\times10^{-6}$ Torr for 3 hr. During the Ga pre-deposition step, streaky RHEED patterns of (1×1) Si surface in the $[110]_{Si(001)}$ azimuth were observed, suggesting that the Si substrate is not saturated with Ga, likely due to Ga desorption, as shown in Fig. 5.2 (b). During the GaN growth step, broken ring RHEED patterns were observed in the $[1100]_{WZ\text{-}GaN}$ azimuth, suggesting the vertical growth of WZ GaN NWs,[17] as shown in Fig. 5.2 (c). The GaN morphology and crystal structure were examined using SEM and XRD. Figure 5.2 (d) shows the XRD scan, with the tilted SEM image as an inset. As shown in the inset, the GaN morphology consists of vertically-oriented NWs with a height of 180±10nm and diameter of 20±2nm.

To explain the evolution of GaN NW morphology, we consider the Ehrlich-Schwoebel barrier for diffusion down steps.[26,27] The initial Ga islands formed on the Si surface are spatially arranged with an island separation which is greater than the critical island size, resulting in the nucleation on top of the islands instead of the coalescence of islands. Ga adatoms diffuse along the non-polar planes and incorporate on the polar-planes because of the higher sticking coefficient on the polar planes than the non-polar planes.[28] Since the c-plane of GaN is a polar plane, the GaN growth is enhanced along the c-direction, exhibiting a WZ structure. The XRD data shows a peak at $2\theta = 34.7°$, corresponding to WZ-GaN (002) planes, revealing the presence of WZ-GaN aligned along its c-direction atop the Si substrate. Presumably, the formation of $SiN_x$ before GaN growth impedes the epitaxial growth of cubic GaN on Si(001).[1,6,13,17,29]

For the growth with N/Ga flux ratio<13, Ga BEP of $0.9\times10^{-7}$ Torr was applied for each pre-deposition Ga and GaN growth step. Figure 5.3 (a) presents an illustration for GaN growth at 800°C with N/Ga flux ratio<13. Prior to GaN growth, the clean Si surface is exposed to a Ga BEP of $0.9\times10^{-7}$ Torr for 3 min, followed by GaN growth with the same Ga BEP and N flux of $1.0\times10^{-6}$ Torr for 3 hr. As shown in Fig. 5.3 (b), during the Ga pre-deposition step, diffuse RHEED patterns were observed, suggesting that the Si surface is saturated with the exposed Ga. Figure 5.3 (c) shows the RHEED patterns taken during the GaN growth step after 23 min (top) and 2 hr (bottom). As shown in Fig. 5.3 (c, top), spotty RHEED patterns, corresponding to the $[110]_{ZB\text{-}GaN}$ azimuth,[11,30] are observed.

Following 2hr of GaN growth, spotty RHEED patterns in the $[1100]_{WZ\text{-}GaN}$ azimuth, shown in Fig. 5.3 (c), bottom were observed,[31] suggesting a rough WZ surface. It is likely that the phase transition from ZB to WZ occurs between 23 min and 2 hours of growth.

The transition may be started from (111) planes of ZB phase to the basal planes of WZ phase. Figure 5.3 (d) shows the cross-sectional SEM image of the 280nm-thick GaN film with a rough surface. The $\theta/2\theta$ XRD and GIXRD scans were shown in Fig. 5.4 (a) and (b). The XRD data shows peaks at $2\theta = 34.7°$, $37.1°$, and $40.0°$, corresponding to WZ-GaN (002), WZ-GaN (101), and ZB-GaN (200) planes, respectively, revealing the presence of mixed phase of WZ and ZB.

To estimate the depth dependence of the phase transition, we performed LIBAD varying $\theta_i$ ranging from 1° to 8°. The resulting GIXRD scans at $\theta_i = 1°$ (blue), 5° (red), and 8°(black) are shown in Fig. 5.4 (b). For $\theta_i = 1°$, only WZ diffraction peaks are observed, revealing that the top of the NW consists of the WZ phase. When $\theta_i$ exceeds 5°, the ZB diffraction peak at $2\theta = 40.0°$ is observed, suggesting that the ZB phase is buried in the film. The refraction-corrected information depths were calculated with the GaN attenuation coefficient of 429cm$^{-1}$ (CuK$\alpha$ $\lambda$=0.154nm).[25, 32] The estimated information depths below the surface for $\theta_i = 1°$, 5°, and 8°are 131nm, 145nm, and 148nm, respectively, indicating that the GaN film grown at N/Ga flux ratio=13 consists of a layered structure of ZB phase from the Si/GaN interface to the middle of the film and WZ phase atop the ZB phase. Therefore, the high flux of Ga in the pre-deposition step is likely enabling the Ga saturation of the Si surface, hindering the formation of a $SiN_x$ surface layer, thereby allowing the epitaxial growth of ZB phase on Si(001).

To grow ZB GaN NWs on Si(001), we utilized a new process consisting of pre-deposition at high Ga flux to saturate the Si surface, followed by GaN growth at low Ga flux to grow NWs. Figure 5.5 (a) presents an illustration of GaN growths with the two Ga fluxes. First, the clean Si surface was exposed for 3 minutes to a Ga BEP of $0.9\times10^{-7}$ Torr,

followed by 3 hrs of GaN growth with a Ga BEP of $0.3\times10^{-7}$ Torr and N flux of $1.0\times10^{-6}$ Torr. As shown in Fig. 5.5 (b), during the Ga pre-deposition step, diffuse RHEED patterns were observed, similar to those shown in Fig. 5.3 (b). Figure 5.5 (c) shows the RHEED patterns collected during the GaN growth step following 10 min (top) and 2 hr (bottom) of growth. As shown in Fig. 5.5 (c) top, a spotty and broken ring RHEED pattern is observed, corresponding to the $[110]_{ZB\text{-}GaN}$ azimuth. After 2hr of GaN growth, broken ring RHEED patterns in the $[1100]_{WZ\text{-}GaN}$ azimuth are observed, shown in Fig. 5.5 (c) bottom, suggesting a phase transition from ZB to WZ has occurred. Figure 5.5 (d) shows a tilted SEM image of the 190±9nm-thick GaN NWs. The θ/2θ XRD and LIBAD scans were shown in Fig. 5.6 (a) and (b). The XRD data shows peaks at 2θ = 33.1°, 34.7°, 37.1°, and 40.0°, corresponding to the WZ-GaN (100), WZ-GaN (002), WZ-GaN (101), and ZB-GaN (200) planes, respectively, revealing the presence of mixed phase of WZ and ZB. To estimate the depth at which the phase transition occurred, we performed LIBAD with varying $\theta_i$ ranging from 1° to 8°. The resulting GIXRD scans at $\theta_i$ = 1° (blue), 5° (red), and 8°(black) are shown in Fig. 5.6 (b). For $\theta_i$ = 1°, only WZ diffraction peaks are observed, revealing that the top layer of the GaN NWs consist of the WZ phase. When $\theta_i$ exceeds 5°, the ZB diffraction peak at 2θ = 40.0° is observed, suggesting that ZB phase exists near the bottom of the GaN NWs. Since the estimated information depths below the surface for $\theta_i$ = 1°, 5°, and 8°are 131nm, 145nm, and 148nm, respectively, the GaN NWs consist of a layered structure comprised of the ZB phase from the Si/GaN interface to the middle of the NW and WZ phase atop the ZB phase, with a transition at about 150nm in thickness.

### 5.5 Optical Properties of Zincblende-Wurtzite GaN Films and Nanowires

Figure 5.7 shows the PL spectra at 10K for a WZ NW (blue line), ZB-WZ mixed film (black line), and ZB-WZ mixed NW (green line). For the WZ NW, the spectrum is dominated by an emission at 3.47 eV corresponding to excitonic transitions of WZ GaN.[6,33,34,35] Deep level emissions related to structural defects and impurities and ZB GaN-related emissions,[36] typically observed around 3.3eV,[37] were not observed. On the other hand, for the ZB-WZ film, the emission at 3.16eV is apparent, which is attributed to donor-acceptor-pair (DAP) transitions in ZB GaN,[38,39,40,41] without the emissions related to WZ GaN, presumably due to the band alignment of ZB and WZ GaN, inducing the capture of electrons in the relatively low ZB conduction band and their recombination with holes in the ZB valence band. For the ZB-WZ mixed NW, four resolved emission peaks at 3.47eV, 3.41eV, 3.32eV, and 3.16eV are observed. The emissions at 3.47 eV and 3.41 eV are attributed to the excitonic transitions[6,30,31,32] and DAP transitions[30,42,43] of WZ GaN, respectively. In addition to the WZ GaN emissions, the emissions related to ZB GaN DAP transitions around 3.3eV[34] and excitonic transitions at 3.16eV[35,36,37,38] are apparent. Figure 5.8 presents a proposed band alignment of ZB and WZ GaN. The heterostructure of ZB and WZ GaN is theoretically expected to exhibit type II band alignment.[44] The type II band structure of the ZB-WZ mixed film may induce the capture of electrons in the relatively low ZB conduction band and their recombination with holes in either WZ or ZB valence band, resulting in the broad PL emission peak centered at 3.16 eV, as shown in Fig. 5.7. On the other hand, the ZB-WZ mixed NWs may have a discontinuous phase of ZB and WZ, resulting in the distinct emission peaks of ZB DAP, ZB $E_g$, WZ DAP, and WZ $E_g$.

### 5.6 Conclusions

In conclusion, we demonstrate the growth of WZ NW, as well as ZB-WZ mixed film and NWs, using a two-step MBE growth method consisting of Ga pre-deposition followed by GaN growth on Si (001). Ga pre-deposition with a high Ga flux, without N, enables Ga saturation of the Si surface, without the $SiN_x$ interlayer formation. Subsequent GaN film or NW growth leads to the formation of the mixed phase of ZB and WZ with a significant ZB content. We discuss the role of the N-free Ga pre-deposition on ZB GaN nucleation and growth. We examine the optical properties of the films and NWs, presenting PL spectra consisting of the GaN ZB DAP emission for films, as well as the emissions related to ZB and WZ DAP and excitonic transitions for NWs. Finally, we demonstrate, for the first time, a growth process consisting of pre-deposition at high Ga flux, followed by GaN growth at low Ga flux, thereby resulting in ZB-WZ GaN NW ensembles.

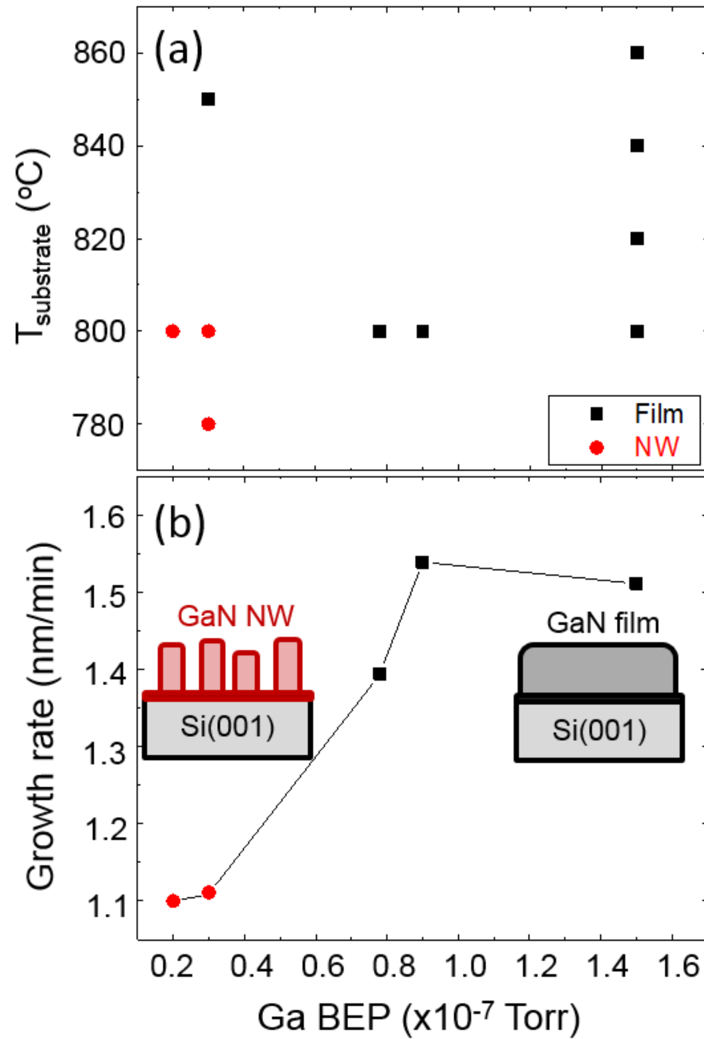


Fig. 5.1 The GaN morphologies plot of (a) $T_{substrate}$ and (b) growth rate vs. Ga BEP, where of red dots (black squares) denote NW (film). The GaN morphology consists in NWs in the regime of Ga BEP $<0.3\times10^{-7}$ Torr and $T_{growth}$ <800°C. At higher Ga BEP and $T_{growth}$, GaN grows in films. The growth rate increases with increasing Ga BEP until $\sim0.9\times10^{-7}$ Torr, and saturates at the Ga BEP exceeding $0.9\times10^{-7}$ Torr.

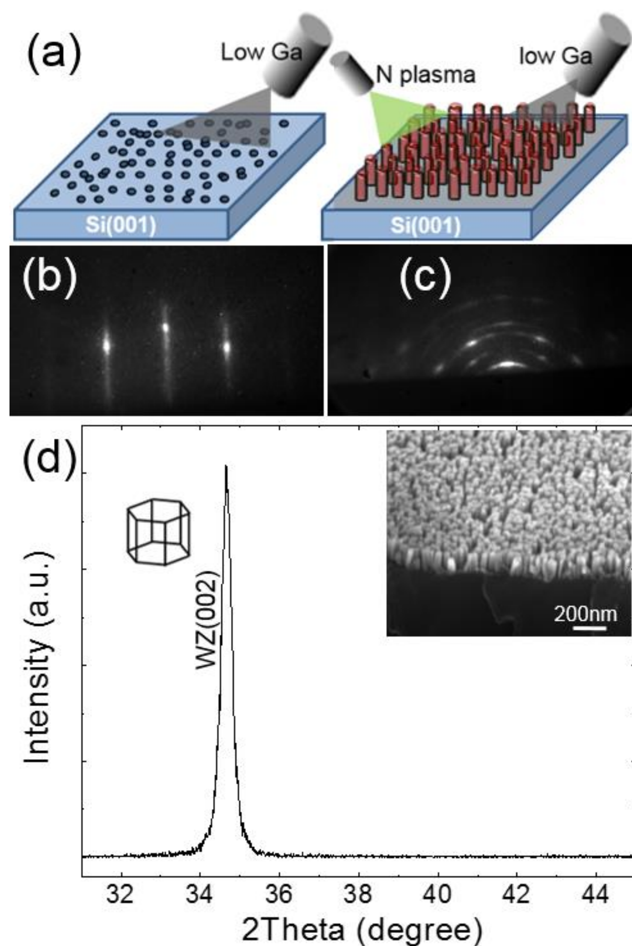


Fig. 5.2 (a) Schematic illustrations of GaN growth at 800°C with N/Ga flux ratio=33. First, the clean Si surface is exposed to a Ga BEP of $0.3\times10^{-7}$ Torr for 3 min, followed by 3hrs GaN growth with the same Ga BEP and a N flux of $1.0\times10^{-6}$ Torr. (b) During the Ga pre-deposition step, streaky RHEED patterns of (1×1) Si surface in the $[110]_{Si(001)}$ azimuth were observed. (c) During the GaN growth step, broken ring RHEED patterns were observed in the $[1100]_{WZ\text{-}GaN}$ azimuth. (d) the XRD scan, with the tilted SEM image as an inset.

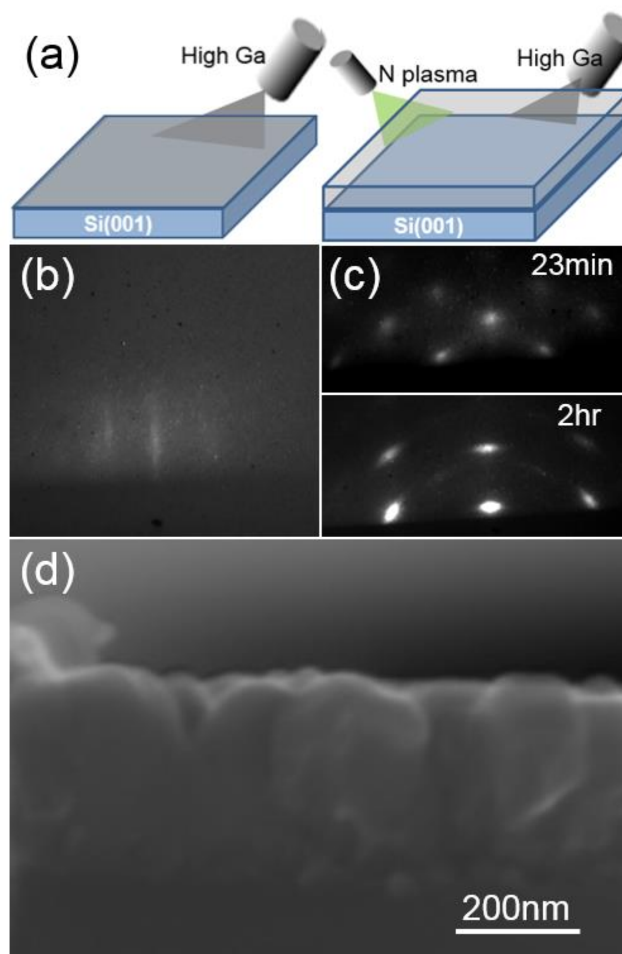


Fig. 5.3 (a) Schematic illustrations of GaN growth at 800°C with N/Ga flux ratio<13. First, the clean Si surface is exposed to a Ga BEP of $0.9\times10^{-7}$ Torr for 3 min, followed by 3hrs GaN growth with the same Ga BEP and a N flux of $1.0\times10^{-6}$ Torr. (b) during the Ga pre-deposition step, diffuse RHEED patterns were observed. (c) RHEED patterns taken during the GaN growth step after 23 min (top) and 2 hr (bottom). (d) cross-sectional SEM image.

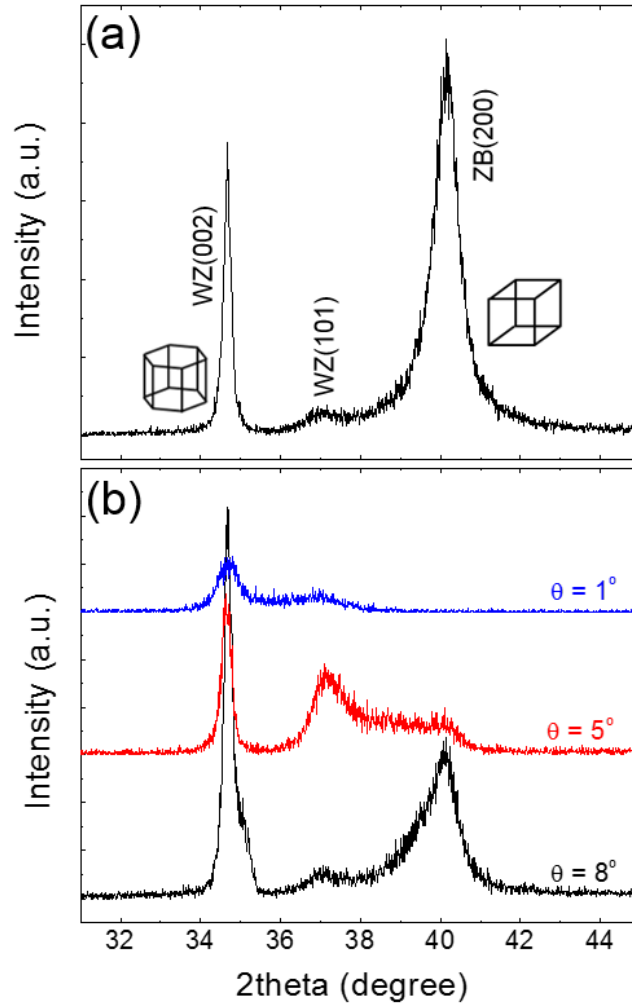


Fig. 5.4 (a) XRD data with peaks at $2\theta = 34.7°$, $37.1°$, and $40.0°$, corresponding to WZ-GaN (002), WZ-GaN (101), and ZB-GaN (200) planes, respectively, revealing the presence of mixed phase of WZ and ZB. (b) LIBAD scans at $\theta_i = 1°$ (blue), 5° (red), and 8°(black). For $\theta_i = 1°$, only WZ diffraction peaks are observed, revealing that the top of GaN consists of WZ phase. With increasing $\theta_i$ exceeding 5°, the ZB diffraction peak at $2\theta = 40.0°$ is observed, suggesting that ZB phase is buried in the film.

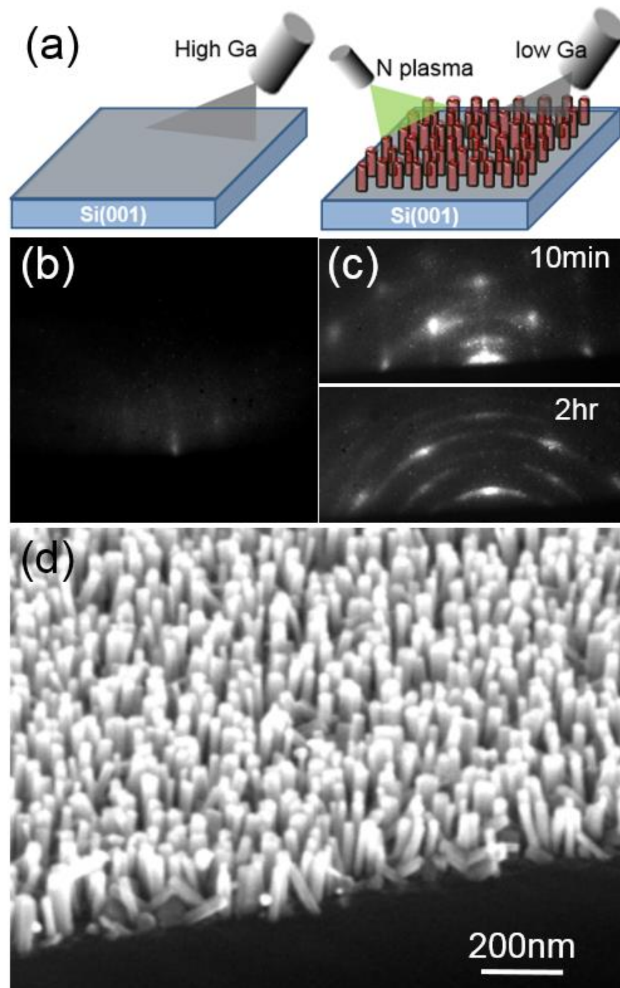


Fig. 5.5 (a) Schematic illustrations of GaN growth at 800°C with high Ga flux during Ga supersaturation, followed by low Ga flux during GaN growth. First, the clean Si surface is exposed to a Ga BEP of $0.9\times10^{-7}$ Torr for 3 min, followed by 3 hrs GaN growth with Ga BEP of $0.3\times10^{-7}$ Torr and N flux of $1.0\times10^{-6}$ Torr. (b) during the Ga pre-deposition step, diffuse RHEED patterns were observed. (c) RHEED patterns taken during the GaN growth step after 10 min (top) and 2 hr (bottom). (d) tilted SEM image, showing formation of 188±9nm-thick GaN NWs.

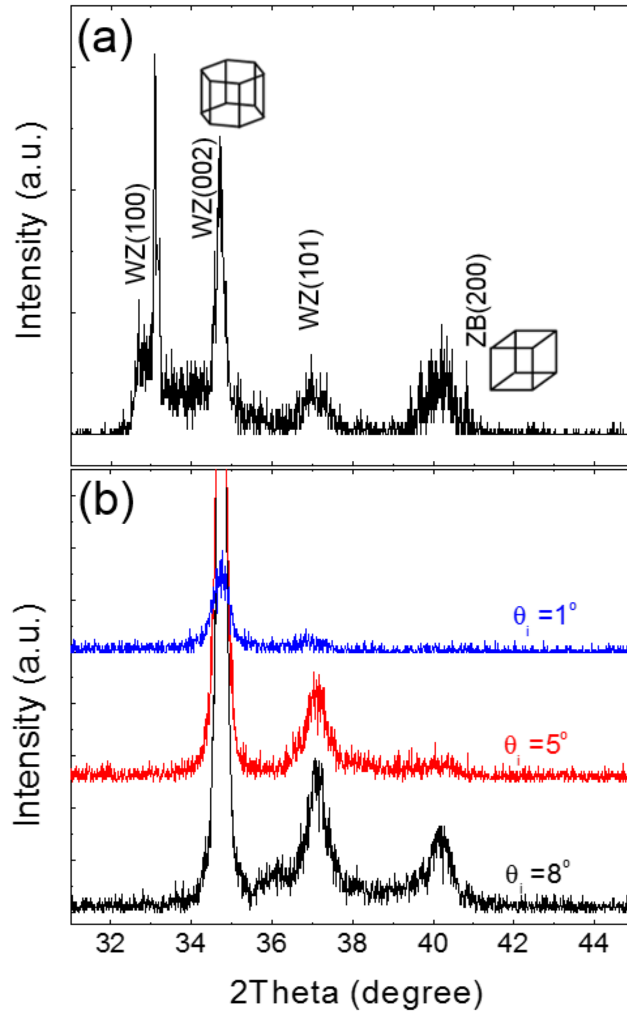


Fig. 5.6 (a) XRD data with peaks at $2\theta = 33.1°$, $34.7°$, $37.1°$, and $40.0°$, corresponding to WZ-GaN (100), WZ-GaN (002), WZ-GaN (101), and ZB-GaN (200) planes, respectively, revealing the presence of mixed phase of WZ and ZB. (b) GIXRD scans at $\theta_i = 1°$ (blue), $5°$ (red), and $8°$(black). For $\theta_i = 1°$, only WZ diffraction peaks are observed, revealing that the top of GaN consists of WZ phase. With increasing $\theta_i$ exceeding $5°$, the ZB diffraction peak at $2\theta = 40.0°$ is observed, suggesting that ZB-WZ phase transformation occurs at 150nm thickness.

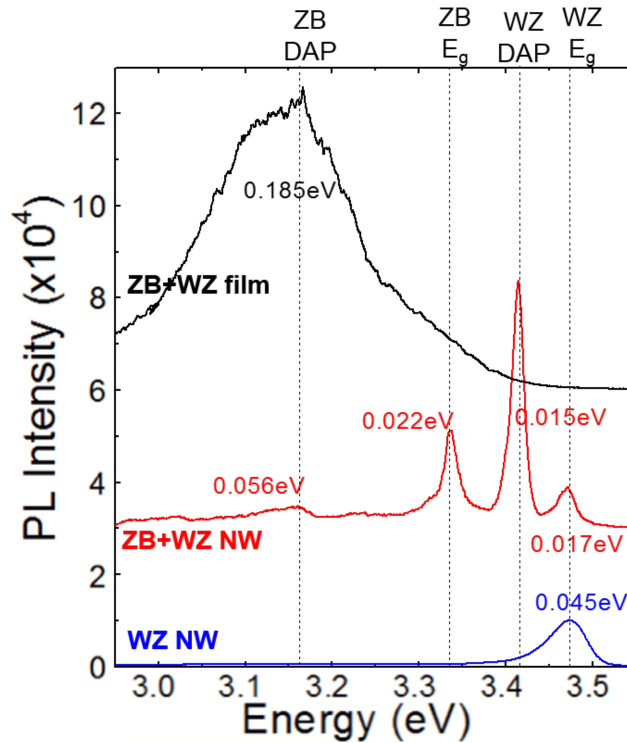


Fig. 5.7 PL spectra at 10K for a WZ NW (blue line), ZB-WZ mixed film (black line), and ZB-WZ mixed NW (green line). For the WZ NW, the spectrum is dominated by an emission at 3.47eV corresponding to excitonic transitions of WZ GaN. For the ZB-WZ film, the emission 3.16eV is apparent, which is attributed to donor-acceptor-pair (DAP) transitions of ZB GaN, without the emissions related to WZ GaN. For the ZB-WZ mixed NW, four resolved emission peaks at 3.47eV, 3.41eV, 3.32eV, and 3.16eV are observed. The emissions at 3.47 eV and 3.41 eV are attributed to the excitonic transitions and DAP transitions of WZ GaN, respectively. In addition to the WZ GaN emissions, the emissions related to ZB GaN DAP transitions around 3.3eV and excitonic transitions at 3.16eV are apparent.

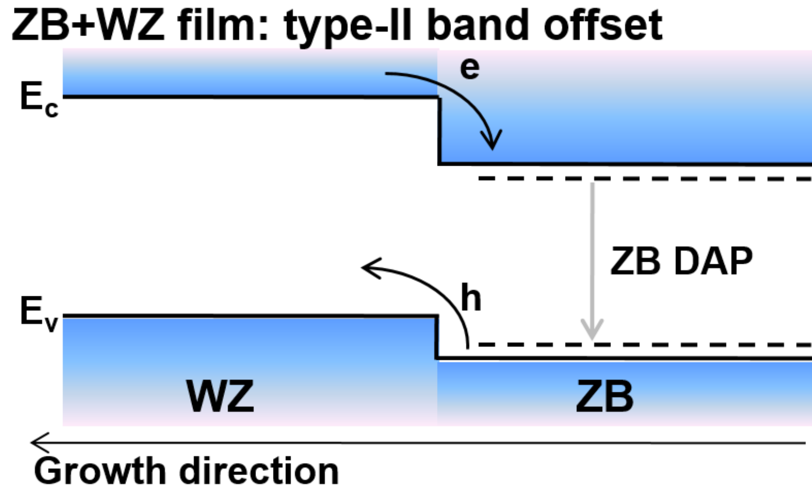


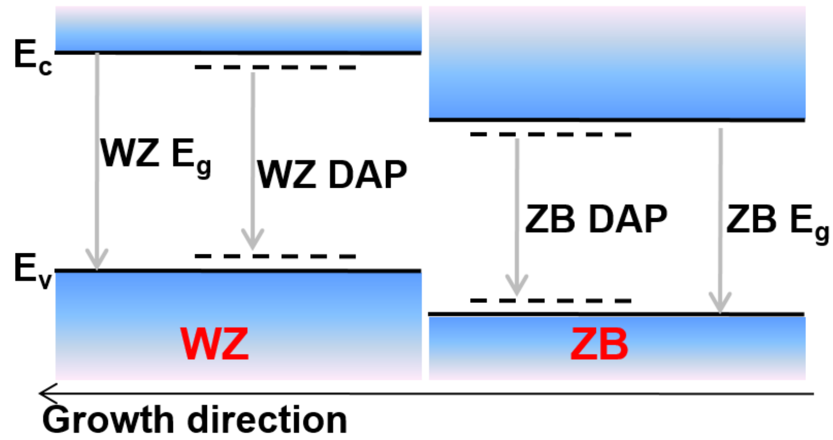


Fig. 5.8 Proposed band alignment of ZB and WZ GaN, inducing the capture of electrons in relatively low ZB conduction band and their recombination with holes in ZB valence band.

**5.7 References**


[1] W. Guo, M. Zhang, A. Banerjee, P. Bhattacharya, *Nano Lett.* **10**, 3355 (2010).

[2] T. N. Bhat, M. K. Rajpalke, B. Roul, M. Kumar, S. B. Krupanidhi, *J. Appl. Phys.* **110**, 093718 (2011).

[3] S. Strite, J. Ruan, Z. Li, A. Salvador, H. Chen, David J. Smith, W. J. Choyke and H. Morkoç, *J. Vac. Sci. Technol. B* **9**(4), 1924 (1991).

[4] S.C. Lee, X.Y. Sun, S.D. Hersee, and S.R.J. Brueck, *J. Cryst. Growth*, **279**, 289 (2005).

[5] J. Borysiuk, Z. R. Zytkiewicz, M. Sobanska, A. Wierzbicka, K. Klosek, K. P. Korona, P. S. Perkowska, and A. Reszka, *Nanotechnology* **25**, 135610 (2014).

[6] L. Cerutti, J. Ristić, S. Fernández-Garrido, E. Calleja, A. Trampert, K. H. Ploog, S. Lazic and J. M. Calleja, *Appl. Phys. Lett.,* **88**, 213114 (2006).

[7] C.-Y. Yeh, Z.W. Lu, S. Froyen, A. Zunger, *Phys. Rev. B* **46**, 10086 (1992).

[8] T. Schupp, T. Meisch, B. Neuschl, M. Feneberg, K. Thonke, K. Lischka, and D. J. As, *J. Crys. Growth* **312**, 3235 (2010).

[9] D. J. As, *Microelectron. J.* **40** 204 (2009).

[10] S. V. Novokiv, C. T. Foxon, and A. J. Kent, *Phys. Status Solidi C* **8**, No5 1439 (2011).

[11] T. Lei, T. D. Moustakas, R. J. Graham, Y. He and S. J. Berkowitz, *J. Appl. Phys.* **71**, 4933 (1992).

[12] W. Guo, A. Banerjee, P. Bhattacharya, and B. S. Ooi, *Appl. Phys. Lett.,* **98**,193102 (2011).

[13] W. Guo, M. Zhang, P. Bhattacharya, and J. Heo. *Nano lett.***11**,1434 (2011).

[14] C. Chèze, L. Geelhaar, A. Trampert and H. Riechert, *Appl. Phys. Lett.,* **97**, 043101 (2010).

[15] R. Calarco, R. J. Meijers, R. K. Debnath, T. Stoica, E. Sutter, and H. Lüth, *Nano lett.* **7**, 2248 (2007).

[16] Y. S. Park, C. M. Park, D. J. Fu, T. W. Kang and J. E. Oh, *Appl. Phys. Lett.,***85**, 5718 (2004).

[17] S. F. Garrido, J. Grandal, E. Calleja, M. A. Sánchez-García and D. López-Romero, *J. Appl. Phys.* **106**, 126102 (2009).

[18] C. Chèze, L. Geelhaar, O. Brandt, W. M. Weber, H. Riechert, S. Münch, R. Rothemund, S. Reitzenstein, A. Forchel, T. Kehagias, P. Komninou, G. P. Dimitrakopulos, and T. Karakostas, *Nano Research*, **3**, 528 (2010).

[19] M. Hiroki, H. Asahi, H. Tampo, K. Asami, and S. Gonda *J. Crystal Growth* **209**, 387 (2000).

[20] G. Nouet, P. Ruterana1, H. Tampo, and H. Asahi, *J. Phys.: Condensed Matter*, **14**, 12697 (2002).

[21] S.V. Novikov, C.R. Staddon, F. Luckert, P.R. Edwards, R.W. Martin, A.J. Kent, C.T. Foxon, *J. Crystal Growth* **350**, 80 (2012).

[22] S.V. Novikov, N.M. Stanton, R.P. Campion, C.T. Foxon, A.J. Kent *J. Crystal Growth* **310**, 3964 (2008).

[23] A. Philippe, C. Bru-Chevallier, M. Vernay, G. Guillot, J. Hübner, B. Daudin, G. Feuillet, *Mater Science and Engin. B*, **59**, 168 (1999).

[24] M. Feneberg, M. Röppischer, C. Cobet, N. Esser, J. Schörmann, T. Schupp, D. J. As, F. Hörich, J. Bläsing, A. Krost, and R. Goldhahn, *Phys. Rev. B* **85**, 155207 (2012).

[25] K. V. Acker, L. D. Buyser, J. P. Celis, and P. V. Houtte, *J. Appl. Cryst.* **27**, 56 (1994).

[26] G. Ehrlich and F.J. Hudda, *J. Chem. Phys.* **44**, 1069 (1966).

[27] R.L. Schwoebel and E.J. Shipsey, *J. Appl. Phys.* **37**, 3682 (1966).

[28] K.A. Bertness, A. Roshko, L.M. Mansfield, T.E. Harvey, and N.A. Sanford, *J. Cryst. Growth*, **310**, 3154 (2008).

[29] L. Yan, S. Jahangir, S. A. Wight, B. Nikoobakht, P. Bhattacharya, and J. M. Millunchick, *Nano Lett.* **15**, 1535 (2015).

[30] H. Okumura, S. Misawa and S. Yoshida, *Appl. Phys. Lett.,***59**(9), 1058 (1991).

[31] Hung-Ying Chen, Hon-Way Lin, Chang-Hong Shen and Shangjr Gwo, *Appl. Phys. Lett.,***89**, 243105 (2006).

[32] D. Simeone, G. Baldinozzi, D. Gosset, S. LeCaer, and J-F. Bérar, *Thin Solid Films*, **530**, 9 (2013).

[33] S. Fischer, G. Steude, D.M. Hofmann, F. Kurth, F. Anders, M. Topf, B.K. Meyer, F. Bertram, M. Schmidt, J. Christen, L. Eckey, J. Holst, A. Hoffmann, B. Mensching, and B. Rauschenbach. *J. Cryst. Growth*, **189/190**, 556 (1998).

[34] M. A. Reshchikov, D. Huang, F. Yun, L. He, H. Morkoç, D. C. Reynolds, S. S. Park and K. Y. Lee, *Appl. Phys. Lett.,* **79**, 3779 (2001).

[35] S. Y. Bae, H. W. Seo, J. Park, H. Yang, H. Kim, and S. Kim *Appl. Phys. Lett.,* **82**, 4564 (2003).

[36] M.A. Reshchhikov, and H. Morkoc, *J. Appl. Phys.* **15**, 061301 (2005).

[37] M. Godlewski, J. P. Bergman, B. Monemar, U. Rossner, R. Langer, and A. Barski, *Mater. Sci. Eng.*, **B 50**, 113 (1997).

[38] A. Philippe, C. Bru-Chevallier, M. Vernay, G. Guillot, J. Hübner, B. Daudin, and G. Feuillet, *Mater. Sci. Eng. B* **59**, 168 (1999).

[39] S. V. Novikov, C. T. Foxon, and A. J. Kent, *Phys. Status Solidi C* **8**, 1439 (2011).

[40] J. Wu, H. Yaguchi, K. Onabe, R. Ito, and Y. Shiraki, *Appl. Phys. Lett.*, **71**(15), 2067 (1997).

[41] H. Yaguchi, J. Wu, H. Akiyama, M. Baba, K. Onabe, and Y. Shiraki, *Phys. Status Solidi B*, **216**, 237 (1999).

[42] B-C. Chung and M. Gershenzon, *J. Appl. Phys.*, **72**, 651 (1992).

[43] S. Fischer, C. Wetzel, W. Walukiewicz, and E. E. Haller, *MRS. Symp. Proc.* **395**, 571 (1996).

[44] M. Murayama and T. Nakayama, *Phys. Rev. B*, **49**, 4710 (1994).

# Chapter 6

# Summary and Suggestions for Future Work

## 6.1 Summary

In this thesis, we demonstrate, for the first time, the formation of embedded GaAs:Ga nanocomposites and ZB GaN nanostructures. We utilize Ga droplets as a near-IR plasmonic metal NP and a seed for droplet epitaxy of ZB GaN nanostructures. Furthermore, we investigate their influence on the structural and optical properties of the embedded GaAs:Ga nanocomposites and the GaN nanostructures including QDs, NWs and films.

In Chapter 3, we examined the formation of embedded Ga NP arrays and their influence on GaAs NBE PL efficiency. Close-packed embedded arrays of $d_{Ga}$=40 and 66 nm were fabricated using off-normal FIB irradiation, followed by MBE overgrowth. We consider the influence of embedded Ga NP arrays on the enhancement in absorption and emission, using FDTD simulations. We identify a regime of NP size and depth where NP-induced EHP generation are enhanced by absorption and LSP-excitation, leading to enhanced NBE emission from GaAs. This approach provides an opportunity to enhance the PL efficiency from a variety of semiconductor heterostructures, using a seamless approach to embed non-noble metals during epitaxy.

In Chapter 4, we investigated the formation of Ga droplets and their conversion to GaN QDs. To obtain polarization-free ZB GaN QDs, we use the DE process with an rf N plasma source. First, we report epitaxial growths of WZ and ZB GaN QDs on c-plane GaN and r-plane $Al_2O_3$ substrate. In addition, by varying the surface conditions of Si substrates, GaN QDs grown on Si (100) without oxide desorption, Si (100) with oxide desorption, and Si (111) with oxide desorption show polycrystalline, ZB, and WZ structures, respectively. We first demonstrate the nucleation and coalescence of ZB GaN QDs on Si (001). For droplet deposition and nitridation temperatures both at 550$^{\circ}$C, we observe a one-to-one conversion of Ga droplets to GaN QDs. Increasing the nitridation temperature to 650$^{\circ}$C and 720$^{\circ}$C induces a Ga droplet coalescence during nitridation.

In Chapter 5, we demonstrated the growth of WZ NW, ZB-WZ mixed film, and NW growth via controlling $SiN_x$ interlayer formation, using a two-step MBE growth method of Ga pre-deposition followed by GaN growth directly on Si (001). A high flux during N-free Ga pre-deposition saturates Si surfaces, hindering the $SiN_x$ interlayer formation. Subsequent GaN film or nanowire (NW) growth leads to the formation of the mixed phase of zincblende (ZB) and wurtzite (WZ) with a significant ZB content at the base. Finally, we discovered a growth process consisting of pre-deposition at high Ga flux, followed by GaN growth at low Ga flux, thereby demonstrating, for the first time, GaN NW ensembles with a significant ZB content.

## 6.2 Suggestions for Future Work

### 6.2.1 In Nanoparticles for Plasmonics

As described in Chapter 3, silver and gold are the most often employed plasmonic materials due to their ease of synthesis and their strong LSPRs in the visible.[1] Unfortunately, Ag and Au are expensive; they only support LSPRs in the visible-infrared region of the electromagnetic spectrum. Because of these limitations, there is considerable interest in the plasmonic properties of other metals,[2,3] alloys,[4] nonmetals such as graphene,[5,6] and indium−tin oxide (ITO),[7] and a wide range of other materials.[8,9,10] Thus, we focus on indium (In) as an alternative plasmonic material, which supports LSPRs in the UV region.[11,12] The dielectric function of In[13] indicates the potential of In as a low-loss, high-gain deep-UV plasmonic metal. We examined the potential of In quantitatively using FDTD Lumerical for absorptance simulations and ellipsometry experiments. We first prepared In-coated substrates via molecular beam epitaxy (MBE) growths of In droplets on Si (001) substrates. Figure 6.1 (a)-(e) show the SEM images of 3, 4, 5, 6.5, 8 ML In droplets on Si (001), and the corresponding In droplet size distributions. We performed Lumerical FDTD simulations to estimate energy-dependent absorption spectra of In droplets on Si (001) surface, as shown in Fig. 6. 2, in order to compare with the $E_{LSPR}$ values obtained from ellipsometry experiments. Figure 6.3 presents the comparison of the $E_{LSPR}$ collected from ellipsometry experiments and FDTD absorption simulations vs. In droplet diameter. The LSPR energy of In droplets on Si (001) ranges from 5 to 6 eV, showing a redshift with increasing In droplet size. It is evident that In droplets exhibit deep UV LSPR from both experiments and simulations. For the future work regarding plasmonic effect of In nanoparticles, further experiments including fabrications of composite material

systems of deep-UV semiconductor and In metal nanoparticle are necessary to access the potential utility of In nanoparticles as a deep-UV light absorption and emission material.

### 6.2.2 Single Crystalline GaAs Overgrowth

In Chapter 3, we described the formation and optical properties of embedded GaAs:Ga nanocomposites. Since the GaAs overgrown layer has a polycrystalline structure, the emission efficiency is limited by the non-radiative recombination induced by polycrystalline GaAs. First, we tried GaAs overgrowth on FIB-fabricated Ga droplets with high V/III incorporation rate ratio (i.e. V/III), which is a measure of how long it takes a surface to recover after being deprived of an As flux, of 10 at the GaAs growth rate of 0.1 μm/hr. Figure 6.4 shows the SEM images of (a) FIB-Ga NPs on GaAs and (b) GaAs overgrowth with V/III of 10. As shown in Fig. 6.4 (b), the surface protrusions were observed. We performed kinetic Monte-Carlo (KMC) simulations to examine the GaAs growth with V/III=10. The simulation result shows that GaAs does not grow on the GaAs substrates, but the surface of Ga droplets is crystallized in GaAs. Further simulations were performed with various V/III ratios, as shown in Fig. 6.5. It reveals that the optimal V/III ratio is 1.5 to form a single crystalline GaAs layer. To fabricate GaAs:Ga nanocomposites with a single crystalline GaAs overgrown layer, we propose MBE-fabrication of Ga droplets, followed by *in situ* MBE GaAs overgrowth, as shown in Fig. 6.6. Ga droplets are fabricated via Ga exposure on GaAs buffer layer, followed by *in situ* GaAs overgrowth with V/III ratio of 1.5. The RHEED patterns collected during *in situ* GaAs overgrowth on MBE-fabricated Ga droplets exhibit streaky patterns, suggesting that the single crystalline

GaAs layer was grown on MBE-fabricated Ga droplets. Further analysis of optical properties including PL measurements and FDTD simulations is needed.

### 6.2.3 Ga Nanoparticles: Catalyst for Si Nanowire growths

In Chapter 4 and 5, we described Ga droplets as a seed material or a self-catalyst for GaN QDs and NWs MBE growths. In addition, Ga droplets may enable growth of Ge or Si nanowires. Ge nanowires have been previously been grown from Ga droplets following electrochemical liquid-liquid-solid process,[14] involving the electroreduction of dissolved $GeO_2$ (aq) in water at isolated liquid Ga droplets electrodes, as shown in Fig. 6.4. Ge nanowires were electrodeposited on the wafer scale (>10 $cm^2$) using only common glassware and a digital potentiostat. This approach shows epitaxial growth of covalent group IV nanowires is possible from using of Ga droplets. A further work involving a different type of covalent group IV nanowires such as Si and various metallic droplets including In or In/Ga alloys can be performed.

### 6.2.4 Ga/GaN and In/InN Core-shell Quantum Dot Structures

In Chapter 4, we described processes for converting Ga droplets to crystalline GaN QDs. In recent years, metal–semiconductor core-shell nanostructures have attracted tremendous attention,[15,16,17,18] in a variety of areas such as photovoltaic devices,[19,20] chemical sensor[21,22,23] and photocatalysis.[24,25] In particular, composites consisting of metal cores and III-Nitride semiconductor are expected to enhance absorption and emission

properties of III-Nitrides. It has been demonstrates that Ga (In) has a wide range of LSPR wavelength covering near-IR to visible (deep UV). Therefore, we propose a new metal core-semiconductor shell structures consisting of Ga (In) and GaN (InN). It still remains a challenge to develop a facile and effective method to fabricate hybrid core–shell nanomaterials. To control the Ga (In) droplets sizes and positions, it is required to utilize FIB irradiation. We are in progress on the installation of *in situ* FIB source to our MBE system. Figure 6.8 presents the design of the FIB source and chamber modification for the installation. Figure 6.5 presents a schematic illustration of FIB-directed epitaxial core-shell Nanostructures, consisting of 2D array of metal - semiconductor epitaxial core-shell nanostructures with Ga droplet cores and a surrounding GaN.

### 6.2.5 Growth of ZB GaN Nanowires

In Chapter 5, we demonstrate the growth of ZB-WZ mixed GaN NW growth via controlling $SiN_x$ interlayer formation, using a two-step MBE growth method of Ga pre-deposition followed by GaN growth directly on Si (001). High flux of N-free Ga pre-deposition saturates Si surfaces, hindering the $SiN_x$ interlayer formation. Subsequent GaN NW growth leads to the formation of the mixed phase of ZB and WZ with a significant ZB content. In addition, it has been demonstrated the nucleation and transformation of ZB and WZ GaN nanocrystals (NCs) in GaAs via ion implantation followed by thermal annealing.[26] Post implantation annealing via RTA at 600 to 900$^{\circ}$C leads to the formation of ZB GaN NCs, with a maximum radius of ~1.75 nm. Based on the results the formation of ZB GaN NCs by implantation and annealing, the smaller size of GaN NCs could have

ZB crystal structures. Thus, to grow pure ZB GaN NWs, extremely small size of ZB GaN NCs in the size of 1-2 nm may act as a seed for ZB GaN NWs. Figure 6.6 presents a schematic illustration of GaN NW growth via two-step MBE process: 1) small sized GaN QD formation for seeds, 2) epitaxial growth of GaN NWs. Further work is necessary to fabricate small ZB GaN QDs.

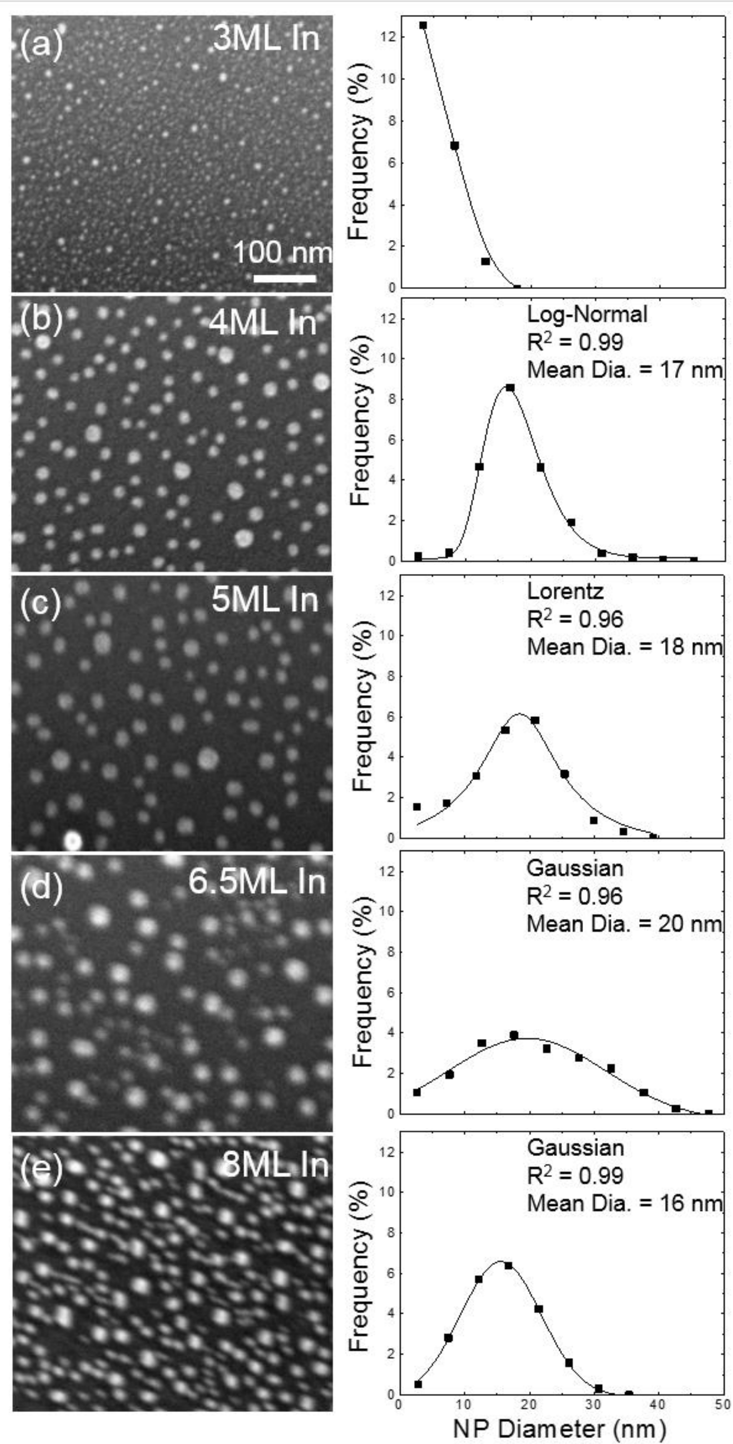


Fig. 6.1 SEM images of In droplets deposited on Si (001) (a) 3ML, (b) 4ML, (c) 5ML, (d) 6.5ML, and (e) 8ML, with the corresponding In droplet size distributions on right sides.

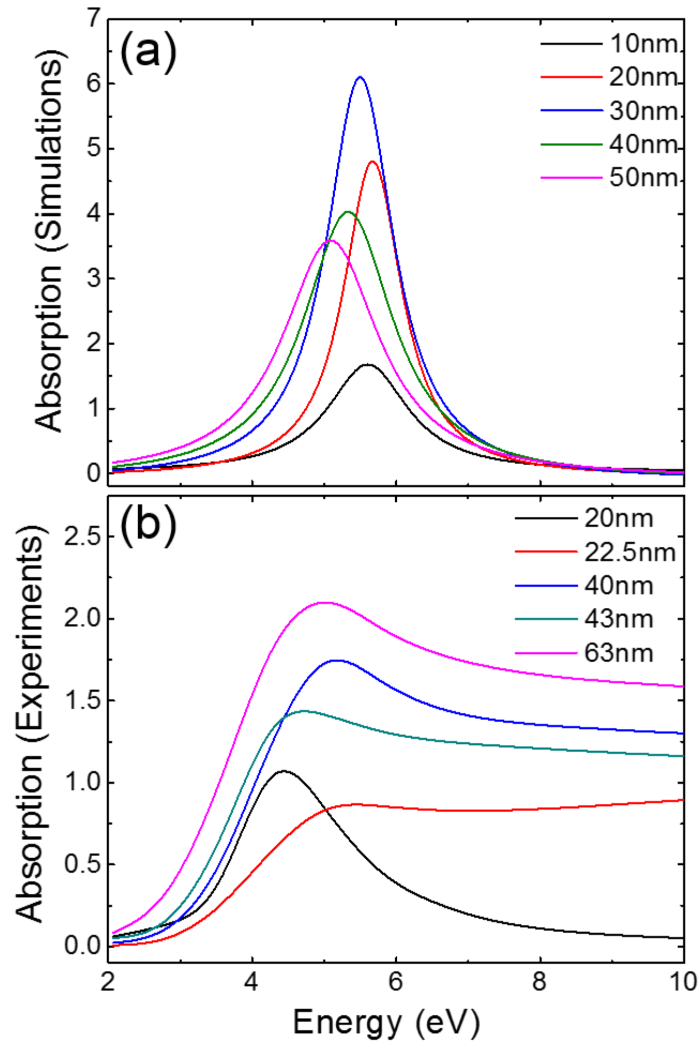


Fig. 6.2 Plots of (a) simulated and (b) measured absorption efficiency (effective absorption cross-section of In droplet / geometrical cross section of In droplet) vs. Energy with various In diameter ranging from 10 to 63nm.

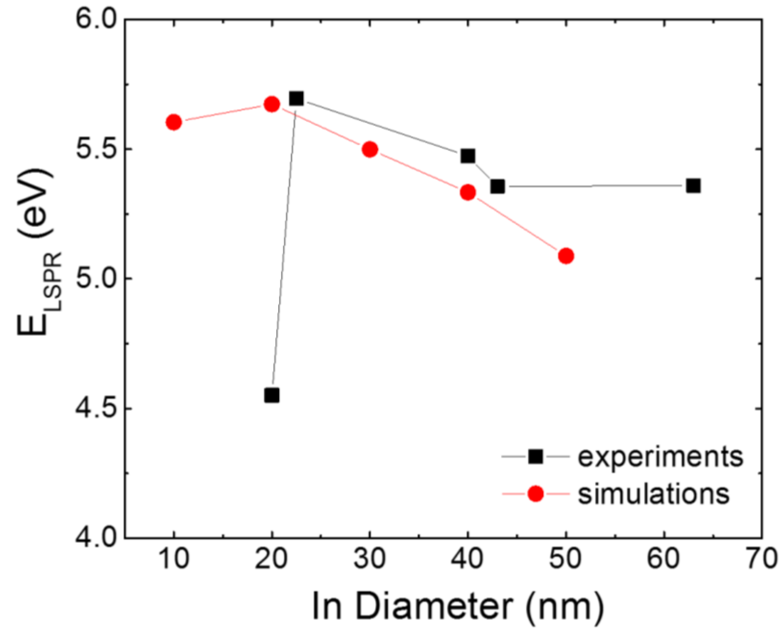


Fig. 6.3 Comparison of the $E_{LSPR}$ collected from ellipsometry experiments and FDTD absorption simulations vs. In droplet diameter. LSPR energy of In droplets on Si (001) ranges from 5 to 6eV, showing redshift with increasing In droplet size.

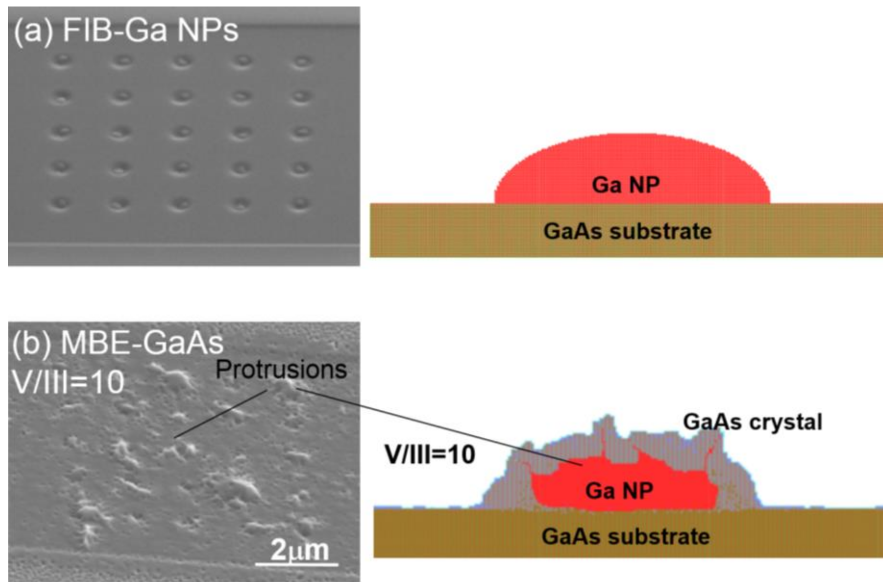


Fig. 6.4 SEM images of (a) FIB-Ga NPs on GaAs and (b) GaAs overgrowth with V/III of 10, with the kinetic Monte-Carlo (KMC) simulation result showing surface protrusions.

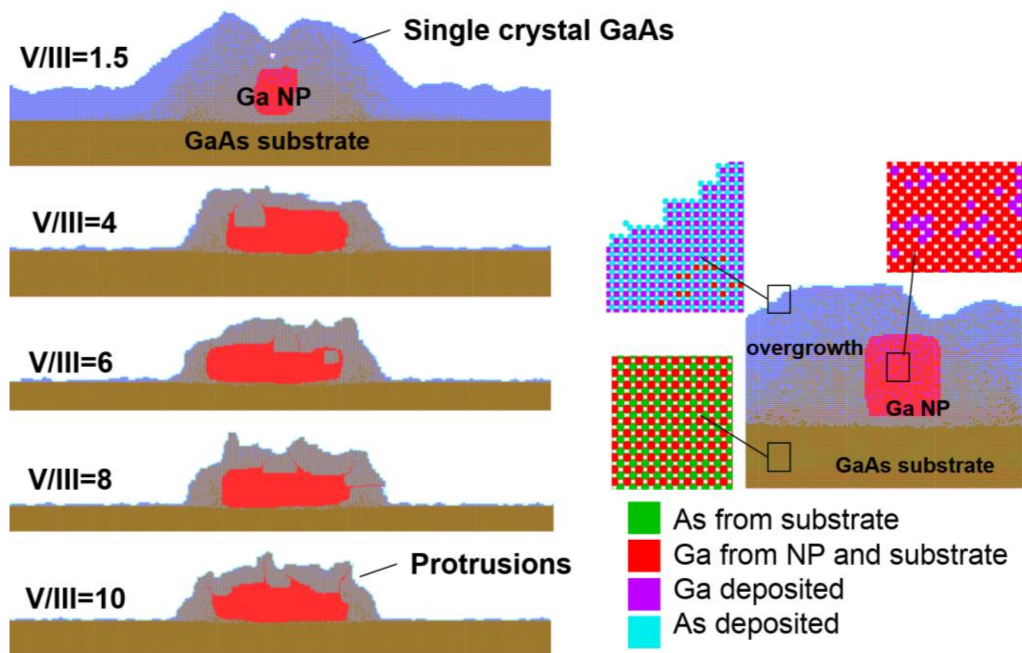


Fig. 6.5 KMC simulation results with various V/III incorporation rate ratios ranging from 1.5 to 10. The color codes are depicted in the right side: (green) As from substrate, (red) Ga from NP and substrate, (violet) Ga deposited, and (bright blue) As deposited.

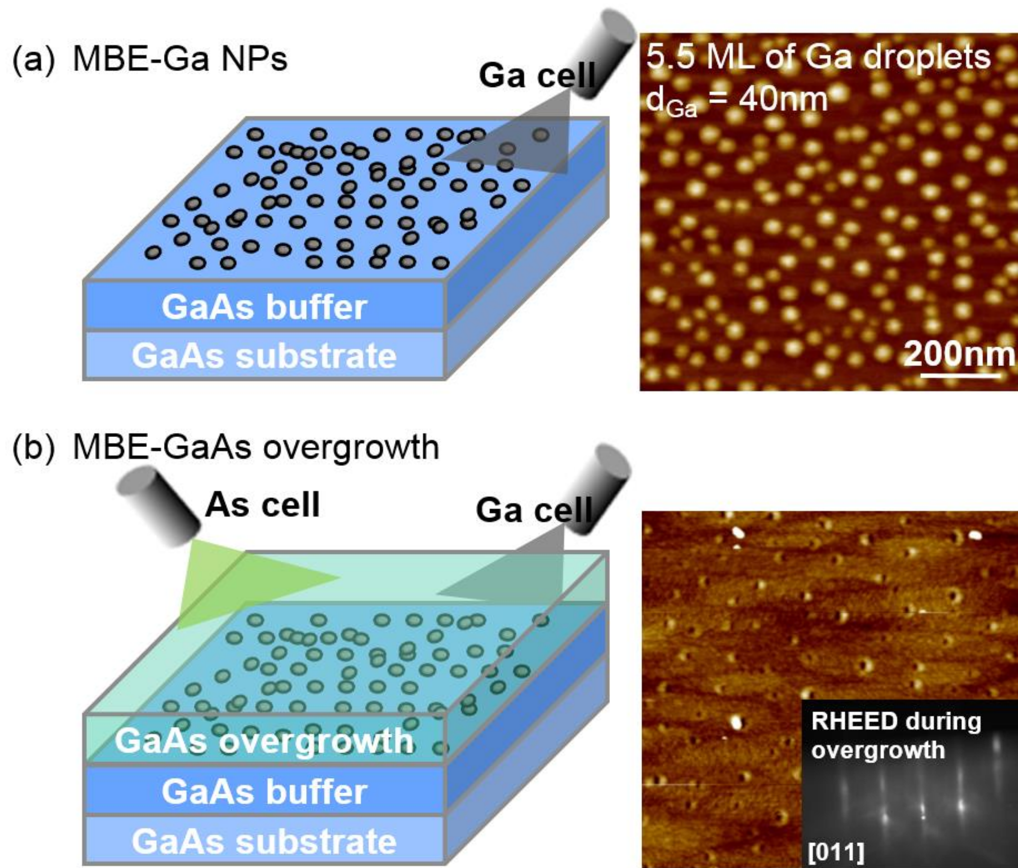


Fig. 6.6 Schematic illustration of Single crystalline GaAs overgrowth using MBE-fabrication of Ga droplets, followed by *in situ* MBE GaAs overgrowth.

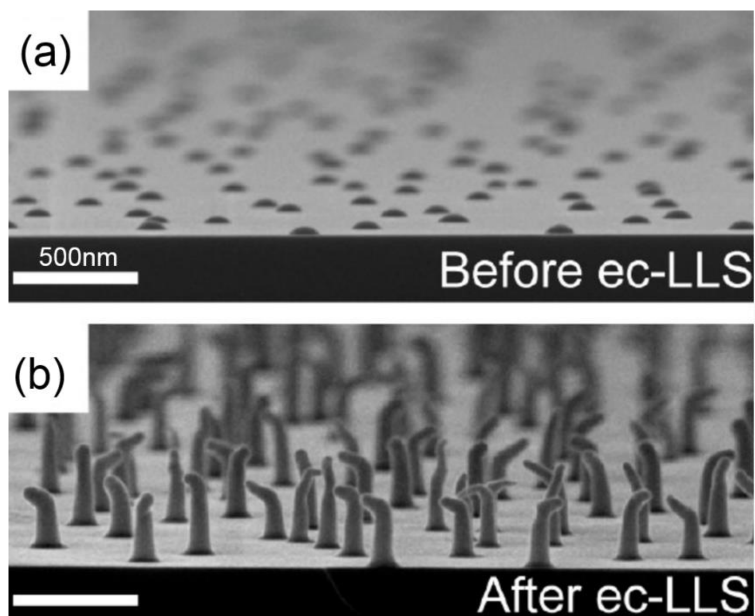


Fig. 6.7 (a) A cross-sectional scanning electron micrograph of a Ge (111) substrate decorated with discrete liquid Ga droplets. (b) Same as (a) but after 60 s ec-LLS process. Reprinted figures with permission from E. Fahrenkrug *et. al. Nano Lett.* **14**(2) 847 (2014). Copyright 2014 by ACS Publications.

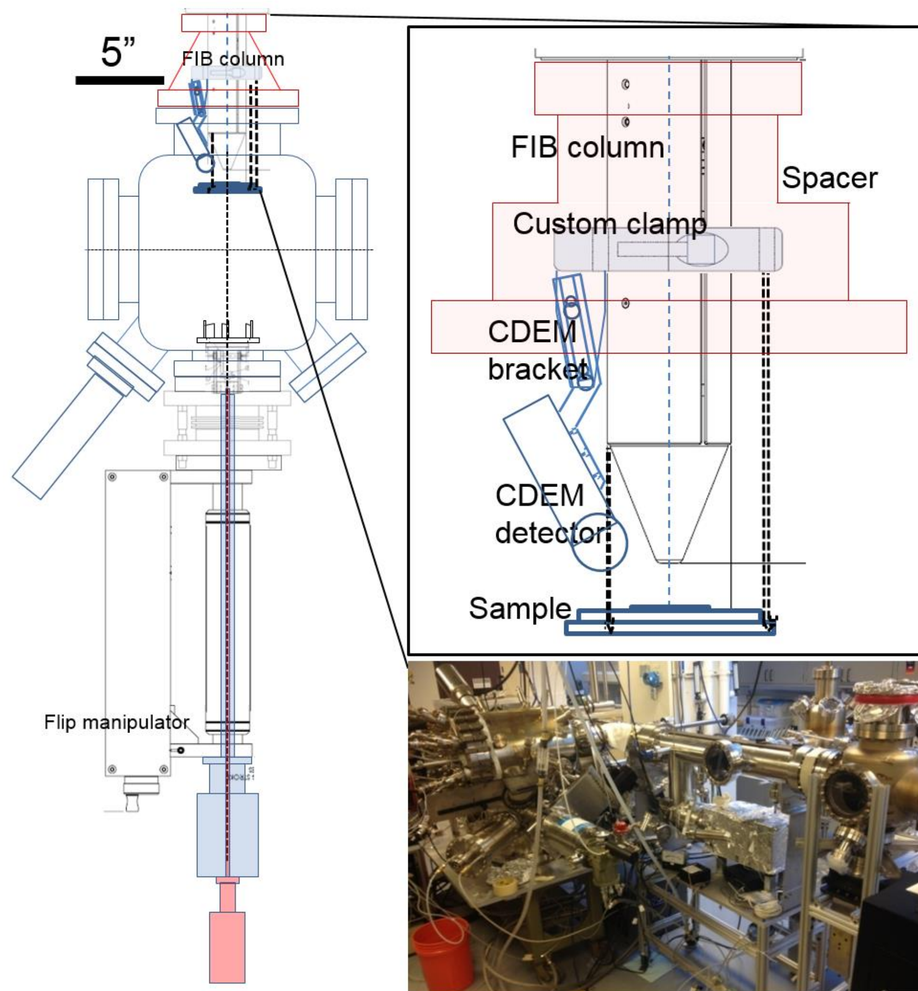


Fig. 6.8 Schematic chamber modification design for *in situ* FIB source, including a custom clamp and a UHV spacer. The custom clamp is for reducing the vibrational interferences, providing a mechanical stability between the FIB column and sample surfaces. This *in situ* system enables oxide-free sample preparations.

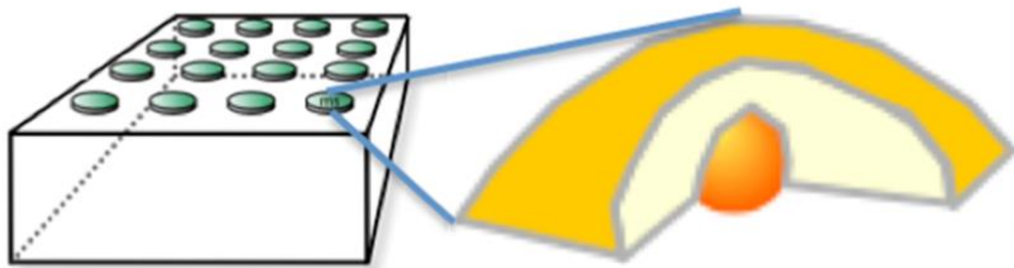

Fig. 6.9 Schematic illustration of FIB-directed Epitaxial Core-Shell Nanostructures: 2D array of metal-semiconductor epitaxial core-shell nanostructures with Ga droplet cores and a surrounding GaN.

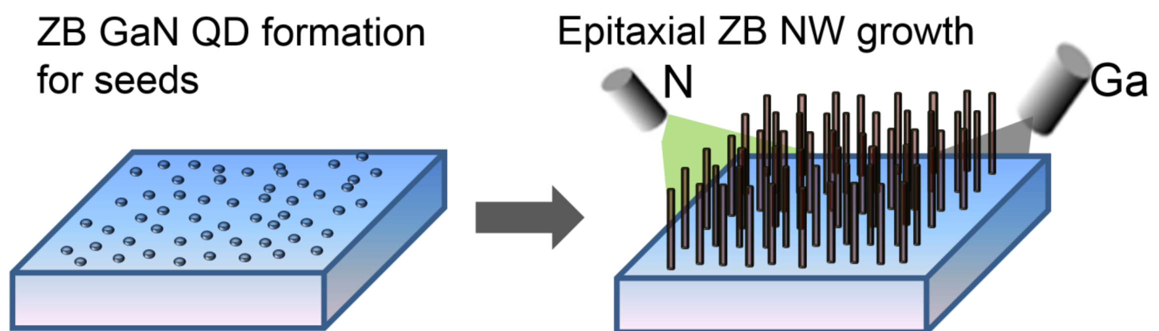


Fig. 6.10 Schematic illustration of GaN NW growth via two-step MBE process: 1) small sized GaN QD formation for seeds, 2) epitaxial growth of GaN NWs.

### 6.3 References


[1] K.L Kelly, E. Coronado, L.L Zhao, and G.C. Schatz, *J. Phys. Chem. B*, **107**, 668 (2003).

[2] M. G. Blaber, M. D. Arnold, N. Harris, M. J. Ford, and M. B. Cortie, *Physica B* **394**, 184 (2007).

[3] P. R. West, S. Ishii, G. V. Naik, N. K. Emani, V. M. Shalaev, and A. Boltasseva, *Laser Photonics Rev*. **4**, 795 (2010).

[4] M. G. Blaber, M. D. Arnold, and M. J. Ford, *J. Phys.: Condens. Matter* 22 (2010).

[5] E. H. Hwang, and S. D. Sarma, *Phys. Rev. B* **75** (2007).

[6] L. Ju, B. Geng, J. Horng, C. Girit, M. Martin, Z. Hao, H. A. Bechtel, X. Liang, A. Zettl, and Y. R. Shen, *Nat. Nanotechnol*. **6**, 630 (2011).

[7] M. Kanehara, H. Koike, T. Yoshinaga, and T. Teranishi, *J. Am. Chem. Soc.* **131**, 17736 (2009).

[8] T. R. Gordon, T. Paik, D. R. Klein, G. V. Naik, H. Caglayan, A. Boltasseva, and C. B. Murray, *Nano Lett.* **13**, 2857 (2013).

[9] J. M. Luther, P. K. Jain, T. Ewers, and A. P. Alivisatos, *Nat. Mater.* **10**, 361 (2011).

[10] W. M. Kim, S. H. Kim, K. S. Lee, T. S. Lee, and I. H. Kim, *Appl. Surf. Sci.* **261**, 749 (2012).

[11] J. M. McMahon, G. C. Schatz, and S. K. Gray, *Phys. Chem. Chem. Phys.* **15**, 5415 (2012).

[12] E. J. Zeman, and G. C. Schatz, *J. Phys. Chem.* **91**, 634 (1987).

[13] J.C. Lemonnier, *J. Phys. C: Solid State Phys.* **8**, 2812 (1975).

[14] E. Fahrenkrug, J. Gu, S. Jeon, P. A. Veneman, R. S. Goldman, and S. Maldonado, *Nano Lett.* **14**(2), 847 (2014).

[15] X. Li, J. Liu, H. Guo, X. Zhou, C. Wang, P. Sun, X. Hu, and G. Lu, *RSC Adv.*, **5**, 545 (2015).

[16] N. Zhang, S. Liu and Y. J. Xu, *Nanoscale,* **4**, 2227 (2012).

[17] R. Ghosh Chaudhuri and S. Paria, *Chem. Rev.,* **112**, 2373 (2012).

[18] L. Zhang, D. A. Blom and H. Wang, *Chem. Mater.*, **23**, 4587 (2011).

[19] L. Zhou, X. Yu and J. Zhu, *Nano Lett.*, **14**, 1093 (2014).

[20] T. Hirakawa and P. V. Kamat, *Langmuir,* **20**, 5645 (2004).

[21] Y.-T. Yu and P. Dutta, *Sens. Actuators, B*, **157**, 444 (2011).

[22] S. M. Majhi, P. Rai, S. Raj, B. S. Chon, K. K. Park and Y. T. Yu, *ACS Appl. Mater. Interfaces,* **6**, 7491 (2014).

[23] X. Li, X. Zhou, H. Guo, C. Wang, J. Liu, P. Sun, F. Liu and G. Lu, *ACS Appl. Mater. Interfaces,* **6**, 18661 (2014).

[24] N. Zhang, X. Fu and Y.-J. Xu, *J. Mater. Chem.*, **21**, 8152 (2011).

[25] N. Zhang, S. Liu, X. Fu and Y.-J. Xu, *J. Phys. Chem. C,* **115**, 9136 (2011).

[26] A. W. Wood, R. R. Collino, P. T. Wang, Y. Q. Wang, R. S. Goldman, *Appl. Phy. Lett.,* **100**, 203113 (2012).

## Appendices

## Appendix A

### NP depth-dependent crystallinity of GaAs overgrown layer

In Appendix A, we discuss the thickness dependence of the crystallinity of the overgrown layer. Figure A.1 (a) shows the GIXRD scans of a (001) GaAs substrate and overgrown layers. For the GaAs substrate, the Bragg diffraction conditions of single crystalline (001) GaAs are not satisfied with $\theta_i = 27.3°$; therefore, diffraction peaks are not apparent. However, for the overgrown layers, peaks at $2\theta = 27.3°$, $45.3°$ and $53.7°$, corresponding to GaAs (111), (220) and (311) planes are observed, revealing the presence of polycrystalline GaAs atop the GaAs substrate. Using the FWHM and integrated intensities of the (111), (220), and (311) diffraction peaks, we quantify the grain size,[1,2] and the preferential orientation (or texture) of the overgrown GaAs layers, namely $f_{(111)}$,[3,4] the fraction of (111) – oriented planes. In Fig. A.1 (b), the grain sizes and $f_{(111)}$ values are plotted as a function of overgrown layer thickness. For thicknesses up to 100 nm, the average grain size is 6.7 ± 0.7 nm, with $f_{(111)} = 0.45 \pm 0.03$, higher than that of a randomly – oriented GaAs powder, $f_{(111)} = 0.305$,[5] indicating a (111) texture. On the other hand, for thicknesses beyond 100 nm, the grain size increases up to 15.2 ± 0.1 nm, while $f_{(111)}$ decreases down to 0.24, suggesting a decrease in the (111) texture. Thus, the grain size ((111) texture) is dependent (inversely dependent) on film thickness.

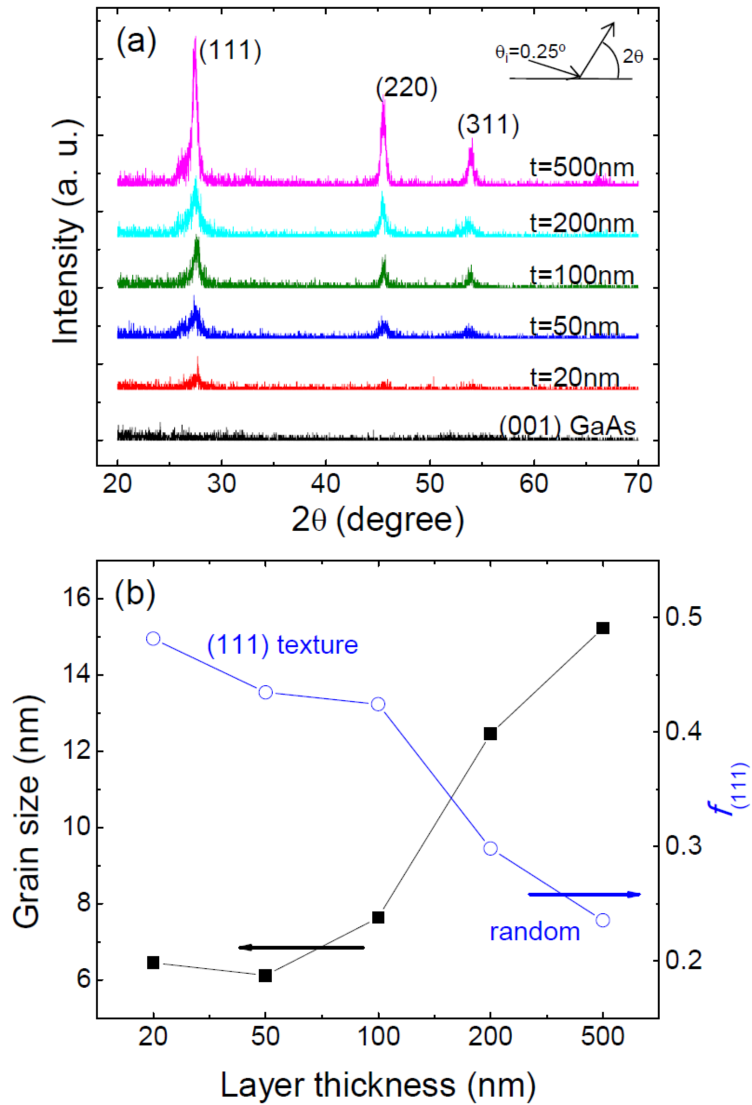


Fig. A.1 (a) GIXRD scans of a GaAs (001) substrate and overgrown GaAs layers in the thickness range 20 nm to 500 nm, using a monochromatic Cu-Kα (λ = 1.5405 Å) rotating anode operated at 40 kV and 100 mA. For all overgrown layers, peaks at 2θ of 27.3°, 45.3° and 53.7°, corresponding to GaAs (111), (220) and (311) planes, are apparent. (b) The calculated grain sizes and fractions of GaAs (111) planes, $f_{(111)}$, for the thickness ranging from 20 nm to 500 nm. For overgrown layer thicknesses up to 100 nm, the grain size ($f_{(111)}$ value) is 6.7 ± 0.7 nm (0.45 ± 0.03). For overgrown layer thicknesses beyond 100nm, the grain size ($f_{(111)}$ value) increases up to (decreases down to) 15.2 ± 0.1 nm (0.24).

**References**

[1] A. L. Patterson, *Phys. Rev.* **56,** 978 (1939).

[2] $D = \frac{0.9\lambda}{B\cos\theta}$ where B is FWHM value, λ is the X-ray wavelength, θ is the diffraction angle, and D is grain size.

[3] F. K. Lotgering, *J. Inorg. Nucl. Chem.* **9,** 113 (1959).

[4] $f_{(111)} = \frac{p_{(111)} - p_{0(111)}}{1 - p_{0(111)}}$ where $P_{(111)}$ is a ratio of integrated intensity of (111) reflection to the sum of the reflections for overgrown layers, and $P_{0(111)}$ is an equivalent value for a randomly oriented GaAs**.**

[5] M.M. Rahman, T. Soga, and T. Jimbo, *IUMRS-ICEM* 679 (2002).

# Appendix B

## Maxwell-Garnett Effective Medium Theory

In Appendix B, we describe Maxwell-Garnett effective medium theory, which was used to estimate the NP buried depth-dependent effective permittivity values in Chapter 3. Effective medium approximations (EMA) is an analytical modeling method that describes the macroscopic properties of composite materials.[1] EMA is developed from averaging the multiple values of the constituents that directly make up the composite material. Although precise calculation is nearly impossible, EMA has been developed that can produce acceptable approximations which describe useful parameters and properties of the composite material.[2,3,4,5] To estimate NP depth-dependent effective permittivity values for GaAs:Ga nanocomposites using effective medium approximations, we assume the cases in which the Ga NPs are existing in between two layers of GaAs, which are GaAs substrate below Ga NP arrays and overgrown GaAs above Ga NP arrays. The depth-dependent effective permittivity in GaAs:Ga nanocomposites is calculated using Equation. B.1,

$$\frac{\varepsilon-\varepsilon_{host}}{L\varepsilon+(1-L)\varepsilon_{host}} = q\,\frac{\varepsilon_{metal}-\varepsilon_{host}}{L\varepsilon_{metal}+(1-L)\varepsilon_{host}} \qquad \text{(B.1)}$$

where $\varepsilon$ is effective permittivity, $\varepsilon_{host}$ is $\varepsilon_{GaAs}$ (@10K) of 12.35, $\varepsilon_{metal}$ is metal NP permittivity, q is NP volume fractions, and L is a depolarization factor of 0.5272 for an oblate hemispheroid. Figure B. 1 shows the plots of effective permittivity of GaAs:Ga nanocomposites vs. NP buried depth, using Maxwell-Garnett effective medium approximations. From this calculation, the effective permittivity values of each GaAs:Ga nanocomposite structure are obtained. The observed diameter, height, and density of Ga

NP arrays are used to estimate NP volume fractions. The LSPR wavelength is defined by Equation B.2:

$$\lambda_{R=}\lambda_P\left[\frac{\varepsilon}{(1-q)L}-\varepsilon+\delta\varepsilon^b+1\right]^{1/2} \qquad (\mathrm{B.2})$$

where $\lambda_P$ is bulk Ga plasmon resonance (nm) of 88nm, and $\lambda_{R}$ : surface plasmon resonance (nm). Figure B.2 presents plots of calculated $E_{LSPR}$ with the effective permittivity values of GaAs:Ga nanocomposites vs. NP depth. In the cases of larger NP sizes and thicker NP buried depths, it is evident that $E_{LSPR}$ is redshifted. However, the calculated $E_{LSPR}$ values are greater than those extracted from Absorptance spectra in Chapter 3 Fig. 3.7 (b). The difference from the extracted values and calculated values is likely to be induced by the assumptions that the calculation considers randomly dispersed NP in a volume and the calculation does not consider the influence of NP size on LSPR.

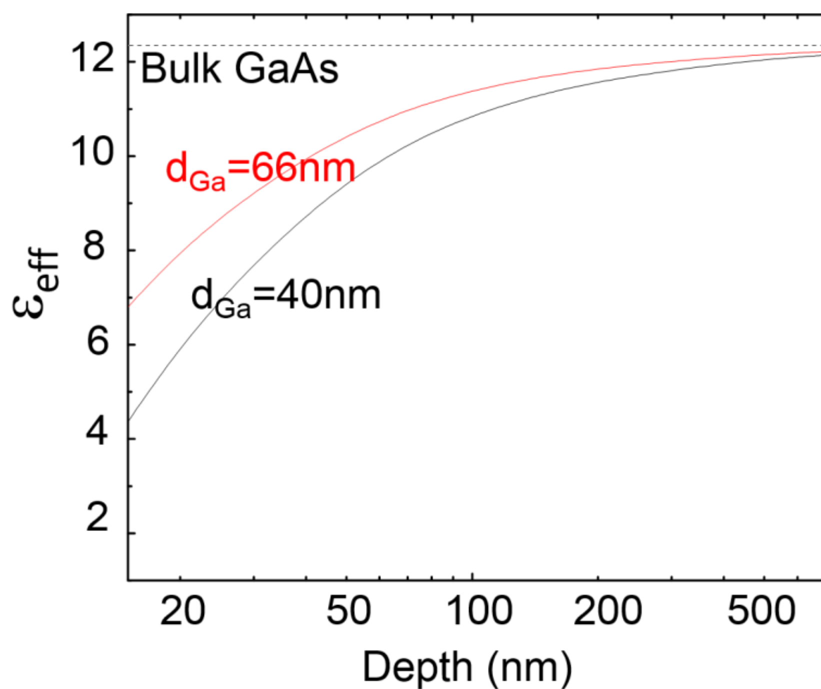


Fig. B.1 Plots of effective permittivity of GaAs:Ga nanocomposites vs. NP buried depth, using Maxwell-Garnett effective medium approximations. The observed diameter, height, and density of Ga NP arrays are used to estimate NP volume fractions.

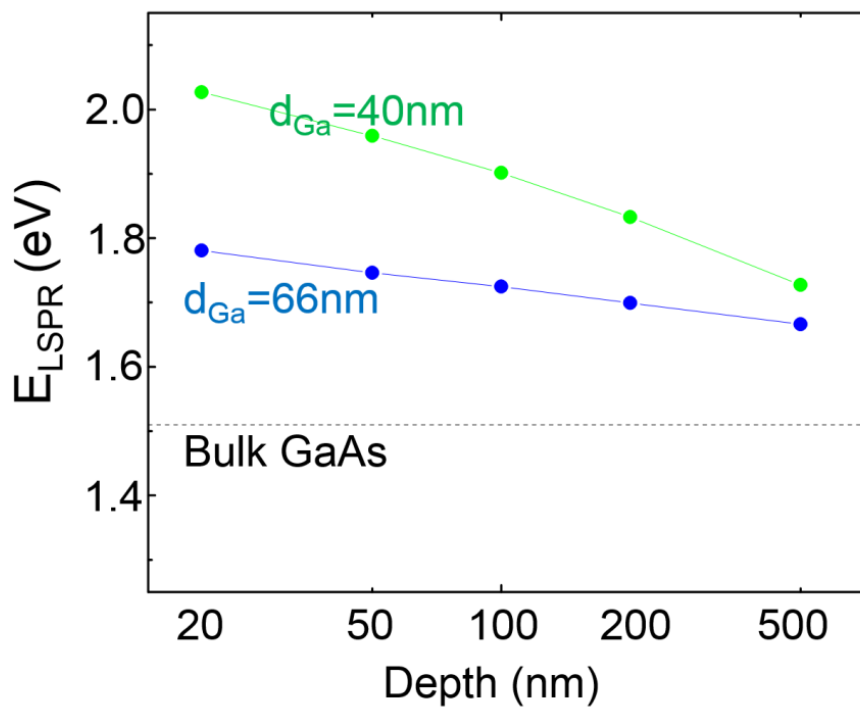


Fig. B.2 Plots of calculated $E_{LSPR}$ with the effective permittivity values of GaAs:Ga nanocomposites vs. NP depth. In the cases of larger NP sizes and thicker NP buried depths, it is evident that $E_{LSPR}$ is redshifted.

**References**

[1] J. P. Marton, and J. R. Lemon, *Phys. Rev. B* **4**, 271 (1971).

[2] G. Xu, M. Tazawa, P. Jin, S. Nakao, and K. Yoshimura, *Appl. Phys. Lett*. **82**, 3811 (2003).

[3] X. Liu, D. Li, X. Sun, Z. Li, H. Song, H. Jiang, and Y. Chen, *Sci Rep.* **5**, 12555 (2015).

[4] R. W. Cohen, G. D. Cody, M. D. Coutts, and B. Abeles, *Phys. Rev. B* **8**, 3689 (1973).

[5] G. L. Hornyak, C. J. Patrissi, and C. R. Martin, *J. Phys. Chem. B* **101**, 1548 (1997).

# Appendix C

## Lumerical FDTD simulation codes

```
################################################
# calculate power absorbed in region where
# the refractive indes is that of a particular materials
# (Silicon and Silver) for all frequencies,
# by integrating the absorption over this material.
#
# This file should work for both 2D and 3D simulation
#################################################
clear;
closeall;

# get monitor data
runanalysis;
m="pabs_adv";
Pabs=getresult(m,"Pabs");
n = getresult(m+"::index","index");
n = n.index_x;
f=Pabs.f;
nx=length(Pabs.x);
ny=length(Pabs.y);
nz=length(Pabs.z);
nf=length(Pabs.f);

# define material filters

filter_mat_GaAs = "GaAs - Palik";
filter_mat_hemisphere = "Ga-per";

filter_real_GaAs = matrix(nx,ny,nz,nf);
filter_imag_GaAs = matrix(nx,ny,nz,nf);
filter_real_hemisphere = matrix(nx,ny,nz,nf);
filter_imag_hemisphere = matrix(nx,ny,nz,nf);

n_filter_real_GaAs =
real(getfdtdindex(filter_mat_GaAs,f,min(f),max(f)));
n_filter_imag_GaAs =
imag(getfdtdindex(filter_mat_GaAs,f,min(f),max(f)));
n_filter_real_hemisphere =
real(getfdtdindex(filter_mat_hemisphere,f,min(f),max(f)));
n_filter_imag_hemisphere =
imag(getfdtdindex(filter_mat_hemisphere,f,min(f),max(f)));

#relative difference for almosequal comparator
rel_diff = 1e-15;



for (i=1:nf) {
```

```
    filter_real_GaAs(1:nx,1:ny,1:nz,i) =
almostequal(n_filter_real_GaAs(2),pinch(real(n),4,2),rel_diff);
    filter_imag_GaAs(1:nx,1:ny,1:nz,i) =
almostequal(n_filter_imag_GaAs(2),pinch(imag(n),4,2),rel_diff);
}
filter_GaAs=filter_real_GaAs*filter_imag_GaAs;




for (i=1:nf) {
    filter_real_hemisphere(1:nx,1:ny,1:nz,i) =
almostequal(n_filter_real_hemisphere(2),pinch(real(n),4,2),rel_diff);
    filter_imag_hemisphere(1:nx,1:ny,1:nz,i) =
almostequal(n_filter_imag_hemisphere(2),pinch(imag(n),4,2),rel_diff);
}
filter_hemisphere=filter_real_hemisphere*filter_imag_hemisphere;

#integrate
Pabs_GaAs = integrate2(Pabs.Pabs*filter_GaAs,1:3,Pabs.x,Pabs.y,Pabs.z);
Pabs_hemisphere =
integrate2(Pabs.Pabs*filter_hemisphere,1:3,Pabs.x,Pabs.y,Pabs.z);

#Plots of filters and total absorption at a wavelength
if (nz>1){ # 3D
image(Pabs.x*1e6,Pabs.y*1e6,pinch(pinch(filter_GaAs,4,8),3,20),"x
(um)","z (um)","filter_GaAs");
image(Pabs.x*1e6,Pabs.y*1e6,pinch(pinch(filter_hemisphere,4,8),3,20),"x
(um)","z (um)","filter_hemisphere");
image(Pabs.x*1e6,Pabs.y*1e6,pinch(pinch(log10(Pabs.Pabs),4,8),3,20),"x
(um)","z (um)","Total Absorption");
}else{ # 2D
image(Pabs.x*1e6,Pabs.y*1e6,pinch(filter_GaAs,4,8),"x (um)","z
(um)","filter_GaAs");
image(Pabs.x*1e6,Pabs.y*1e6,pinch(filter_hemisphere,4,8),"x (um)","z
(um)","filter_hemisphere");
image(Pabs.x*1e6,Pabs.y*1e6,pinch(log10(Pabs.Pabs),4,8),"x (um)","z
(um)","Total Absorption");
}

# plots of absorption spectrum
plot(c/f*1e9,Pabs_GaAs,"wavelength","Total Power Absorption","Total
Absorption in GaAs");
plot(c/f*1e9,Pabs_hemisphere,"wavelength","Total Power
Absorption","Total Absorption in hemisphere");
plot(c/f*1e9,Pabs_GaAs+Pabs_hemisphere,"wavelength","Total Power
Absorption","Total absorption");

plot(c/f*1e9,Pabs_adv,"wavelength","Power Absorption","Absorption in
GaAs");
plot(c/f*1e9,Pabs.Pabs*filter_GaAs,"wavelength","Power
Absorption","Absorption in GaAs");
plot(c/f*1e9,Pabs.Pabs*filter_hemisphere,"wavelength","Power
Absorption","Absorption in hemisphere");
plot(c/f*1e9,Pgaas+Phemi,"wavelength","Power Absorption","absorption");
```

## Appendix D

## Validation of Lumerical Absorptance Simulations

In Appendix D, to validate these simulations, we calculate and compare the reflectance of bulk GaAs to experimental data.[1] Figure D.1 (a) shows the simulated absorptance of bulk GaAs (at 300K), exhibiting the absorption at 1.42eV presumably corresponding to the GaAs bandedge. To determine the reflectance of bulk GaAs, we assume negligible transmittance, such that *Absorptance* (E) = 1-*Reflectance* (E), as shown in Fig. D.1 (b). The resulting energy-dependent reflectance spectrum of bulk GaAs at 300K is similar to the measured reflectance reported by H. Ehrenreich et al.,[33] for which enhancements in reflectance are apparent at 3 and 5 eV.

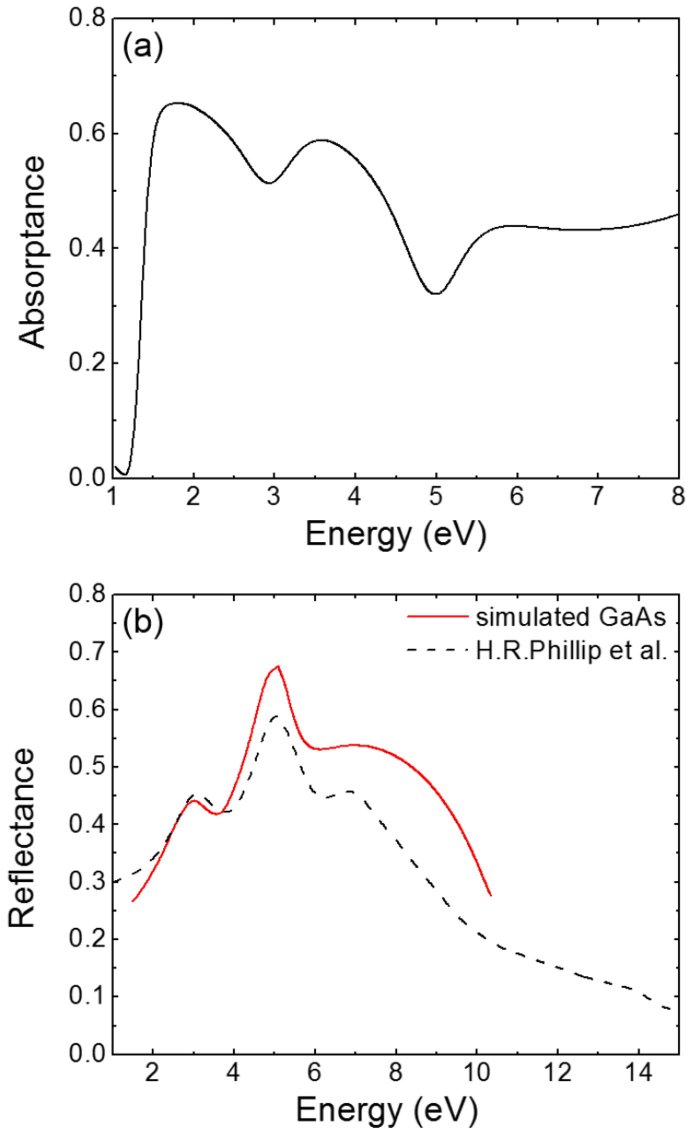


Fig. D.1 (a) the simulated energy-dependent absorptance of bulk GaAs (at 300K), exhibiting the absorption at 1.42eV presumably corresponding to the GaAs bandedge. (b) the simulated energy-dependent reflectance spectrum of bulk GaAs at 300K (red line), in comparison to the measured reflectance reported by H. R. Phillip et al. (black dashed line). Reprinted figures with permission from H. R. Phillip *et. al. Phys. Rev.* **129** (4) 1550 (1963). Copyright 1963 by American Physical Society.

**References**

---

[1] H. R. Phillip, and H. Ehrenreich, *Phys. Rev.* **129**(4), 1550 (1963).

# Appendix E

## Size Analysis of Droplets and Quantum Dots

In Appendix E, we describe the procedures for the identification and size quantification of the MBE-grown metal droplets and semiconductor QDs based on AFM images. Scanning Probe Image Processor (SPIP) was used to perform the analyses. We also describe how the QD size distributions are determined using Origin software.

To quantify the droplet and QD size from AFM images, we used the Particle and Pore Analysis module in SPIP. In particular, AFM images consisting of $1024 \times 1024$ pixels were loaded in SPIP. The "Advanced Threshold" detection method was used for droplet and QD identification. Based on the root mean square (RMS) of the height values within the image, we defined a height threshold level by adding $5 \times$ RMS to the substrate background level. Regions above the defined threshold level were identified as droplets and QDs. Finally, the droplet and QD sizes (i.e. diameters, heights, and etc.) were exported from SPIP in a spreadsheet. With the droplet and QD sizes obtained from AFM images, we calculated the mean and standard deviation of the droplet and QD sizes and plotted the size distributions as described below. We first plotted the droplet and QD frequency (%) as a function of droplet and QD diameter (or height) and then fitted the histogram with a Gaussian distribution in Origin.

# Appendix F

## Materials Parameters

This appendix describes GaAs material parameters and the values of energy-dependent $\varepsilon_{Ga}$ and $\varepsilon_{GaAs}$ used in the GaAs:Ga nanocomposites absorptance and emission analysis in Chapter 3. The plots of energy-dependent $\varepsilon_{Ga}$ and $\varepsilon_{GaAs}$ are presented in Fig. F.1[1] and Fig. F.2.[2,3]

Table F. 1 GaAs material parameters[4]

| Crystal structure | Zinc Blende |
|---|---|
| Number of atoms in 1 $cm^3$ | $4.42 \cdot 10^{22}$ |
| Debye temperature | 360 K |
| Density | 5.32 g $cm^{-3}$ |
| Dielectric constant (static ) | 12.9 |
| Dielectric constant (high frequency) | 10.89 |
| Effective electron mass $m_e$ | $0.063m_o$ |
| Effective hole masses $m_h$ | $0.51m_o$ |
| Effective hole masses $m_{lp}$ | $0.082m_o$ |
| Electron affinity | 4.07 eV |
| Lattice constant | 5.65325 A |
| Optical phonon energy | 0.035 eV |

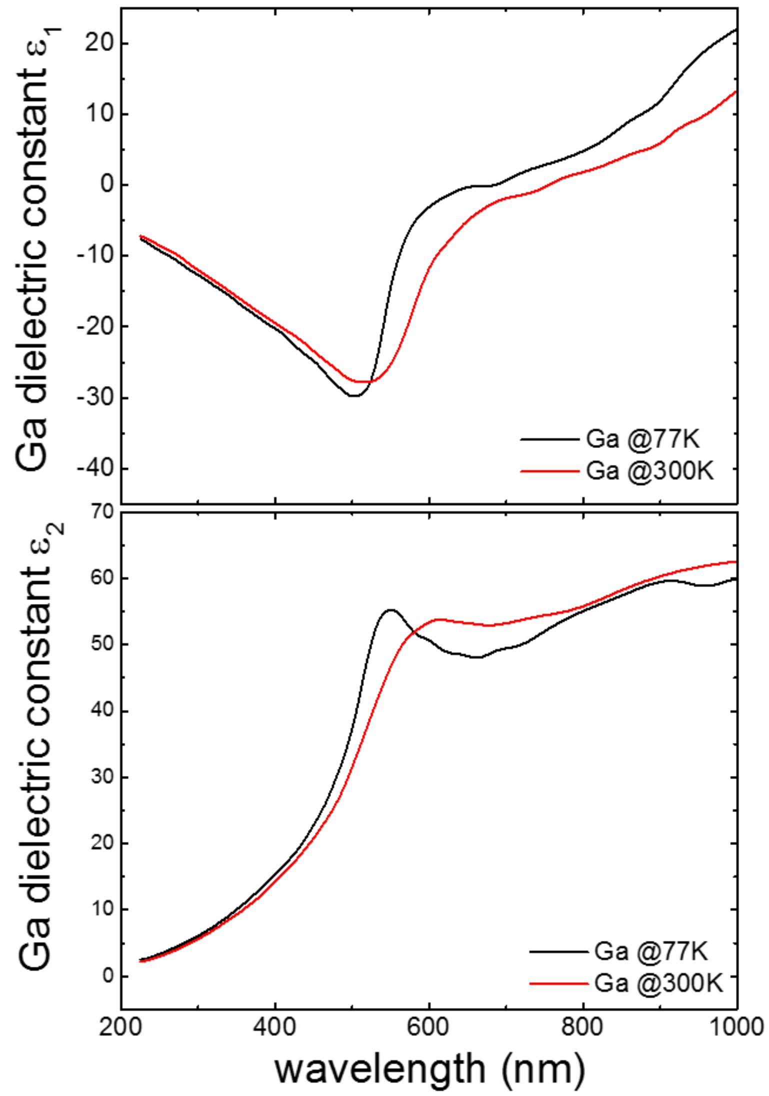


Fig. F.1 Plots of energy-dependent $\varepsilon_{Ga}$, (top) real parts of dielectric constant, (bottom) imaginary parts of dielectric constant.

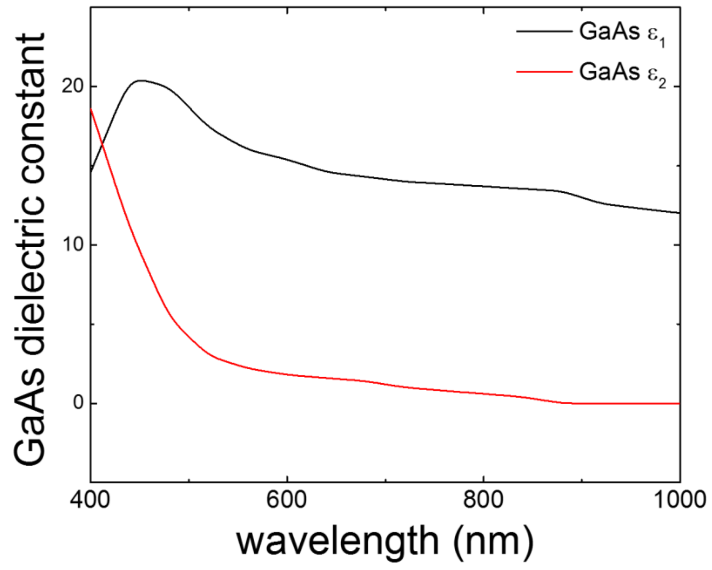


Fig. F.2 Plots of energy-dependent $\varepsilon_{GaAs}$.

**References**

[1] M. W. Knight, T. Coenen, Y. Yang, B. J. M. Brenny, M. Losurdo, A. S. Brown, H. O. Everitt, and A. Polman, *ACS Nano* **9**, 2049 (2015).

[2] M. Scalora, M. A. Vincenti, V. Roppo, J. V. Foreman, J. W. Haus, N. Akozbek, and M. J. Bloemer, *IEEE/LEOS.* 132 (2009).

[3] I.Strzalkowski, S. Joshi, and C. R. Crowell, *Appl. Phys. Lett.* **28**, 350 (1976).

[4] http://www.ioffe.ru/SVA/NSM/Semicond/GaAs/basic.html

## Appendix G

### Refraction-corrected Information depth

In Appendix G, we describe the information depth of thin nanostructures deposited on substrates. In chapter 5, the crystallinity of GaN was determined using x-ray diffraction (XRD), conducted with a 12 kW Rigaku rotating anode source (Cu target and graphite monochromator) at an incident angle ($\theta_i$) ranging from 1 to 8° for low-incident-beam-angle diffraction (LIBAD) method.[1] LIBAD is a nondestructive technique to study surface structure as well as to determine the phase depth profile. In the LIBAD configuration, X-ray penetration depth is controlled by fixing the incident angle. The refraction corrected information depth can be calculated based on the incident angle and material parameters according to Eq. G. 1 and G. 2, where $\mu$ is GaN linear absorption coefficient at 0.154 nm and $\alpha$ is an incident angle.

$$Information\ depth\ (nm) = \frac{1}{\mu k_{\alpha}} + \frac{1}{1 - \exp(\mu \times thickness \times k_{\alpha})} \qquad (G.1)$$

$$k\alpha = \frac{1}{sin\alpha} + \frac{1}{\sin(2\theta - \alpha)} \qquad (G.2)$$

Since X-rays are electromagnetic radiation that are absorbed by matter following identical laws as in optical absorption for partial transmission, the transmitted X-ray intensity decays exponentially with respect to the path length in the matter it travels. Figure G. 1 shows the incident angle-dependent information depth of GaN.

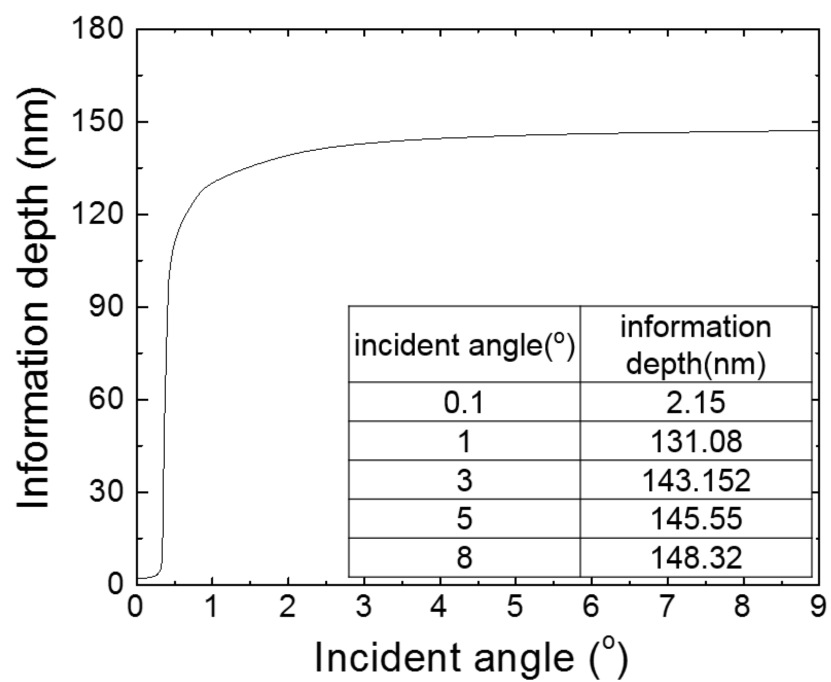


Fig. G.1 A Plot of incident angle-dependent information depth of GaN with 0.154nm X-ray radiation.

**References**

---

[1] K. V. Acker, L. D. Buyser, J. P. Celis, and P. V. Houtte, *J. Appl. Cryst.* **27**, 56 (1994).

## Appendix H

## List of Samples

Table H.1. Samples of GaAs overgrowth on Ga droplets

| RMBE# | oxide desorption | | GaAs overgrowth | | | | | | | |
|---|---|---|---|---|---|---|---|---|---|---|
| | temp (°C) | time | As2 | | Ga | | Incor. ratio | growth rate (μm/h) | thickness (nm) | $T_{growth}$ (°C) |
| | | | NV (mil) | BEP (Torr) | Temp (°C) | BEP (Torr) | | | | |
| RMBE529 | 610 | 10min | 180 | no info | 905 | no info | no info | 0.05 | 30 | 450C |
| RMBE530 | 610 | 10min | 180 | no info | 905 | no info | no info | 0.05 | 50 | 450C |
| RMBE640 | 610 | 10min | 226 | 1.87E-5 | 915 | 5.67E-08 | no info | 0.05 | no info | 450C |
| RMBE644 | 580 | 10min | 170 | 1.09E-5 | 1040 | 9.20E-07 | 1.14 | 1.07 | 70 | 580C |
| RMBE745 | no desorption | | 240 | 5.50E-6 | 1060 | 4.70E-07 | 1.51 | 0.96 | 20 | 200 |
| RMBE744 | no desorption | | 240 | 5.50E-6 | 1060 | 4.70E-07 | 1.51 | 0.96 | 20 | 300 |
| RMBE897 | no desorption | | 275 | no info | 1040 | no info | 1.51 | 1 | 100 | 300 |
| RMBE898 | no desorption | | 300 | no info | 1050 | no info | 1.43 | 1.03 | 200 | 300 |
| RMBE915 | no desorption | | 300 | no info | 1050 | no info | 1.43 | 1.03 | 500 | 300 |
| RMBE954 | no desorption | | 300 | 5.40E-6 | 1032 | 5.10E-07 | 1.4 | 1.01 | 50 | 300 |

Table H.2 Samples of GaN QDs grown on c-plane GaN from Kyma Technologies

| RMBE# | substrate | size (cmXcm) | Quality | Ga droplet formation | Nitridation | | | |
|---|---|---|---|---|---|---|---|---|
| | | | | | Tnit ($^0$C) | N flow rate (sccm) | Power (W) | nit. time (min) |
| RMBE1197 | kyma AG854.7 | 0.5X1 | - | 5.5ML of Ga@185C | 185 | 1 | 350 | 30 |
| RMBE1256 | kyma AE902.5 | 1X1 | Bad | 5.5ML of Ga@185C | 185 | 0.35 | 350 | 30 |
| RMBE1257 | kyma AE1985.4 | 1X1 | Bad | 5.5ML of Ga@185C | 250 | 0.35 | 350 | 30 |
| RMBE1258 | kyma AE2158.3 | 1X1 | Bad | 5.5ML of Ga@185C | 550 | 0.35 | 350 | 30 |
| RMBE1263 | kyma AE2063.10 | 1X1 | Good | 5.5ML of Ga@185C | 185 | 1 | 350 | 30 |
| RMBE1264 | kyma AE2153.9 | 1X1 | Good | 5.5ML of Ga@185C | 185 | 0.35 | 350 | 30 |
| RMBE1265 | kyma AE1447.4 | 0.25X1 | Fine | 5.5ML of Ga@185C | 185 | 0.55 | 450 | 30 |
| RMBE1266 | kyma AE1447.4 | 0.75X1 | Fine | 5.5ML of Ga@185C | 250 | 0.35 | 350 | 30 |
| RMBE1267 | kyma AE2093.8 | 1X1 | Fine | 5.5ML of Ga@185C | 250 | 0.55 | 450 | 30 |

Table H. 3 Samples of GaN QDs grown on Si substrates

| RMBE# | substrate | cleaning | Oxide desorption | Ga droplet formation | Nitridation | | | |
|---|---|---|---|---|---|---|---|---|
| | | | | | Tnit ($^0$C) | N flow rate (sccm) | Power (W) | nit. time (min) |
| RMBE868 | Si(001) | HF cleaning | NA | 7.5ML of Ga@550C | 550 | 1 | 350 | 30 |
| RMBE866 | Si(001) | HF cleaning | NA | 7.5ML of Ga@550C | 650 | 1 | 350 | 30 |
| RMBE911 | Si(001) | HF cleaning | NA | 7.5ML of Ga@550C | 720 | 1 | 350 | 30 |
| RMBE969 | Si(001) | HF cleaning | thermal cleaning | 7.5ML of Ga@550C | 550 | 1 | 350 | 30 |
| RMBE1009 | Si(001) | HF cleaning | thermal cleaning | 7.5ML of Ga@550C | 650 | 1 | 350 | 30 |
| RMBE909 | Si(001) | HF cleaning | thermal cleaning | 7.5ML of Ga@550C | 720 | 1 | 350 | 30 |
| RMBE921 | Si(111) | HF cleaning | thermal cleaning | 7.5ML of Ga@550C | 550 | 1 | 350 | 30 |
| RMBE920 | Si(111) | HF cleaning | thermal cleaning | 7.5ML of Ga@550C | 650 | 1 | 350 | 30 |
| RMBE983 | Si(111) | HF cleaning | thermal cleaning | 7.5ML of Ga@550C | 720 | 1 | 350 | 30 |

Table H. 4 Samples of GaN films and NWs grown on Si substrates

| RMBE# | substrate | cleaning | Oxide desorption | Ga droplet formation | GaN growth | | | |
|---|---|---|---|---|---|---|---|---|
| | | | | | Tnit ($^0$C) | N flow rate (sccm) | Power (W) | nit. time (min) |
| RMBE1081 | Si(001) | HF cleaning | thermal cleaning | 1.5E-7 Torr of Ga BEP @800C | 800 | 1 | 400 | 180 |
| RMBE1091 | Si(001) | HF cleaning | thermal cleaning | 1.5E-7 Torr of Ga BEP @820C | 820 | 1 | 400 | 180 |
| RMBE1090 | Si(001) | HF cleaning | thermal cleaning | 1.5E-7 Torr of Ga BEP @840C | 840 | 1 | 400 | 180 |
| RMBE1095 | Si(001) | HF cleaning | thermal cleaning | 1.5E-7 Torr of Ga BEP @860C | 860 | 1 | 400 | 180 |
| RMBE1089 | Si(001) | HF cleaning | thermal cleaning | 9.8E-8 Torr of Ga BEP @800C | 800 | 1 | 400 | 180 |
| RMBE1082 | Si(001) | HF cleaning | thermal cleaning | 8E-8 Torr of Ga BEP @800C | 800 | 1 | 400 | 180 |
| RMBE1096 | Si(001) | HF cleaning | thermal cleaning | 3E-8 Torr of Ga BEP @800C | 800 | 1 | 400 | 180 |
| RMBE1100 | Si(001) | HF cleaning | thermal cleaning | 2E-8 Torr of Ga BEP @800C | 800 | 1 | 400 | 180 |
| RMBE1099 | Si(001) | HF cleaning | thermal cleaning | 3E-8 Torr of Ga BEP @780C | 780 | 1 | 400 | 180 |
| RMBE1101 | Si(001) | HF cleaning | thermal cleaning | 3E-8 Torr of Ga BEP @850C | 850 | 1 | 400 | 180 |
| RMBE1141 | Si(001) | HF cleaning | thermal cleaning | 1E-7 Torr of Ga BEP @800C | 800 | 1 | 400 | 180 |